Chemical Geology (2002), **191**, 165–181.

Experimental resetting of the U–Th–Pb systems in monazite

Anne-Magali Seydoux-Guillaume [a,*], Jean-Louis Paquette [b], Michael Wiedenbeck [a], Jean-Marc Montel [c], Wilhelm Heinrich [a]

[a] *GFZ-Potsdam, Division 4, Telegrafenberg, 14473, Potsdam, Germany*
[b] *Laboratoire de Géologie, UMR 6524 "Magmas et Volcans", Université B. Pascal, 5, Rue Kessler, 63038, Clermont-Ferrand Cedex, France*
[c] *LMTG-UMR 5563, Université Paul Sabatier, 39 Allées Jules Guesde, 31000, Toulouse, France*

Abstract

Abraded fragments (200–400 μm) of a large, chemically homogeneous, and non-metamict Brazilian monazite crystal, characterised by a concordant U–Pb ages of 474 ± 1 Ma ($^{208}Pb/^{206}Pb = 19.5$), were hydrothermally treated at varying temperatures with solutions of different compositions. Product monazites were analysed with Scanning Electron Microscope (SEM), Electron Microprobe (EMP), Secondary Ion Mass Spectrometer (SIMS) and Isotope Dilution–Thermal Ionisation Mass Spectrometer (ID-TIMS).

Experiments with pure water over a temperature range of 800–1200 °C, at 700 MPa and durations ranging from 5 to 60 days showed that even at 1200 °C any dissolution and recrystallization of new monazite is confined to the outermost surface of the grain. Neither Pb diffusion at the EMP scale, nor significant discordancy were observed.

We performed experiments at 800 and 1000 °C for different durations using different fluid compositions at quartz saturation: a 10 wt.% $CaCl_2$ fluid, a 10 wt.% $SrCl_2$ fluid, a 10 wt.% NaCl fluid and a fluid containing NBS 982 Pb standard ($^{208}Pb/^{206}Pb = 1$).

For all runs, EMP traverses revealed no Pb-diffusion profiles. Significant overgrowths of newly formed monazite are documented by SEM analyses. They occurred only in the 1000 °C experiments when either $CaCl_2$ or Pb-bearing fluids were present. In the $CaCl_2$ experiment, two zones could be distinguished within the crystal: a core possessing the initial monazite composition and a rim consisting of newly formed monazite produced by dissolution/precipitation, which was enriched in Ca and Pb-free. ID-TIMS dating of single grains treated with $SrCl_2$ and $CaCl_2$ solutions at 1000 °C are significantly discordant. Experiments employing the NBS Pb-standard produced sub-concordant monazite, for which the $^{207}Pb/^{206}Pb$ apparent age has become older than prior to the experiment (544 Ma at 800 °C and 495 Ma at 1000 °C). The newly grown monazite rim had obviously incorporated Pb from the fluid.

None of our reaction products contained a detectable diffusion profile. The only resetting mechanism we detected involved dissolution/precipitation. The extent of the dissolution/precipitation process depends on fluid composition and is a more efficient mechanism than diffusion for controlling the resetting of monazite in natural rocks.

Keywords: Monazite; U–Pb isotopes; Resetting; Fluid; Dissolution/precipitation; SIMS

ELSEVIER

Chemical Geology 191 (2002) 165–181

CHEMICAL GEOLOGY
INCLUDING
ISOTOPE GEOSCIENCE

www.elsevier.com/locate/chemgeo

Experimental resetting of the U–Th–Pb systems in monazite

Anne-Magali Seydoux-Guillaume [a,*], Jean-Louis Paquette [b], Michael Wiedenbeck [a], Jean-Marc Montel [c], Wilhelm Heinrich [a]

[a] *GFZ-Potsdam, Division 4, Telegrafenberg, 14473, Potsdam, Germany*
[b] *Laboratoire de Géologie, UMR 6524 "Magmas et Volcans", Université B. Pascal, 5, Rue Kessler, 63038, Clermont-Ferrand Cedex, France*
[c] *LMTG-UMR 5563, Université Paul Sabatier, 39 Allées Jules Guesde, 31000, Toulouse, France*

Abstract

Abraded fragments (200–400 μm) of a large, chemically homogeneous, and non-metamict Brazilian monazite crystal, characterised by a concordant U–Pb ages of 474 ± 1 Ma ($^{208}Pb/^{206}Pb = 19.5$), were hydrothermally treated at varying temperatures with solutions of different compositions. Product monazites were analysed with Scanning Electron Microscope (SEM), Electron Microprobe (EMP), Secondary Ion Mass Spectrometer (SIMS) and Isotope Dilution–Thermal Ionisation Mass Spectrometer (ID-TIMS).

Experiments with pure water over a temperature range of 800–1200 °C, at 700 MPa and durations ranging from 5 to 60 days showed that even at 1200 °C any dissolution and recrystallization of new monazite is confined to the outermost surface of the grain. Neither Pb diffusion at the EMP scale, nor significant discordancy were observed.

We performed experiments at 800 and 1000 °C for different durations using different fluid compositions at quartz saturation: a 10 wt.% $CaCl_2$ fluid, a 10 wt.% $SrCl_2$ fluid, a 10 wt.% NaCl fluid and a fluid containing NBS 982 Pb standard ($^{208}Pb/^{206}Pb = 1$).

For all runs, EMP traverses revealed no Pb-diffusion profiles. Significant overgrowths of newly formed monazite are documented by SEM analyses. They occurred only in the 1000 °C experiments when either $CaCl_2$ or Pb-bearing fluids were present. In the $CaCl_2$ experiment, two zones could be distinguished within the crystal: a core possessing the initial monazite composition and a rim consisting of newly formed monazite produced by dissolution/precipitation, which was enriched in Ca and Pb-free. ID-TIMS dating of single grains treated with $SrCl_2$ and $CaCl_2$ solutions at 1000 °C are significantly discordant. Experiments employing the NBS Pb-standard produced sub-concordant monazite, for which the $^{207}Pb/^{206}Pb$ apparent age has become older than prior to the experiment (544 Ma at 800 °C and 495 Ma at 1000 °C). The newly grown monazite rim had obviously incorporated Pb from the fluid.

None of our reaction products contained a detectable diffusion profile. The only resetting mechanism we detected involved dissolution/precipitation. The extent of the dissolution/precipitation process depends on fluid composition and is a more efficient mechanism than diffusion for controlling the resetting of monazite in natural rocks.

Keywords: Monazite; U–Pb isotopes; Resetting; Fluid; Dissolution/precipitation; SIMS

1. Introduction

The light rare-earth element (LREE)-phosphate monazite is widely used as a U–Th–Pb geochronom-

* Corresponding author. Present address: Institut für Planetologie, Wilhelm-Klemm-Str. 10, D-48149, Münster, Germany. Tel.: +49-251-83-33405.
E-mail address: seydoux@uni-muenster.de (A.-M. Seydoux-Guillaume).

0009-2541/02/$ - see front matter © 2002 Elsevier Science B.V. All rights reserved.
PII: S0009-2541(02)00155-9

eter to determine the timing of both magmatic and metamorphic events (Parrish, 1990). In most cases, $^{206}Pb/^{238}U$ and $^{207}Pb/^{235}U$ ages in monazites are concordant (e.g. Schärer et al., 1986; Corfu, 1988; Smith and Barreiro, 1990; Landzirotti and Hanson, 1995; Parrish, 1995; Simpson et al., 2000); nevertheless, discordant U–Pb ages have also been reported. Such discordant data may reflect mixing between different grain populations that crystallised at different times within a particular rock (Black et al., 1984; Bertrand et al., 1993; Childe et al., 1993); or a mixture of newly grown rims with inherited cores (Montel et al., 1996; Braun et al., 1998; Cocherie et al., 1998; Crowley and Ghent, 1999; Williams et al., 1999; Zhu and O'Nions, 1999; Poitrasson et al., 2000; Rubatto et al., 2001; Townsend et al., 2001), or else a diffusive Pb loss (Suzuki and Adachi, 1994; Suzuki et al., 1994). Clearly, the correct interpretation of measured isotope ratios requires a detailed understanding of the resetting process that affects the monazite isotope system.

Despite the fact that major analytical progress on the U–Th–Pb isotope system in natural monazite has recently been achieved by Secondary Ion Mass Spectrometry (SIMS) (Harrison et al., 1995; Grove and Harrison, 1999; Zhu et al., 1997; Rubatto et al., 2001), LA-ICP-MS (Poitrasson et al., 1996, 2000) and Electron Microprobe (EMP) methods (Montel et al., 1996; Cocherie et al., 1998; Crowley and Ghent, 1999), the controlling mechanisms that induce its partial or complete resetting during a geological event are only partially understood. There is an overall agreement that, in nature, the U–Th–Pb system in monazite may be reset by loss of Pb by interacting with coexisting fluids, implying a dissolution/precipitation process. The partitioning of elements between fluid and growing monazite would thus define the U–Th–Pb budget of any newly formed rims.

With respect to resetting by diffusive Pb loss, there have been several attempts to interpret discordant ages of natural monazite grains in terms of closure temperature of Dodson (1973). In Dodson's model, resetting results from the diffusion of the daughter isotopes out of the crystal; closure temperature depends on the size of the crystal, its shape, the cooling rate and the diffusion coefficient of the daughter elements. Experiments on Pb diffusion by Smith and Giletti (1997) and Cherniak et al. (2000) showed that such diffusion is very slow, even at high temperatures. A different approach is to determine empirically a "geological closure temperature" from natural occurrences. This approach yields temperatures as low as 530 ± 25 °C (Black et al., 1984) to 725 ± 25 °C (Copeland et al., 1988). However, it has been shown that monazite inclusions shielded by host minerals such as quartz or garnet are not always subject to resetting, despite the fact that they were exposed to granulite–facies temperatures above 800 °C over long time scales (De Wolf et al., 1993; Kalt et al., 2000; Montel et al., 2000). If the closure temperature calculated from the diffusion data and Dodson's model is similar to the geological closure temperature, then we can conclude that volume diffusion is the main resetting mechanism. If not, alternative mechanisms must be proposed, for example, dissolution/precipitation.

In dissolution/precipitation process, one would expect that fluid composition plays a key role. In an earlier study, Teufel and Heinrich (1997) demonstrated that the hydrothermal treatment of >40 μm natural monazite grains at 750 °C/0.3 GPa using pure water did not affect their U–Pb system. Significant dissolution and precipitation along with Pb loss into pure water was only observed when very fine powdered monazite (< 15 μm) was used as starting material. In those experiments, grains initially had an angular morphology, so they possessed high surface energies. Obviously, these experiments with crushed grains and pure water did not demonstrate definitively whether dissolution/precipitation is an important process for resetting large natural monazites.

The aim of the present experimental study was to investigate the effect of fluid composition on the resetting behaviour of monazite, in the case where the amount of dissolution/precipitation driven by surface energy is small. For this, all experiments were conducted with mechanically abraded grains. This is an extension of the study of Teufel and Heinrich, investigating higher $P–T$ conditions, more complex fluid compositions and analysing U–Pb isotopes of single grains. The effects of pure water at high temperature (>800 °C), NaCl, $CaCl_2$ and $SrCl_2$-bearing fluids on the dissolution/precipitation process and the concomitant redistributions of elements and isotopes are evaluated. NaCl was used as an analogue for "normal" crustal fluids. Sr- and Ca-bearing fluids were used to test for an exchange between Ca^{2+} (1.18 Å) or Sr^{2+} (1.31 Å) with Pb^{2+} (1.35 Å) (radii from Shannon,

1976) and because both of these elements are abundant in monazite-hosting minerals such as garnet and plagioclases. We also treated monazite with a NBS 982 Pb solution. This Pb standard is depleted in ^{208}Pb compared to monazite so any modification to the Pb system should be readily detected. Furthermore, because crustal fluids are generally SiO_2 saturated, with the exception of the pure water runs, we buffered all other experiments with SiO_2. Our data constrain which mechanisms dominate the resetting of the U–Th–Pb isotope system in monazite and what influence the composition of the fluid phase and temperature have on this process.

2. Sample description and experimental approach

A monazite single crystal, 3×2 cm in size, from the Itambe pegmatite district (Brazil, Cruz et al., 1996) was used for this study. The yellow-orange crystal was nearly free of fluid and solid inclusions, and is homogeneous at the micrometer scale, as demonstrated by multiple EMP analysis and profiles (Seydoux et al., 1999). The composition is typical for natural monazites (Table 1) containing 6.92 wt.% ThO_2, 0.13 wt.% UO_2 and 0.16 wt.% PbO. In terms of end-members, the $LREE_{La-Gd}PO_4$ component makes up 89.8 mol% and the $Y+HREE_{Tb-Lu}PO_4$ component, 1.7 mol%. Th is incorporated through nearly equal amounts of brabantite $CaTh(PO_4)_2$ ($\sim$ 3.8 mol%) and huttonite $ThSiO_4$ ($\sim$ 4.3 mol%) components. Detailed study using TEM, XRD, and Raman spectroscopy methods showed that this monazite is non-metamict and contains only nanometer-scale domains, where the lattice is weakly distorted (Seydoux-Guillaume et al., 2002). Multiple Isotope Dilution–Thermal Ionisation Mass Spectrometer (ID-TIMS) analyses yielded concordant U–Pb ages of 474 ± 1 Ma and document the isotopic homogeneity of the monazite (Table 2).

A fragment of the crystal was broken and sieved into different grain size fractions. For our experiments, the 200–400-μm fraction was used. The angular grains obtained after crushing were mechanically air-abraded (Krogh, 1982) in order to obtain a rounded morphology (Fig. 1a). This was done to avoid the preferential dissolution of the angular edges during hydrothermal experiments (Teufel and Heinrich, 1997). Abraded fragments were washed in 0.1N HNO_3. Only well-rounded grains devoid of micro-inclusions were selected for experiments.

A long duration experiment using pure water was performed at 800 °C/0.2 GPa for 60 days. Shorter duration runs were performed at 1000, 1100 and 1200 °C/0.7 GPa for 7, 12 and 5 days, respectively (Table 3). At such high $P-T$ conditions, no longer runs were possible with internally heated vessel for safety reasons. For each run, about 10 abraded fragments were placed into a platinum capsule (0.2 mm wall thickness) filled with $\sim$ 20 mg of distilled H_2O. The capsules, 15 mm in length and 3 mm in diameter, were welded and checked for leaks by heating at 110 °C for 24 h. A standard cold seal pressure vessel was used for the 800 °C/0.2 GPa experiment. For experiments at higher temperatures, an internally heated pressure vessel (IHPV), using Ar as the pressure medium, was employed. Temperature error is within ± 2 °C for the 800 °C, and ± 25 °C for the 1200 °C. Details about the apparatus and calibration procedure can be found in Vielzeuf and Montel (1994). At the end of the runs, vessels were quenched to room temperature within a few minutes. After quenching, each capsule was checked for leakage by weighing.

One experiment was performed at 1100 °C/0.2 GPa in silica saturated water; about 30 monazite grains plus 1 mg SiO_2 powder were placed into a Pt capsule along with 10 μl distilled H_2O. This experiment was also run in an IHPV.

In another series of experiments, monazites were treated with fluids of different compositions: H_2O–NaCl, $H_2O-CaCl_2$ or $H_2O-SrCl_2$. Salt concentrations were 10 wt.% in all runs. Additionally, a HNO_3-bearing solution containing 950 μg/g NBS 982 Pb standard ($^{208}Pb/^{206}Pb = 1.000$, $^{207}Pb/^{206}Pb = 0.467$ and $^{206}Pb/^{204}Pb = 36.739$) was used in two runs. At 800 °C/0.2 GPa, experiments were again performed in standard cold seal hydrothermal pressure vessels, and at 1000 °C/1 GPa in a piston-cylinder apparatus with a 22-mm-diameter pressure chamber and CaF_2 as pressure medium. In the latter, Pt–PtRh thermocouples were used for temperature control. The temperature difference along the 13-mm-long capsules was ± 13 °C at 1000 °C, and the variation of temperature during the run was ± 2 °C. Piston cylinder experiments were quenched in a few seconds. Experimental conditions of all runs are summarised in Table 3.

Table 1
EMP analyses for the untreated monazite (Untreated) and some representative analyses for a monazite grain from the VRM0-1 experiment (1000 °C, 1 GPa, 21 days) at different distances from the crystal rim (see Fig. 3)

	Untreated	Distance along E–F (μm) in VRM0-1 (1000 °C, $CaCl_2$-bearing fluid)					
		24	80	100	102	104	110
Wt.%							
P_2O_5	27.81	27.46	28.07	27.14	27.03	27.33	27.51
SiO_2	1.42	1.77	1.42	1.51	1.83	1.66	1.43
ThO_2	6.92	7.27	6.92	7.55	9.37	8.64	7.24
UO_2	0.13	0.21	0.08	0.05	0.06	0.15	0.12
Y_2O_3	0.71	0.70	0.63	0.41	0.27	0.63	0.69
La_2O_3	14.51	13.83	14.17	14.05	13.90	13.43	13.93
Ce_2O_3	30.59	29.99	29.92	29.87	29.23	29.56	30.05
Pr_2O_3	3.14	3.22	3.13	2.96	3.10	3.17	3.02
Nd_2O_3	10.20	10.53	10.03	10.47	10.86	10.34	10.28
Sm_2O_3	2.05	2.22	2.13	2.19	2.03	2.13	2.04
Gd_2O_3	0.94	1.06	0.92	1.00	0.88	0.97	0.92
Tb_2O_3	–	0.12	0.07	0.11	0.14	0.02	0.07
Dy_2O_3	0.11	0.15	0.16	0.07	0.01	0.09	0.12
Ho_2O_3	–	0.00	0.04	0.00	0.00	0.00	0.00
Er_2O_3	0.05	0.08	0.11	0.00	0.10	0.01	0.02
Yb_2O_3	–	0.02	0.03	0.01	0.00	0.00	0.06
Lu_2O_3	–	0.04	0.00	0.00	0.00	0.00	0.00
PbO	0.16	0.00	0.00	0.00	0.00	0.13	0.18
CaO	0.44	0.53	0.61	0.57	0.56	0.45	0.39
Σ	99.18	99.19	98.43	97.94	99.35	98.71	98.06
Cations (pfu) on the basis of 16 oxygens							
P	3.782	3.734	3.812	3.750	3.704	3.747	3.784
Si	0.229	0.284	0.228	0.247	0.296	0.269	0.232
Th	0.253	0.266	0.253	0.280	0.345	0.318	0.268
U	0.005	0.007	0.003	0.002	0.002	0.005	0.004
Y	0.061	0.060	0.054	0.035	0.023	0.054	0.060
La	0.860	0.819	0.838	0.846	0.830	0.802	0.835
Ce	1.799	1.764	1.757	1.785	1.732	1.753	1.788
Pr	0.184	0.188	0.183	0.176	0.183	0.187	0.179
Nd	0.585	0.604	0.575	0.610	0.628	0.598	0.596
Sm	0.114	0.123	0.118	0.123	0.113	0.119	0.114
Gd	0.050	0.056	0.049	0.054	0.047	0.052	0.049
Tb	–	0.006	0.004	0.006	0.007	0.001	0.004
Dy	0.006	0.008	0.008	0.003	0.000	0.005	0.006
Ho	–	0.000	0.002	0.000	0.000	0.000	0.000
Er	0.002	0.004	0.005	0.000	0.005	0.001	0.001
Yb	–	0.001	0.001	0.000	0.000	0.000	0.003
Lu	–	0.002	0.000	0.000	0.000	0.000	0.000
Pb	0.007	0.000	0.000	0.000	0.000	0.006	0.008
Ca	0.076	0.092	0.105	0.100	0.097	0.078	0.067
Σ	8.013	8.018	7.995	8.017	8.012	7.995	7.998
End-members							
$LREEPO_4$	0.898	0.889	0.880	0.899	0.883	0.878	0.890
$YHREEPO_4$	0.017	0.020	0.019	0.011	0.009	0.015	0.019
$CaThU(PO_4)_2$	0.038	0.025	0.053	0.028	0.034	0.039	0.034
$PbThU(PO_4)_2$	0.004	0.000	0.000	0.000	0.000	0.003	0.004
$ThSiO_4$	0.043	0.054	0.037	0.056	0.069	0.059	0.049
$USiO_4$	0.001	0.001	0.000	0.000	0.000	0.001	0.001
Σ	1.001	0.989	0.989	0.994	0.996	0.995	0.996

Table 2
U–Pb isotope data for monazite reactants and products (single grain analysis)

Analysed sample	Weight (μg)	U (ppm)	Pb rad (ppm)	$^{206}Pb/^{204}Pb$	$^{208}Pb/^{206}Pb$	$^{206}Pb/^{238}U$	$^{207}Pb/^{235}U$	$^{207}Pb/^{206}Pb$	$^{206}Pb/^{238}U$	$^{207}Pb/^{235}U$	$^{207}Pb/^{206}Pb$	Discordancy (%)
		Concentrations		Atomic ratios					Apparent ages (Ma)			
Untreated monazite 1	40	1216	1670	3692	19.5718	0.07631 ± 5	0.5950 ± 5	0.05655 ± 2	474	474	474	0
Untreated monazite 2	58	1310	1788	4651	19.4575	0.07629 ± 5	0.5951 ± 4	0.05657 ± 2	474	474	475	0
Untreated monazite 3	41	868	1189	3773	19.459	0.07650 ± 27	0.5973 ± 22	0.05662 ± 6	475	476	477	0
Untreated monazite 4	38	1286	1758	3693	19.4553	0.07634 ± 36	0.5956 ± 29	0.05659 ± 4	474	474	475	0
Untreated monazite 5	37	1005	1399	1350	19.6078	0.07646 ± 64	0.5965 ± 52	0.05658 ± 15	475	475	475	0
VRM97-10 (1000 °C, H_2O)	87	1248	1650	2290	19.2005	0.07457 ± 37	0.5814 ± 40	0.05657 ± 26	464	465	474	3.2
VRM97-8 (1100 °C, H_2O)	123	1087	1471	1757	19.387	0.07554 ± 53	0.5892 ± 60	0.05657 ± 40	469	470	475	1.3
VRM97-8 (2) (1100 °C, H_2O)	116	1051	1412	1758	19.2604	0.07542 ± 115	0.5878 ± 99	0.05652 ± 41	469	469	473	1.2
VRM97-6 (1200 °C, H_2O)	107	1224	1623	2141	18.9959	0.07555 ± 33	0.5887 ± 42	0.05652 ± 30	470	470	473	0
VRM99-2 (1100 °C, H_2O-SiO_2)	26	1076	1484	416	19.0767	0.07579 ± 216	0.5915 ± 299	0.05660 ± 226	471	472	476	1.2
VRM0-7 (800 °C, Pb-standard)	116	852	1254	253	16.9981	0.08699 ± 44	0.7000 ± 37	0.05836 ± 87	538	539	543	–
VRM0-18 (1000 °C, Pb-standard)	78	1024	1392	530	18.1686	0.07851 ± 70	0.6181 ± 57	0.05710 ± 12	487	489	495	–
VRM0-4 (800 °C, $CaCl_2$)	102	576	780	706	18.8929	0.07640 ± 147	0.5959 ± 178	0.05657 ± 124	475	475	475	0
VRM0-1 (1000 °C, $CaCl_2$)	204	507	226	3253	19.7006	0.02464 ± 43	0.1921 ± 35	0.05655 ± 23	157	178	474	67.8
VRM0-3 (800 °C, $SrCl_2$)	90	645	878	3630	19.3986	0.07626 ± 75	0.5945 ± 60	0.05654 ± 14	474	474	476	0
VRM0-2 (1000 °C, $SrCl_2$)	126	669	767	4555	19.4326	0.06416 ± 105	0.5001 ± 82	0.05653 ± 9	401	412	473	16
VRM0-17 (800 °C, NaCl)	83	677	918	2838	19.5046	0.07546 ± 36	0.5873 ± 35	0.05645 ± 20	469	469	470	0

For untreated monazites, a 4-pg blank correction was applied corresponding to a corrected $^{206}Pb/^{204}Pb$ ratio of around 6500. For the treated monazites, it was necessary to add an experimental blank in the calculations. Nevertheless, it is not possible to precisely define an experimental blank. Consequently, an individual experimental blank was determined for each experiment in order to obtain a corrected $^{206}Pb/^{204}Pb$ ratio of 6500.

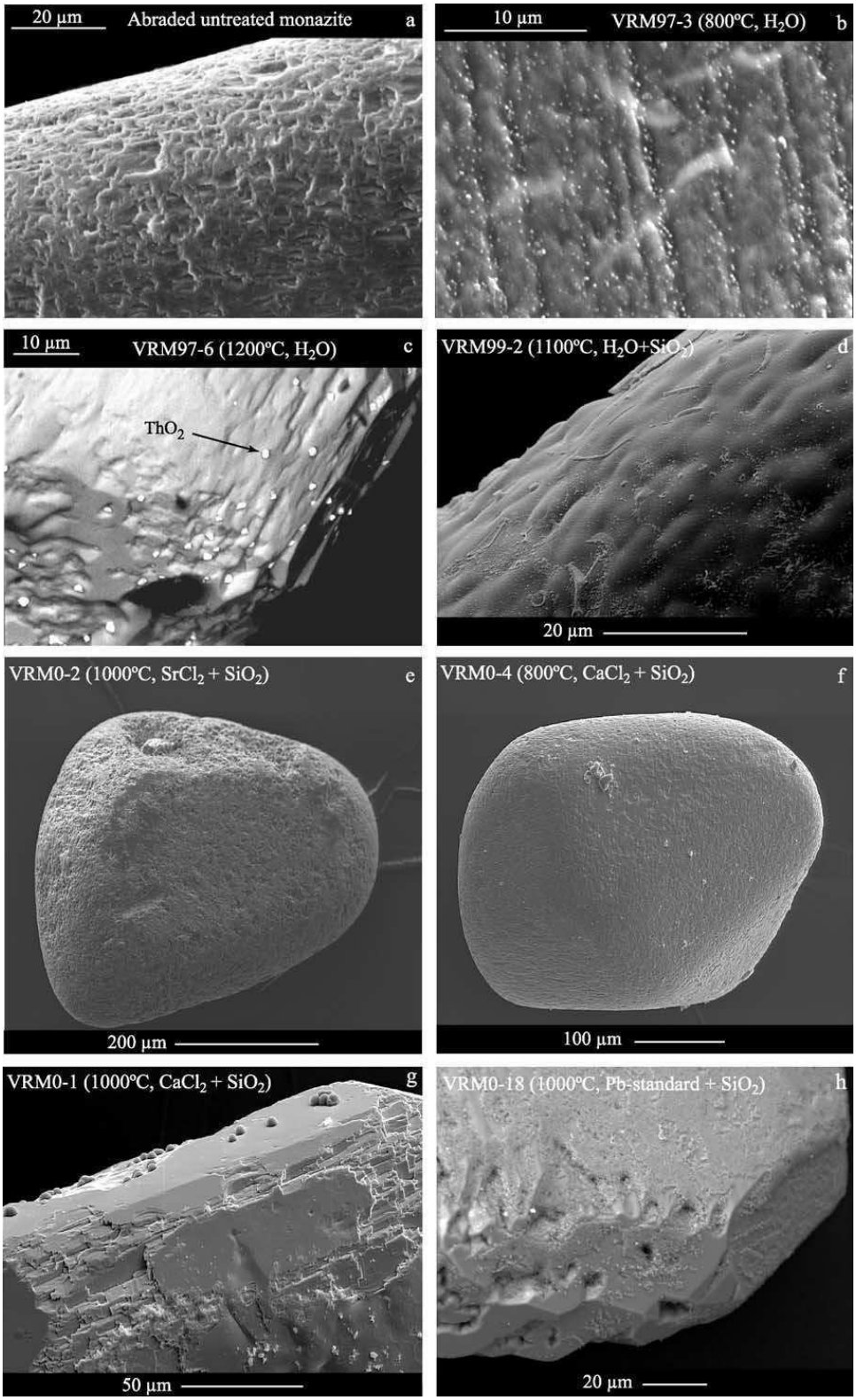
20 µm
Abraded untreated monazite
a
10 µm
VRM97-3 (800°C, H2O)
b
10 µm
VRM97-6 (1200°C, H2O)
c
ThO2
VRM99-2 (1100°C, H2O+SiO2)
d
20 µm
VRM0-2 (1000°C, SrCl2 + SiO2)
e
200 µm
VRM0-4 (800°C, CaCl2 + SiO2)
f
100 µm
VRM0-1 (1000°C, CaCl2 + SiO2)
g
50 µm
VRM0-18 (1000°C, Pb-standard + SiO2)
h
20 µm

Table 3
Experimental conditions of all runs and results of each run concerning the changes of surface morphology, the precipitation of new phases, the chemical changes near the surface and an estimation from the percentage of monazite dissolution during the run

Run number	Weight of monazite (mg)	Weight of fluid (mg)	Fluid composition	T (°C)	P (GPa)	Duration (days)	Textural changes (SEM)	New phases (SEM)	Chemical changes (EMP)	Estimate[a] of monazite dissolution (%)
VRM97-3	0.97	20	H_2O	800	0.2	60	none	ThO_2	none	0.82
VRM97-10	0.62	20	H_2O	1000	0.7	7	new faces (~ 5 μm) on the surface	ThO_2	none	3.87
VRM97-8	1.14	20	H_2O	1100	0.7	12	new faces (~ 12 μm) on the surface	ThO_2	none	3.33
VRM97-6	0.72	20	H_2O	1200	0.7	5	new faces (>40 μm) on the surface	ThO_2	none	7.78
VRM99-2	0.55	10	$H_2O + SiO_2$	1100	0.2	27	none	Quartz	none	3.45
VRM0-7	2.33	11.44	NBS 982 Pb + SiO_2	800	0.2	26	none	Quartz	none	0.20
VRM0-18	1.03	11.52	NBS 982 Pb + SiO_2	1000	1	14	significant overgrowths	Quartz	none	2.13
VRM0-4	1.96	11.71	10 wt.% $CaCl_2 + SiO_2$	800	0.2	39	none	Quartz + brabantite	none	0.24
VRM0-1	2.27	11.84	10 wt.% $CaCl_2 + SiO_2$	1000	1	21	significant overgrowths	Quartz	significant variations	0.99
VRM0-3	1.92	12.05	10 wt.% $SrCl_2 + SiO_2$	800	0.2	39	none	Quartz + $SrCl_2$	none	0.25
VRM0-2	2.05	11.42	10 wt.% $SrCl_2 + SiO_2$	1000	1	21	none	Quartz	none	1.06
VRM0-17	0.97	11.85	10 wt.% $NaCl + SiO_2$	800	0.2	18	none	Quartz	none	0.49

[a] Estimate using the data from Devidal et al. (1998) (see Discussion for details).

Subsequent to each run, the samples were hand-picked and split for optical microscopy, scanning electron microscope (SEM), EMP and SIMS analyses. A single grain from each run was selected for ID-TIMS analysis.

3. Analytical methods

Grain surface morphology was investigated using an SEM. BSE and SE images were made on grains for each using a Zeiss DSM962 scanning electron microscope. Acceleration voltage was typically 15 kV.

Additionally, EMP analyses of polished single monazite grains mounted in epoxy resin were obtained using a Cameca SX-50 electron microprobe equipped with a wavelength dispersive system. The operating conditions are given in Förster (1998a). Core–rim relationships of at least one monazite grain from each run were evaluated by measuring compositional profiles in 2-μm steps

Fig. 1. BSE–SEM micrographs illustrating textural characteristics observed in both untreated and treated monazite. (a) Surface details of an abraded but otherwise untreated monazite fragment. (b) Surface details of a monazite grain from the experiment VRM97-3 (H_2O, 800 °C). Many small (200 nm) "bright" crystals of thorianite (ThO_2) were observed on the surface of the grain. (c) Surface details of a monazite grain from the experiment VRM97-6 (H_2O, 1200 °C). The grain appears totally recrystallised with very large, newly formed faces and ThO_2 crystals were observed. (d) Experiment VRM99-2 ($H_2O + SiO_2$, 1100 °C). Presence of Si in the system seems to avoid formation of ThO_2 crystals. (e) Experiment VRM0-2 ($SrCl_2$, 1000 °C). No overgrowth was observed. (f) Experiment VRM0-4 ($CaCl_2$, 800 °C). No overgrowth was observed. (g) Experiment VRM0-1 ($CaCl_2$, 1000 °C). Significant overgrowths were observed. Monazite shows new-formed faces. (h) Experiment VRM0-18 (Pb standard, 1000 °C). Significant overgrowths were observed. Monazite shows new-formed faces.

across the grain. Furthermore, X-ray imaging was conducted on a monazite grain from run VRM0-1 (1000 °C, 1 GPa, $CaCl_2$-bearing solution) using a Cameca SX 100 microprobe. Element mapping for Th–M_α, Pb–M_β and U–M_β was made in wavelength-dispersive mode, and for Ca–K_α, Ce–L_α and P–K_α in energy dispersive mode with the following conditions: accelerating potential 20 kV, beam current 30 nA and scan of 256×256 pixels with 600 ms/pixel.

The Cameca ims 6f ion probe in GFZ-Potsdam was used to acquire digital images of the relative concentration distributions of selected elements (see Appendix A) within our monazite sample VRM0-1 (1000 °C, $CaCl_2$ fluid).

Individual thermal ionisation U–Pb isotope analyses were performed in Clermont–Ferrand (UMR 6524) on five abraded monazite fragments from our starting material plus on one product grain from each experiment. The selected grain was washed in a 0.1N HNO_3 heated solution in order to clean grains from experiment derived in common Pb contamination. The selected grain was dissolved using 8N HCl in a PFA Teflon modified version of Parrish-type microcapsules (Parrish, 1987) at 210 °C, during 16–20 h. Chemical separation and mass spectrometry were performed according to Pin and Paquette (1997).

4. Results

Optical microscopy revealed a complete discolorization of the monazite grains after all runs, from yellowish orange to whitish grey (see Observational basis). Teufel and Heinrich (1997) already reported this effect. All the results in textural changes, chemical changes and appearance of new phases are summarised in Table 3. Isotopic changes are reported in Table 2.

4.1. Grain surface morphology

4.1.1. No visible modification on the grain surface

SEM images for experiments with $H_2O + SiO_2$, NaCl, $SrCl_2$, $CaCl_2$ at 800 °C and Pb standard at 800 °C showed no textural modifications of the monazite grains (Fig. 1d,e and f). Quartz crystals related to the SiO_2 in excess in the capsule were present in all runs. For the experiment with $SrCl_2$ fluid at 800 °C, few small $SrCl_2$ crystals were found in the run products. For the experiment with $CaCl_2$ fluid at 800 °C, precipitation of some brabantite crystals $(Ca,Th)(PO_4)_2$ occurred.

4.1.2. Moderate modifications

For experiments with pure H_2O, SEM imaging showed little modifications of the surface of the grains. At 800 °C, there is no apparent modification of monazite grains except the precipitation of numerous 200-nm crystals appearing bright in BSE images on the grain surfaces (Fig. 1b). However, at temperatures higher than 1000 °C, the development of new, ~ 5-μm-long crystal faces on the grain surface as well as "bright" crystals, 1–2 μm large, were observed. At 1100 °C, these faces are longer, reaching 12 μm in length. Finally, by 1200 °C, large newly formed faces (>40 μm) and larger "bright" crystals with cubic morphology are visible (Fig. 1c). EDS analysis demonstrated that the faces are Th-depleted monazite and that the "bright" crystals are ThO_2 (thorianite), which is consistent with their cubic morphology.

Because Th can be incorporated in monazite via the $[P_{-1}REE_{-1}Si_1Th_1]$ thorium–silicate component, the presence of silica might affect the monazite solution interactions. In contrast to the SiO_2-free experiment VRM97-8, SEM images of monazite from experiment VRM99-2 (water + SiO_2) (Fig. 1d) show no growth of newly formed monazite and no ThO_2 on the surface. An excess of SiO_2 in the system prevented the formation of new ThO_2 crystals. This is the first indication of the role of fluid composition on monazite behaviour in fluids.

4.1.3. Significant modifications

Finally, two experiments showed significant overgrowths: first with $CaCl_2$ fluid at 1000 °C (Fig. 1g) and the second with Pb fluid at 1000 °C (Fig. 1h). In both experiments, the monazite grains seem to have significantly recrystallized.

4.2. Modifications of chemical compositions

4.2.1. No EMP-measurable variations

EMP imaging (BSE and X-ray) and concentration profiles from the rims to the centres of monazite

grains showed no variation of the chemical composition; of particular importance is that no Pb-diffusion profiles were detected for experiments with H_2O, $H_2O + SiO_2$, NaCl, $SrCl_2$, $CaCl_2$ at 800 °C and Pb fluids.

4.2.2. Significant variations

Only the experiment with $CaCl_2$ at 1000 °C showed significant variations in monazite chemical composition. In order to confirm this result, a second grain was analysed. BSE imaging and EMP traverses of these two monazite fragments both document significant zonation. Fig. 2 shows a BSE image for one grain prepared for EMP. Two domains are clearly visible, demarked by a "bright" discontinuity (1). The external domain (rim) shows sharper faces as compared to the internal domain (core). On this grain, EMP profile E–F from the rim to the core of the grain (Fig. 3), X-ray imaging (Fig. 4) and SIMS imaging (Fig. 5) were performed. The EMP and SIMS maps show that the results obtained on the profile can be generalised to the whole grain. Two zones with different chemical compositions, separated by a sharp boundary (1) (Fig. 2), could be readily distinguished in all data sets. At (1), a significant enrichment in Th and Si is observed over a 2–4-μm distance, correlated

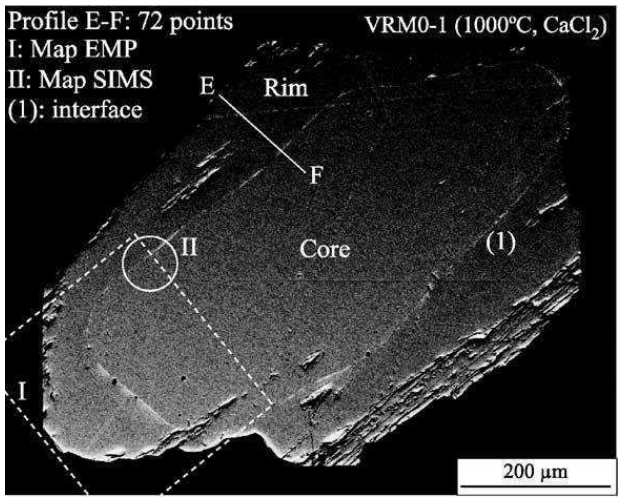

Fig. 2. BSE image of a polished monazite grain from VRM0-1 (1000 °C, $CaCl_2$) in epoxy showing the location of EMP profile (E–F) from Fig. 3, EMP–X-ray imaging (map I) from Fig. 4 and SIMS-imaging (map II) from Fig. 5. The interface (1) between the rim and the core of this grain is clearly visible.

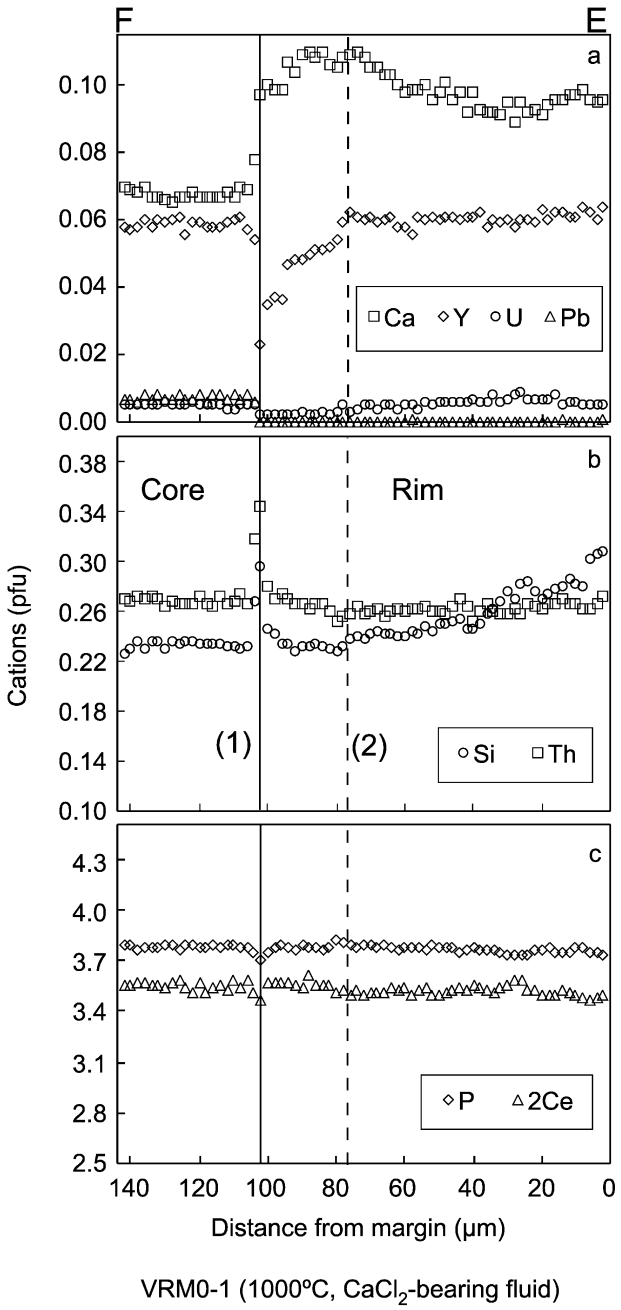

Fig. 3. EMP-traverse E–F across rim–core interface (Fig. 2). Ca, Y, U, Pb, Th, Si, P and Ce content in cations are reported and some analyses are in Table 2. The line at 102 μm corresponds to the "bright" interface (1) observed in Fig. 2.

with a P and Ce depletion (Figs. 3 and 4). The rim is free of Pb but enriched in Ca relative to the initial monazite (Figs. 3–5). Furthermore, in contrast to the

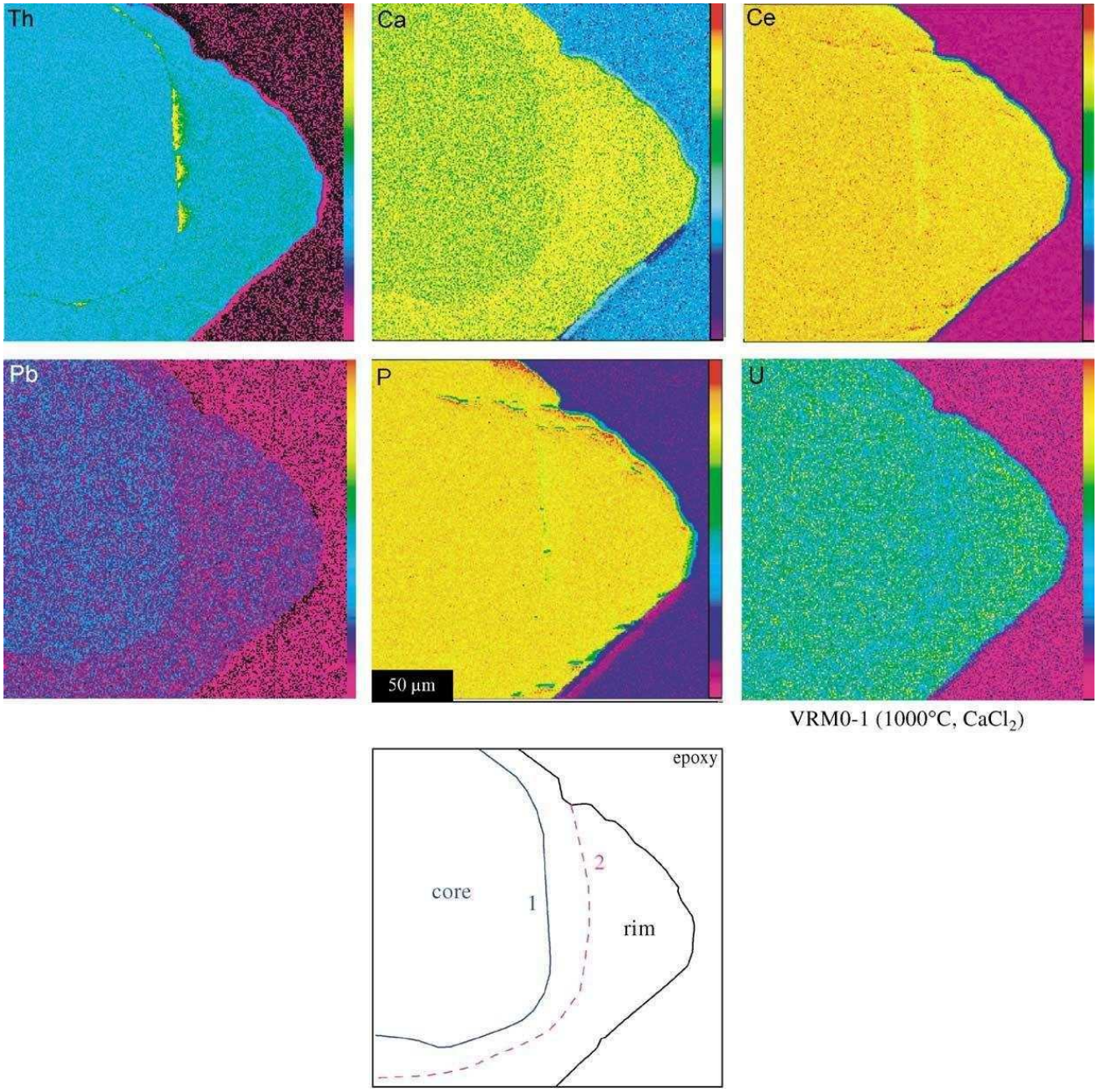

Fig. 4. X-ray imaging (map I) from the grain shown in Fig. 2 (experiment VRM0-1 with $CaCl_2$ at 1000 °C). Th, Pb and U were analysed with WDS and Ca, Ce and P with EDS using a Cameca SX-100 EMP. Analytical conditions: 30 nA, 20 kV, 256 × 256 µm, 600 ms/µm. The drawing under the images shows the distinguished zones: the sharp interface (1) between the rim and the core and a diffuse interface (2). Between (1) and (2), U is depleted and Ca enriched.

core, the $ThSiO_4$ end-member newly formed in the rim is greater than the $REEPO_4$ component (Table 1). A more gradual decrease in both U and Y concentrations at the discontinuity (2) is also observed (Figs. 3–5). The $(Y+HREE)PO_4$ xenotime and $USiO_4$ coffinite components decrease (Table 1), whereas Ca increases. U and Y are depleted between locations (1) and (2) over a distance of ~ 30 µm (Figs. 3–5),

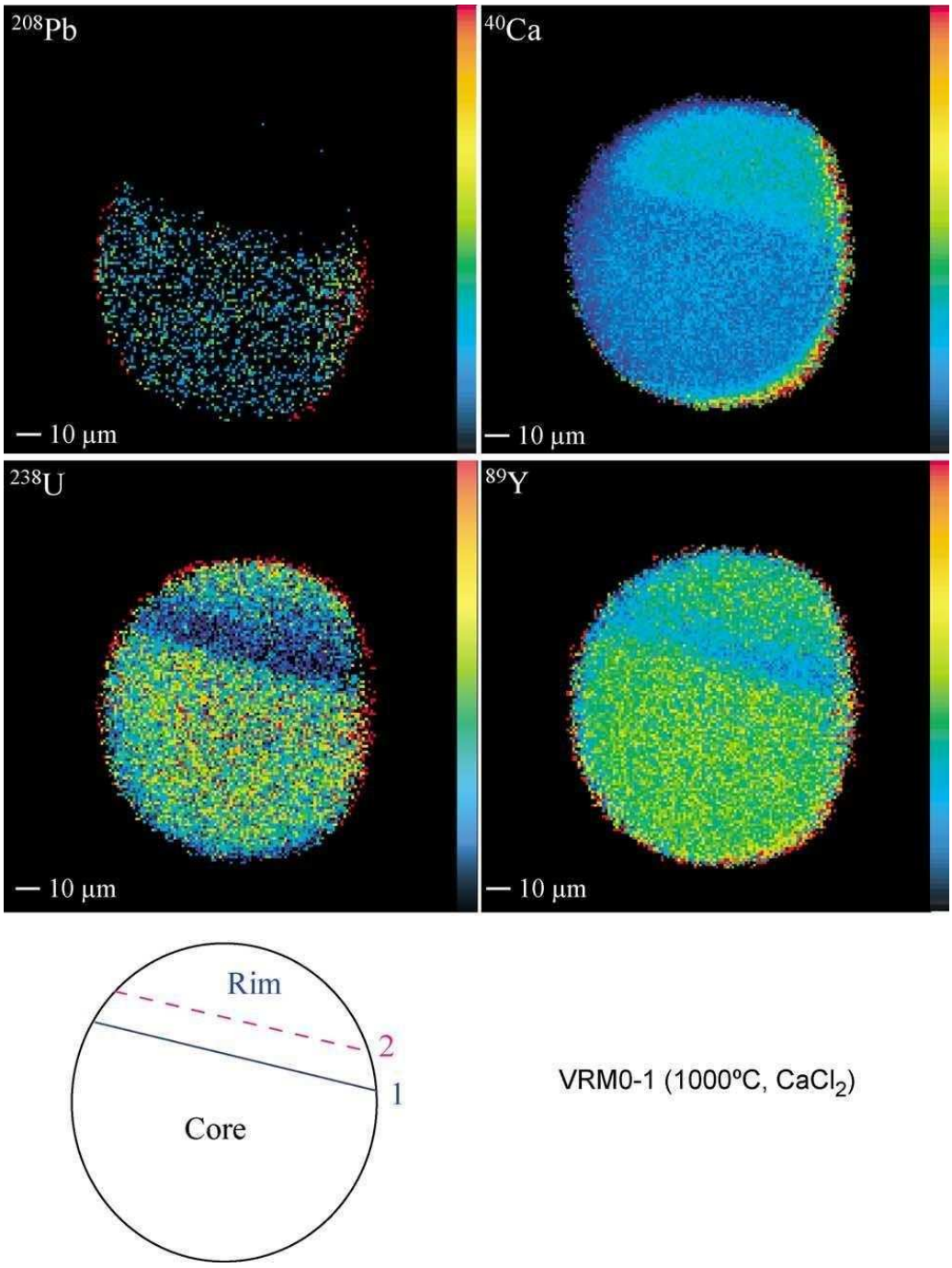

Fig. 5. SIMS digital ion image (map II) from the grain shown in Fig. 2 (experiment VRM0-1 with $CaCl_2$ at 1000 °C). Images were corrected with ^{140}Ce in order to suppress artefacts caused by sample charging ($^{40}Ca \times 100/^{140}Ce$; $^{208}Pb \times 100/^{140}Ce$; $^{89}Y \times 100/^{140}Ce$ and $^{238}U \times 1000/^{140}Ce$). Field of view is ~ 75 µm in diameter.

whereas Ca is enriched. The discontinuity (2) (more visible in Figs. 3 and 5) is more diffuse. Furthermore, the Si content increases gradually starting 60 µm away from E (Fig. 3). The core showed the same composition as the initial monazite (Table 1) and no other significant variations were observed.

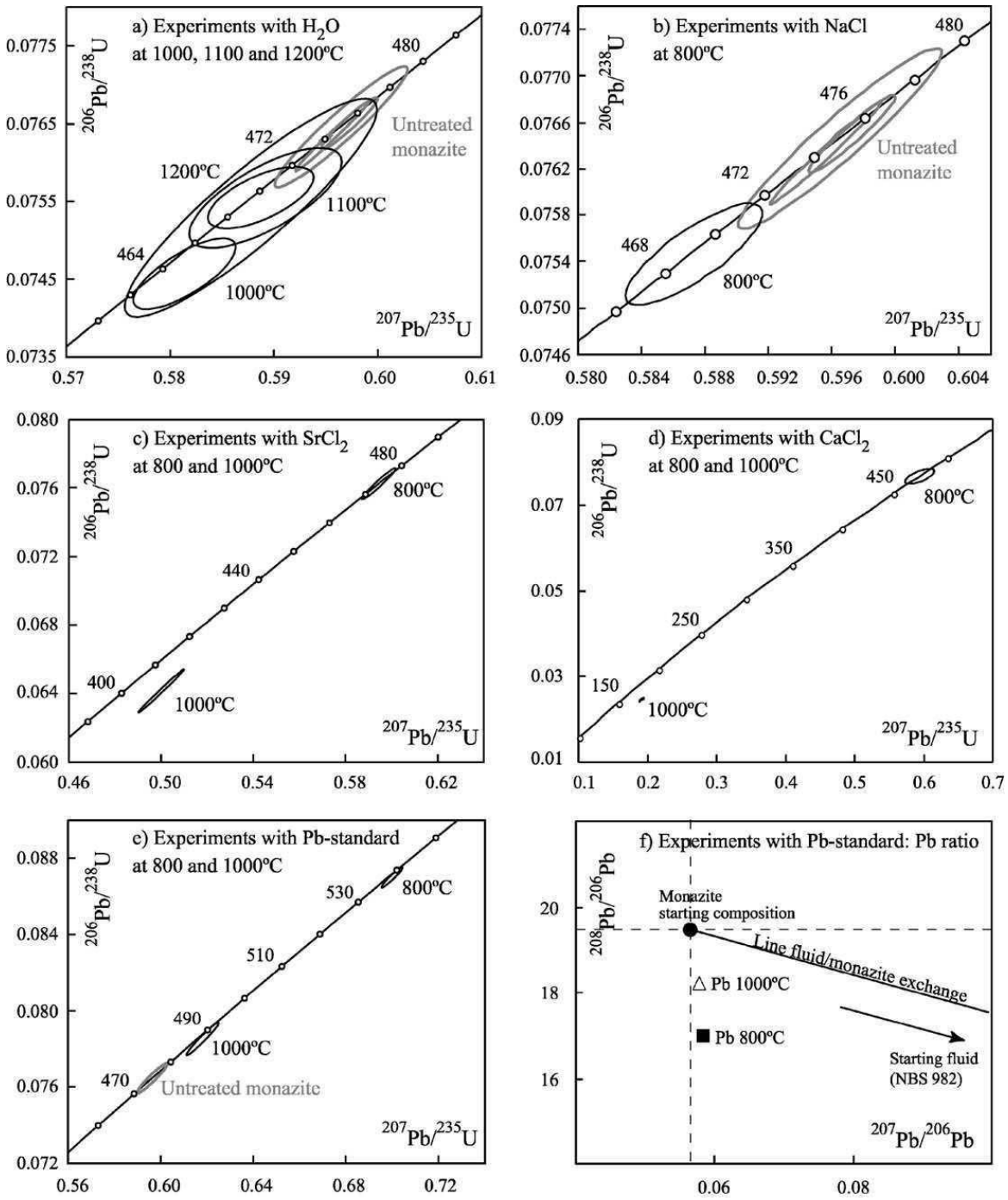

Fig. 6. U–Pb concordia diagrams for monazites experimentally treated by several fluids. (a) Untreated monazite and experiments with H_2O; (b) experiments with NaCl; (c) experiments with $SrCl_2$; (d) experiments with $CaCl_2$; (e) experiments with Pb standard. (f) $^{208}Pb/^{206}Pb$ vs. $^{207}Pb/^{206}Pb$ diagram. Pb 800 °C and Pb 1000 °C correspond to the experimental values measured with ID-TIMS (see Table 2). Individual error ellipses are quoted at the 2σ level. The analytical point for $H_2O + SiO_2$ is not plotted in the diagram owing to the very large error ellipse. Nevertheless, the point is centred on the untreated monazite and consequently can be considered as concordant.

4.3. Isotopic modifications

4.3.1. No significant discordancy

For the experiments employing H_2O, $H_2O + SiO_2$, NaCl, $SrCl_2$ and $CaCl_2$ at 800 °C, single grain analyses yielded sub-concordant to concordant U–Pb ages in the range of 458–475 Ma (Table 2 and Fig. 6a–d). U and Pb concentrations coincide within error limits to the starting material (Table 2). A duplicate of the experiment at 1100 °C with H_2O demonstrates the reproducibility of the U–Pb isotope analyses and the homogeneity of run products.

4.3.2. Significant modifications

Significant discordancy was only observed at 1000 °C when $CaCl_2$ or $SrCl_2$ was present in the fluid. In the $SrCl_2$-enriched fluid, the discordancy was about 16% (Table 2 and Fig. 6c), whereas in the case of $CaCl_2$ enriched fluid, the discordancy was 68% (Fig. 6d). This Pb loss is in agreement with the EMP results, which show a volume of about 70% from the newly grown, Pb-free monazite.

U–Pb analyses of monazite that reacted with NBS 982 show major change in Pb isotopic composition, an effect most pronounced in the 800 °C run. The $^{208}Pb/^{206}Pb$ ratio decreases from ~19.5 to 17.0 at 800 °C and 18.2 at 1000 °C and the $^{207}Pb/^{206}Pb$ increase from ~0.0566 to 0.0584 at 800 °C and 0.0571 at 1000 °C, reflecting an enrichment of both ^{207}Pb and ^{206}Pb relative to ^{208}Pb (Table 2). This results in sub-concordant analytical data points where the apparent $^{207}Pb/^{206}Pb$ and Pb/U ages are older than that of the initial monazite (Fig. 6e). Interestingly, the $^{207}Pb/^{206}Pb$ age obtained from the experiment at 800 °C (543 Ma) is older than that for the experiment at 1000 °C (495 Ma).

5. Discussion

5.1. Theoretical basis

Our experiments are based fundamentally on interactions between a solid phase and a fluid phase. We can anticipate that several processes will occur during a run.

The first process is the dissolution of the grains, in order to reach a chemical equilibrium. Devidal et al. (1998) determined the solubility of $NdPO_4$ in pure water from 450 to 800 °C at 200 MPa. They also demonstrated that the solubility of $NdPO_4$ is similar in pure water and in diluted NaCl–HCl–H_2O, and is independent of pH. The experimental conditions in this study were different from ours, but we can, nonetheless, use data of Devidal et al. (1998) to estimate the magnitude of the dissolution process. The saturation should represent 4 μg of monazite/10 mg of fluid at 800 °C, 12 μg/10 mg at 1000 °C, 19 μg/10 mg at 1100 °C, and 28 μg/10 mg at 1200 °C. Then, we can calculate from crystal and fluids weights reported in Table 3 that from 0.2% and 8% of the initial monazite should dissolve to reach saturation (see Table 3).

The second process is the reequilibration of the chemical composition of the monazite with the fluid composition, for $P-T$ conditions imposed by the experiment.

The third process is attainment of textural equilibrium. In order to limit this problem, we abraded the grains. This eliminates sharp edges and corners, which are high-energy sites, but of course, the equilibrium shape for a monazite in a fluid is not that of a rugby ball (Fig. 1e,f), but that of a faceted crystal (Fig. 1g,h). It is impossible to evaluate quantitatively this process, but it will operate even when chemical equilibrium is reached, until such time when the textural equilibrium is reached.

Attainment of those three aspects of thermodynamics equilibrium is achieved through kinetic processes. Because of the high temperatures, we can neglect the diffusion in the fluid phase, and because we did not see the formation of some totally new grains (except ThO_2), we can disregard nucleation problems. We must then consider mainly volume diffusion in monazite and mineral/fluid interface kinetics. Volume diffusion is a process that tends to equilibrate the interior of the crystal with the surrounding. Mineral/fluid surface kinetics will control the dissolution of monazite and the reprecipitation at the surface of the existing grain. Surface diffusion could also operate for equilibrium shape attainment.

We should keep in mind that all these processes will compete during the run, the driving force being

chemical disequilibrium and surface energy, and the limiting factor being the kinetics.

5.2. Observational basis

The colour changed by the experiments (from yellowish orange to whitish grey) can be attributed to the "healing" of the nanometer-scale-distorted domains in monazite as a function of increasing temperature; complete healing is reached at 900 °C, 7 days (see Seydoux-Guillaume et al., 2002).

Even experiments at the very high temperature of 1200 °C (5 days in water) showed no resetting, neither by diffusion nor by dissolution/precipitation. For all runs, EMP traverses detected no diffusion profiles, and in particular no Pb-diffusion profile. This result was anticipated, if we consider the very low Pb-diffusion coefficient in monazite measured by Smith and Giletti (1997) and Cherniak et al. (2000). We can predict for these T time conditions (1200 °C, 5 days) a diffusion distance of $\sim$ 68 and $\sim$ 40 nm, respectively.

In all experiments thorium, was insoluble in fluids. The dissolution of monazite is definitely non-stoichiometric (or incongruent) and most of the time, the Th liberated by monazite dissolution precipitates as ThO_2 on the surface of the grain (in the water experiments). However, in the experiments where the fluid is saturated in SiO_2, it seems that thorium was directly re-incorporated in the forming monazite as $ThSiO_4$ end-member (Franz et al., 1996; Van Emden et al., 1997; Förster, 1998a,b).

We interpret the strong chemical modifications only observed for the 1000 °C $CaCl_2$ experiment (Table 1 and Figs. 3–5) as resulting from a dissolution/precipitation mechanism that operated in this run. Only $\sim$ 20 grains were recovered from the initial 30, demonstrating that some grains were totally dissolved during the run. Because the P–T and chemical conditions in this run were different from the conditions of formation of the starting monazite, the newly formed monazite has a distinctly new composition. Because very little is known about the thermodynamics of REE-phosphate and other monazite end-members, we cannot discuss in more detail the change in composition and the formation of the Th-rich domain. However, it seems likely that the starting monazite dissolved up to interface (1) and then began to crystallize from (1) to the grain margin (Fig. 4). Because Th is very insoluble in the fluid, the first monazite that recrystallized was enriched in $ThSiO_4$ and because Y, HREE and U are less compatible, this initial product was depleted in these elements. Then, during the crystallisation process a progressive enrichment in U, Y and HREE was initiated [between (1) and (2)—see Fig. 3].

An important observation from this experiment was that Pb was not reincorporated into the newly formed monazite. This confirms the results of Teufel and Heinrich (1997), who showed that recrystallisation is associated with strong discordancy. Finally, no self-diffusion of Pb or inter-diffusion of Ca–Pb were observed, even at the interface between the two zones where the optimal conditions for such diffusion were present. Relative to solid state diffusion, dissolution/precipitation is clearly a more efficient, faster mechanism for inducing discordancy.

The intense Pb loss observed in the experiments using $CaCl_2$ fluid (68% discordancy) and $SrCl_2$ (16% discordancy) underline the importance of the fluid composition in resetting process. However, in the run at 1000 °C with $SrCl_2$, neither overgrowths (SEM) nor chemical heterogeneity (EMP) were observed. We cannot say at present if such discordancy results from outward Pb diffusion, from Sr–Pb exchange diffusion, or from the formation of small, undetected, Pb-free overgrowth. Neither dissolution features nor diffusion profiles were observed using SEM and EMP, respectively. However, according to the very low Pb-diffusion coefficient, it would not be realistic to associate this discordancy with a diffusion process.

Our most surprising result comes from the Pb-enriched fluid experiments. We must stress, however, that those experiments do not mimic any "normal" geologic environment, as nature seldom provides such extremely Pb-enriched fluid. SEM images clearly show that dissolution/precipitation was active at 1000 °C (Fig. 1h), but not at 800 °C. Surprisingly, the effect of Pb standard is weaker at 1000 °C, as shown in the concordia diagrams (Fig. 6e). We saw previously that the estimated percentage of monazite dissolved at 1000 °C is about 10 times higher than at 800 °C (Table 3). Therefore, in the 1000 °C experiment, the Pb in the initial fluid would have been more diluted after monazite dissolution. Therefore, in the 1000 °C experiment, the initial Pb isotopic composi-

tion was modified by mixing with the initial Pb composition coming from the dissolved monazite. In this run, the remaining monazite grains interacted not with the NBS 982, but with the modified fluid. Because the Pb isotopic composition of the fluid was no longer NBS 982, the discordancy induced by this interaction is less visible. However, we must say that at present, we do not know how this interaction operates.

On the $^{208}Pb/^{206}Pb$ vs. $^{207}Pb/^{206}Pb$ diagram (Fig. 6f), it is clearly shown that the lower $^{208}Pb/^{206}Pb$ and higher $^{207}Pb/^{206}Pb$ ratios are related to an exchange between the Pb standard fluid and the Pb-containing starting monazite. However, both the 800 and 1000 °C treated monazites plot significantly below the mixing line between the starting monazite and the NBS Pb standard. This implies that the decrease in ^{208}Pb relative to ^{206}Pb and ^{207}Pb is not the product just of a simple exchange mechanism. We do not understand, up to now, the mechanism that produces such fractionation. We do not think that this could be related to a chemical or isotopic heterogeneity, as we see that the initial monazite is very homogeneous (EMP and ID-TIMS). The present data suggest that some isotopic fractionation is possible during monazite dissolution. A possible process to explain this unusual feature would be the preferential dissolution of some highly damaged domain with peculiar isotopic composition, although this model is not supported by what is known about radiation damage effects in monazite (Ewing, 1975; Meldrum et al., 1998; Ewing et al., 2000; Seydoux-Guillaume et al., 2002). Considerable further work involving fluid analyses will be necessary to elucidate this point.

6. Conclusions

Significant dissolution/precipitation and corresponding discordancy occurred only for experiments with $CaCl_2$ or Pb-bearing fluids at 1000 °C. In the case of experiments with a $SrCl_2$ fluid, the effect was much weaker. Diffusion profiles were not discernable for any element, including Pb. We conclude that dissolution/precipitation is a more efficient mechanism than diffusion to modify the U–Pb monazite system. Its efficiency depends both on the fluid composition and temperature. At this point, it is interesting to compare the different behaviours of monazite and zircon during hydrothermal alteration. Geisler et al. (2001) showed the effect of metamictization on the hydrothermal stability of zircon. They show a selective leaching by the solutions from metamict zircon. In this case, the structural properties (metamict state) of the zircon controls leaching. In contrast, hydrothermal alteration of monazite, which is not metamict, will be mainly controlled by the chemistry of the solution and the temperature.

The presence of Ca in the fluid has major consequences for the U–Pb isotopic system of monazite. In nature, monazite frequently occurs as inclusions in plagioclase, garnet, or apatite. In this case, circulation of a fluid in the rock could mobilise the Ca from the host phase which could result in a partial or total resetting of monazite (De Wolf et al., 1993; Braun et al., 1998; Montel et al., 2000). Because Th is poorly soluble in fluids, this element should be reincorporated into the monazite structure as brabantite or huttonite end-members, favouring the recrystallisation of a Th-rich and Pb-free rim. In natural samples, such Th-rich zones frequently occur. These latter are often younger, i.e., contain a lower Pb content than the adjacent domains (Cocherie et al., 1998; Crowley and Ghent, 1999). In the presence of intense deformation, it is possible to obtain discordant U–Pb monazite ages, resulting from new overgrowths of Pb-free monazites produced by dissolution/precipitation (Krohe and Wawrzenitz, 2000). Because Pb-volume diffusion in monazite is slow under most natural conditions, volume diffusion is unlikely to contribute significantly to discordance. Other processes such as recrystallisation are more important. Therefore, fluid occurrences and compositions, and textural positions of the monazite in the rock (Paquette et al., 1999; Montel et al., 2000) have to be considered when interpreting any data set.

Acknowledgements

We would like to thank very much Moacyr Marinho who kindly provide us the monazite sample. We thank B. Wunder and R. Schulz for their help with the experiments using piston cylinder. Thanks to D. Rhede and O. Appelt for help with EMP analyses and imaging and U. Glenz for SEM. Our thanks go to

E.M. Schemmert who produced good grain mounts. Travels for the authors were supported by PROCOPE. We would like to thank D. Cherniak, T. Geisler and an anonymous reviewer for their constructive comments. Many thanks to John Hanchar for his excellent editorial work. **[EO]**

Appendix A. SIMS analytical details

Images used a 12.7-kV, 20-nA, $^{16}O^-$ primary beam which was rastered over an area of 150×150 μm. Samples were cleaned in ethanol, dried at 75 °C and coated with a conductive gold film prior to analysis. The selected area for imaging was initially pre-sputtered in order to remove the gold coat. Digital image acquisition, employing a resistive anode encoder, involved peak-stepping 20 times through the cycle: ^{1}H (8 s), ^{28}Si (8 s), ^{31}P (8 s), ^{40}Ca (8 s), ^{89}Y (8 s), ^{140}Ce (8 s), ^{206}Pb (60 s), ^{208}Pb (30 s), ^{232}Th (8 s), ^{238}U (30 s). Total analytical time per imaged area was thus some 65 min. For these analyses, the mass spectrometer was operated at low-mass resolving power employing a 10-kV secondary ion extraction potential in conjunction with a 50-V energy bandpass. In order to suppress artefacts due both to sample charging as well as from polyatomic ions, an 80-V bias was applied to the sample. The field-of-view for our images was circa 75 μm in diameter and our spatial resolution was better than 2 μm.

References

Bertrand, J.M., Roddick, J.C., Van Kranendonk, M.J., Ermanovics, I., 1993. U–Pb geochronology of deformation and metamorphism across a central transect of the Early Proterozoic Torngat Orogen, North River map area, Labrador. Can. J. Earth Sci. 30, 1470–1489.

Black, L.P., Fitzgerald, F.D., Harley, S.L., 1984. Pb isotopic composition, colour, and microstructure of monazites from a polymetamorphic rock in Antarctica. Contrib. Mineral. Petrol. 85, 141–181.

Braun, I., Montel, J.M., Nicollet, C., 1998. Electron microprobe dating of monazites from high-grade gneisses and pegmatites of the Kerala Khondalite Belt, southern India. Chem. Geol. 146, 65–85.

Cherniak, D.J., Watson, E.B., Harrison, T.M., Grove, M., 2000. Pb diffusion in monazite: a progress report on a combined RBS/SIMS study. EOS Trans. AGU 81, S25 Spring Meeting Supplement.

Childe, F., Doig, R., Gariépy, C., 1993. Monazite as a metamorphic chronometer, south of the Grenville Front, western Quebec. Can. J. Earth Sci. 30, 1056–1065.

Cocherie, A., Legendre, O., Peucat, J.J., Kouamelan, A.N., 1998. Geochronology of polygenetic monazites constrained by in situ electron microprobe Th–U–total lead determination: implications for lead behaviour in monazite. Geochim. Cosmochim. Acta 62, 2475–2497.

Copeland, P., Parrish, R.R., Harrison, T.M., 1988. Identification of inherited radiogenic Pb in monazite and its implications for U–Pb systematics. Nature 333, 760–763.

Corfu, F., 1988. Differential response of U–Pb systems in coexisting accessory minerals, Winnipeg River Subprovince, Canadian Shield: implications for Archean crustal growth and stabilization. Contrib. Mineral. Petrol. 98, 312–325.

Crowley, J.L., Ghent, E.D., 1999. An electron microprobe study of the U–Th–Pb systematics of metamorphosed monazite: the role of Pb diffusion versus overgrowth and recrystallization. Chem. Geol. 157, 285–302.

Cruz, M.J., Cunha, J.C., Merlet, C., Sabaté, P., 1996. Datação pontual das monazitas da região de Itambé, Bahia, através da microssonda electrônica. XXXIX Congresso Brasileiro de Geologia, vol. 2. Sociedade Brasileira de Geologià-Núcleo, Bahià-Segipe, pp. 206–209.

Devidal, J.L., Gibert, F., Kieffer, B., Pin, C., Montel, J.M., 1998. A new method for solubility measurement: application to $NdPO_4$–NaCl–HCl hydrothermal fluids. Goldsmith Conference Toulouse 1998. Mineral. Mag., vol. 62A, pp. 375–376.

De Wolf, C.P., Belshaw, N., O'Nions, R.K., 1993. A metamorphic history from micron-scale $^{207}Pb/^{206}Pb$ chronometry of Archean monazite. Earth Planet. Sci. Lett. 120, 207–220.

Dodson, M.H., 1973. Closure temperature in cooling geochronological and petrological systems. Contrib. Mineral. Petrol. 40, 257–259.

Ewing, R.C., 1975. The crystal chemistry of complex niobium and tantalum oxides: IV. The metamict state: discussion. Am. Mineral. 60, 728–733.

Ewing, R.C., Meldrum, A., Wang, L.M., Wang, S.X., 2000. Radiation-induced amorphization. In: Ribbe, P.H. (Ed.), Rev. Mineral. Geochem., vol. 39. Mineralogical Society of America, Washington, DC, pp. 319–361.

Förster, H.J., 1998a. The chemical composition of REE–Y–Th–U-rich accessory minerals in peraluminous granites of the Erzgebirge–Fichtelgebirge region, Germany: part I. The monazite–(Ce)–brabantite solid solution series. Am. Mineral. 83, 259–272.

Förster, H.J., 1998b. The chemical composition of REE–Y–Th–U-rich accessory minerals in peraluminous granites of the Erzgebirge–Fichtelgebirge region, Germany: part II. Xenotime. Am. Mineral. 83, 1302–1315.

Franz, G., Andrehs, G., Rhede, D., 1996. Crystal chemistry of monazite and xenotime from Saxothuringian–Moldanubian metapelites, NE Bavaria, Germany. Eur. J. Mineral. 8, 1097–1118.

Geisler, T., Ulonska, M., Schleicher, H., Pidgeon, R.T., van Bronswijk, W., 2001. Leaching and differential recrystallization of

metamict zircon under experimental hydrothermal conditions. Contrib. Mineral. Petrol. 141, 53–65.

Grove, M., Harrison, T.M., 1999. Monazite Th–Pb age depth profiling. Geology 27, 487–490.

Harrison, T.M., McKeegan, K.D., LeFort, P., 1995. Detection of inherited monazite in the Manaslu leucogranite by $^{208}Pb/^{232}Th$ ion microprobe dating: crystallization age and tectonic implications. Earth Planet. Sci. Lett. 133, 271–282.

Kalt, A., Corfu, F., Wijbrans, J.R., 2000. Time calibration of a $P–T$ path from a Variscan high-temperature low-pressure metamorphic complex (Bayerische Wald, Germany), and the detection of inherited monazite. Contrib. Mineral. Petrol. 128, 143–163.

Krogh, T.E., 1982. Improved accuracy of U–Pb zircon ages by the creation of more concordant systems using an air abrasion technique. Geochim. Cosmochim. Acta 46, 637–649.

Krohe, A., Wawrzenitz, N., 2000. Domainal variations of U–Pb monazite ages and Rb–Sr whole-rock dates in polymetamorphic paragneisses (KTB Drill Core, Germany): influence of strain and deformation mechanisms on isotope systems. J. Metamorph. Geol. 18, 271–291.

Landzirotti, A., Hanson, G.N., 1995. U–Pb dating of major and accessory minerals formed during metamorphism and deformation of metapelites. Geochim. Cosmochim. Acta 59, 2513–2526.

Meldrum, A., Boatner, L.A., Weber, W.J., Ewing, R.C., 1998. Radiation damage in zircon and monazite. Geochim. Cosmochim. Acta 62, 2509–2520.

Montel, J.M., Foret, S., Veschambre, M., Nicollet, C., Provost, A., 1996. Electron microprobe dating of monazite. Chem. Geol. 131, 37–53.

Montel, J.M., Kornprobst, J., Vielzeuf, D., 2000. Preservation of old U–Th–Pb ages in shielded monazite: example from the Beni Bousera Hercynian kinzigites (Morocco). J. Metamorph. Geol. 18, 335–342.

Paquette, J.L., Montel, J.M., Chopin, C., 1999. U–Th–Pb dating of the Brossasco ultrahigh-pressure metagranite, Dora–Maira massif, western Alps. Eur. J. Mineral. 11, 69–77.

Parrish, R.R., 1987. An improved micro-capsule for zircon dissolution in U–Pb geochronology. Chem. Geol., Isot. Geosci. 66, 99–102.

Parrish, R.R., 1990. U–Pb dating of monazite and its application to geological problems. Can. J. Earth Sci. 27, 1431–1450.

Parrish, R.R., 1995. Thermal evolution of the southeastern Canadian Cordillera. Can. J. Earth Sci. 32, 1618–1642.

Pin, C., Paquette, J.L., 1997. A mantle-derived bimodal suite in the Hercynian Belt: Nd isotope and trace element evidence for a subduction-related rift origin of the Late Devonian Brévenne metavolcanics, Massif Central (France). Contrib. Mineral. Petrol. 129, 222–238.

Poitrasson, F., Chenery, S., Bland, D.J., 1996. Contrasted monazite hydrothermal alteration mechanisms and their geochemical implications. Earth Planet. Sci. Lett. 145, 79–96.

Poitrasson, F., Chenery, S., Shepherd, T.J., 2000. Electron microprobe and LA-ICP-MS study of monazite hydrothermal alteration: implications for U–Th–Pb geochronology and nuclear ceramics. Geochim. Cosmochim. Acta 64, 3283–3297.

Rubatto, D., Williams, I.S., Buick, I.S., 2001. Zircon and monazite response to prograde metamorphism in the Reynolds Range, central Australia. Contrib. Mineral. Petrol. 140, 458–468.

Schärer, U., Xu, R.H., Allègre, C.J., 1986. U–(Th)–Pb systematics and ages of Himalayan leucogranites, South Tibet. Earth Planet. Sci. Lett. 77, 35–48.

Seydoux, A.M., Montel, J.M., Paquette, J.L., Marinho, M., 1999. Experimental study of the resetting of the U–Th–Pb geochronological system of monazite. EUG X, Terra Nova 10 (Abstract Supplement 1), p. 800.

Seydoux-Guillaume, A.M., Wirth, R., Nasdala, L., Gottschalk, M., Montel, J.M., Heinrich, W., 2002. XRD, TEM and Raman study of experimental annealing of natural monazite. Phys. Chem. Mineral. 29, 240–253.

Shannon, R.D., 1976. Revised effective ionic radii and systematic studies of interatomic distances in halide and chalcogenides. Acta Crystallogr. 32, 751–767.

Simpson, R.L., Parrish, R.R., Searle, M.P., Waters, D.J., 2000. Two episodes of monazite crystallization during metamorphism and crustal melting in the Everest region of the Nepalese Himalaya. Geology 28, 403–406.

Smith, H.A., Barreiro, B., 1990. Monazite U–Pb dating of staurolite grade metamorphism in pelitic schists. Contrib. Mineral. Petrol. 105, 602–615.

Smith, H.A., Giletti, B.J., 1997. Lead diffusion in monazite. Geochim. Cosmochim. Acta 61, 1047–1055.

Suzuki, K., Adachi, M., 1994. Middle Precambrian detrital monazite and zircon from the Hida gneiss on Oki-Dogo Island, Japan: their origin and implications for the correlation of basement gneiss of southwest Japan and Korea. Tectonophysics 235, 277–292.

Suzuki, K., Adachi, M., Kajizuka, I., 1994. Electron microprobe observations of Pb diffusion in metamorphosed detrital monazites. Earth Planet. Sci. Lett. 128, 391–405.

Teufel, S., Heinrich, W., 1997. Partial resetting of the U–Pb isotope system in monazite through hydrothermal experiments: an SEM and U–Pb isotope study. Chem. Geol. 137, 273–281.

Townsend, K.J., Miller, C.F., D'Andrea, J.L., Ayers, J.C., Harrison, T.M., Coath, C.D., 2001. Low temperature replacement of monazite in the Ireteba granite, Southern Nevada: geochronological implications. Chem. Geol. 172, 95–112.

Van Emden, B., Thornber, M.R., Graham, J., Lincoln, F.J., 1997. The incorporation of actinides in monazite and xenotime from placer deposits in western Australia. Can. Mineral. 35, 95–104.

Vielzeuf, D., Montel, J.M., 1994. Partial melting of metagreywackes: part I. Fluid-absent experiments and phase relationships. Contrib. Mineral. Petrol. 117, 375–393.

Williams, M.L., Jercinovic, M.J., Terry, M.P., 1999. Age mapping on the electron microprobe: deconvoluting multistage tectonic histories. Geology 27, 1023–1026.

Zhu, X.K., O'Nions, R.K., 1999. Zonation of monazite in metamorphic rocks and its implications for high temperature thermochronology: a case study from the Lewisian terrain. Earth Planet. Sci. Lett. 171, 209–220.

Zhu, X.K., O'Nions, R.K., Belshaw, N.S., Gibb, A.J., 1997. Significance of in situ SIMS chronometry of zoned monazite from the Lewisian granulites, northwest Scotland. Chem. Geol. 135, 5–35.

Geology; November 2003; v. 31; no. 11; p. 973–976; 4 figures.

Transmission electron microscope study of polyphase and discordant monazites: Site-specific specimen preparation using the focused ion beam technique

Anne-Magali Seydoux-Guillaume* Institut für Planetologie, Wilhelm-Klemm-Strasse 10, 48149 Münster, Germany
Philippe Goncalves* Université Blaise-Pascal, Laboratoire Magmas et Volcans-CNRS, 5 rue Kessler, 63038 Clermont-Ferrand, France
Richard Wirth GeoForschungsZentrum-Potsdam, Division 4, Telegrafenberg, 14473 Potsdam, Germany
Alexander Deutsch Institut für Planetologie, Wilhelm-Klemm-Strasse 10, 48149 Münster, Germany

ABSTRACT

Electron-microprobe (EMP) U-Th-Pb dating on polyphase and discordant monazites from polymetamorphic granulites of the Andriamena unit (north-central Madagascar) reveals inconsistent chemical ages. To explain these drastic variations, transmission electron microscopy (TEM) foils were prepared directly from thin sections by using the focused ion beam technique. The most important result of the TEM study is the demonstration of the presence of small (~50 nm) Pb-rich domains where large variations in EMP ages occur. We suggest that radiogenic Pb was partially reincorporated in monazite during the recrystallization at 790 Ma. Because the excited volume of EMP is ~4 μm^3, U-Th-Pb dating yielded various apparent older ages without geological significance. In addition, TEM analysis of the foils revealed the presence of an ~150-nm-wide amorphous zone along the grain boundary of monazite and its host quartz. This Fe-Si-Al–rich phase may have formed as a result of fluid activity at 500 Ma, and the phase's amorphous state may be due to the irradiation from U and Th decay in the monazite. This demonstrates for the first time the enormous potential of the TEM investigations on site-specific specimens prepared with the focused ion beam technique for the interpretation of geochronological data.

Keywords: monazite, discordance, focused ion beam, transmission electron microscopy, U-Th-Pb ages, Madagascar.

Transmission electron microscope study of polyphase and discordant monazites: Site-specific specimen preparation using the focused ion beam technique

Anne-Magali Seydoux-Guillaume* Institut für Planetologie, Wilhelm-Klemm-Strasse 10, 48149 Münster, Germany
Philippe Goncalves* Université Blaise-Pascal, Laboratoire Magmas et Volcans-CNRS, 5 rue Kessler, 63038 Clermont-Ferrand, France
Richard Wirth GeoForschungsZentrum-Potsdam, Division 4, Telegrafenberg, 14473 Potsdam, Germany
Alexander Deutsch Institut für Planetologie, Wilhelm-Klemm-Strasse 10, 48149 Münster, Germany

ABSTRACT

Electron-microprobe (EMP) U-Th-Pb dating on polyphase and discordant monazites from polymetamorphic granulites of the Andriamena unit (north-central Madagascar) reveals inconsistent chemical ages. To explain these drastic variations, transmission electron microscopy (TEM) foils were prepared directly from thin sections by using the focused ion beam technique. The most important result of the TEM study is the demonstration of the presence of small (~50 nm) Pb-rich domains where large variations in EMP ages occur. We suggest that radiogenic Pb was partially reincorporated in monazite during the recrystallization at 790 Ma. Because the excited volume of EMP is ~4 μm³, U-Th-Pb dating yielded various apparent older ages without geological significance. In addition, TEM analysis of the foils revealed the presence of an ~150-nm-wide amorphous zone along the grain boundary of monazite and its host quartz. This Fe-Si-Al–rich phase may have formed as a result of fluid activity at 500 Ma, and the phase's amorphous state may be due to the irradiation from U and Th decay in the monazite. This demonstrates for the first time the enormous potential of the TEM investigations on site-specific specimens prepared with the focused ion beam technique for the interpretation of geochronological data.

Keywords: monazite, discordance, focused ion beam, transmission electron microscopy, U-Th-Pb ages, Madagascar.

INTRODUCTION

In polymetamorphic terranes, most studies combining electron-microprobe (EMP) U-Th-Pb dating (EMP chemical ages) with conventional isotopic techniques have shown that monazites behave as a closed system (Crowley and Ghent, 1999; Terry et al., 2000; Williams and Jercinovic, 2002). Other authors, however, reported large variations in EMP ages, inconsistent with discrete episodic growth of monazite (Montel et al., 1996; Braun et al., 1998; Cocherie et al., 1998; Catlos et al., 2002; Goncalves, 2002; Fig. 1). Two explanations are given for this observation: (1) partial Pb loss from monazite by diffusion or leaching, implying that the EMP age data represent minimum ages, or (2) overlapping measurement of different age domains by the EMP, resulting in mixed apparent ages. The aim of this study was to elucidate the reason for inconsistent EMP ages, reported for polyphase monazites from ultrahigh-temperature (UHT) granulites of north-central Madagascar (Goncalves, 2002; Paquette et al., 2003). This goal was achieved by using transmission electron microscopy (TEM).

*E-mail: Seydoux-Guillaume—seydoux@uni-muenster.de. Present address: Goncalves—Geosciences Department, University of Massachusetts, Morrill Science Center, 611 North Pleasant Street, Amherst, Massachusetts 01003-9297, USA.

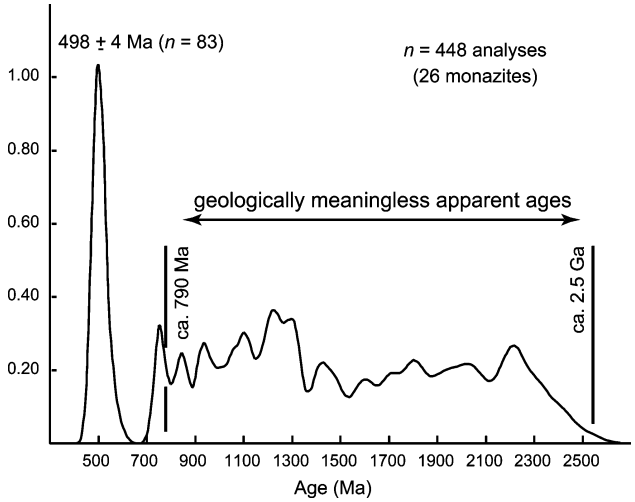

Figure 1. Weighted histogram of 448 electron microprobe (EMP) chemical U-Th-Pb ages for 26 monazites included in garnet, quartz, and coronitic textures. 2.5 Ga and 790 Ma ages were derived from isotope dilution–thermal ionization mass spectrometer data; 500 Ma age is from EMP data on monazite overgrowths. Note continuous range of EMP ages between 2500 and 790 Ma (after Goncalves, 2002).

DESCRIPTION OF THE PROBLEM

The investigated monazites record three distinct episodes of crystallization: at 2.5 Ga under UHT conditions, ca. 790 Ma, related to hydration and retrograde metamorphism of the UHT assemblages, and at 500 Ma, during a growth episode due to late fluid circulation under low amphibolite facies conditions (Goncalves, 2002). The succession of events was revealed by textural studies, EMP chemical dating (Fig. 2), and isotope dilution–thermal ionization mass spectrometer (ID-TIMS) dating of extracted selected grains. The ID-TIMS dating yielded discordant ages defining a mixing array involving the 2500, 790, and 500 Ma age components, and a geologically meaningless lower intercept ca. 580 Ma (Goncalves, 2002, Paquette et al., 2003).

The EMP ages, however, do not show a simple trimodal distribution reflecting the geological events at 2500, 790, and 500 Ma (Fig. 1). On the contrary, most grains are characterized by (1) meaningless apparent ages ranging continuously between 2500 and 790 Ma and (2) a very well defined unimodal population clustering at 500 Ma (Fig. 1). In addition, age dispersions are observed within single monazite grains. It is noteworthy that the grain ages scatter irregularly. In contrast, areas with an apparent age of 500 Ma systematically form small overgrowths, or internal domains close to small quartz inclusions, orthoamphibole, biotite, or cordierite.

Two questions remained unanswered after this combined in situ dating: what is the reason for largely varying apparent ages in a single monazite grain, and what is the difference between the well-defined 500 Ma overgrowths

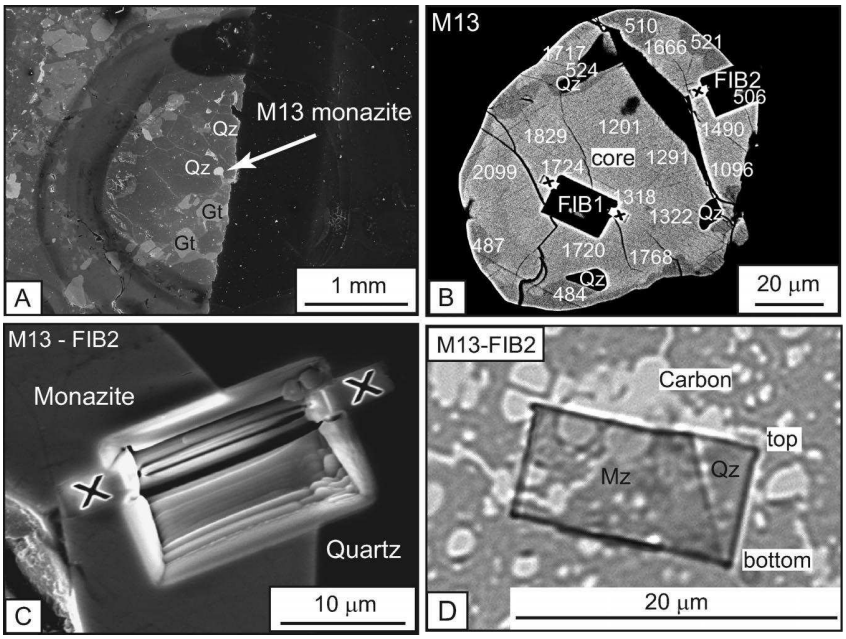

Figure 2. Preparation of transmission electron microscopy (TEM) foils from monazite M13 using focused ion beam (FIB) technique. A: Backscattered-electron (BSE) image of thin section with monazite M13 embedded in quartz (Qz) with associated garnet (Gt). B: Close-up BSE image of monazite M13. Bright areas (core) formed at 790 Ma; dark areas are 500 Ma overgrowths. Numbers are U-Th-Pb ages in Ma obtained by electron microprobe. C: Secondary-electron image of FIB milled trench with TEM foil removed. Foil was milled perpendicular to image plane along trace marked by crosses. D: Optical micrograph in transmitted light of TEM-ready FIB foil on perforated carbon film on copper grid. Foil dimensions are 15 μm × 7 μm × 130 nm.

and the domains showing geologically meaningless ages? Nanometer-scale investigations to solve these problems required preparation of TEM foils—ultrathin, ultrasmall tabular sections—from defined areas in monazite grains that have been dated by the EMP technique (Figs. 2B and 3A). For this purpose, we applied the focused ion beam (FIB) milling technique.

METHODS

Focused Ion Beam (FIB) Technique

The FIB preparation technique is designed to produce site-specific TEM foils, ~15–20 μm × 10–15 μm, and ~100 nm thick (for technical details, see Overwijk et al., 1993; Young, 1997; Roberts et al., 2001). Milling occurs by using gallium ions accelerated to 30 keV. Carbon coating of the TEM-ready foil is not necessary, because it rests on carbon foil. The FIB allows cutting a TEM-ready foil in a section from a well-defined area such as mineral boundary, without preferential thinning or production of artifacts (e.g., Fig. 4D). Homogeneous sample thickness is very favorable, especially for acquisition of elemental maps or line scans (Figs. 3C and 3D). The TEM foil is cut perpendicular to the surface of the sample (Figs. 2C and 2D), allowing the gathering of information with respect to the depth of the specimen. In the current context, this aspect is particularly useful for testing the reliability of specific EMP age data.

The site-specific specimens for this study were prepared with the FEI FIB200 instrument at the GeoForschungsZentrum (GFZ)-Potsdam. Figure 2 illustrates subsequent stages of the preparation.

Transmission Electron Microscope (TEM)

TEM studies were carried out with the Philips CM200 TEM at the GFZ-Potsdam, and the JEOL 3010 TEM of the Interdisciplinary Center for Electron Microscopy and Microanalysis (ICEM), University of Münster. The JEOL 3010, operating at 300 kV, was used for conventional TEM. The Philips CM200, equipped with an energy-dispersive X-ray analyzer (EDAX) with an ultrathin window, was used for energy-dispersive X-ray (EDX) analysis and EDX mapping. Acceleration voltage was 200 kV, and the electron source was a LaB_6 filament. Point analyses were carried out with a spot size of ~4 nm; the counting time for EDX point analysis was 200 s, and 45 ms per step in EDX mapping.

SAMPLE DESCRIPTION

Two monazite grains (M13 and M26) were selected for the TEM study. (For simplicity we relabeled these grains, labeled by Goncalves [2002] M13′ and M26″.) These monazites are representative for the whole population because they display the typical bimodal age distribution. Both grains were originally located in polygonal recrystallized quartz within the rock matrix. The 110 μm monazite M26 displays a chemically distinct core, surrounded by a homogeneous rim and isolated small overgrowths (Fig. 3A). The distributions of EMP age data in core and rim are similar, scattering continuously from 1805 to 911 Ma (Fig. 3A). In contrast, overgrowths yielded systematically younger dates, ca. 500 Ma. As shown in the backscattered-electron (BSE) image (Fig. 2B), the 160 μm monazite M13 revealed only two domains: (1) a large core and (2) darker areas located at the rim and at the contact with quartz inclusions. These areas with an average age of 504 ± 15 Ma are interpreted as younger recrystallized domains. The EMP ages in the core range from 2099 to 1096 Ma.

On the basis of these EMP ages and ID-TIMS results, Goncalves (2002) interpreted the cores of M13 and M26 as 2.5 Ga monazites, which underwent partial Pb loss during the 790 Ma event. Goncalves further suggested that the rim on monazite M26 was formed by dissolution followed by precipitation at 790 Ma, despite the older ages obtained by EMP. The overgrowth crystallized ca. 500 Ma.

NANOSCALE INVESTIGATIONS OF MONAZITE WITH COMPLEX AGES

In monazite M13, the TEM foil FIB1 was extracted from the old core, and foil FIB2 includes the core and the dark area giving consistent 500 Ma ages (Fig. 2B). In M26, foil FIB1 covers core and rim (Fig. 3A).

Structural State

Bright-field (BF) images of all domains in these monazites consistently show a typical pattern, i.e., mottled diffraction contrasts due to the presence of distorted volumes (Fig. 4B; cf. Black et al., 1984; Seydoux-Guillaume et al., 2002a). These lattice defects are produced by self-irradiation due to the α-decay of U and Th. An important observation is the lack of significant difference in defect concentration in the 500 Ma domains and the old cores of both monazites. Note the presence of mottled diffraction contrasts in quartz as well; these are also due to lattice defects, which are probably caused by irradiation related to U and Th decay in the monazite (Fig. 4D).

Nanometer-Sized Pb-Rich Domains

Many ~50-nm-sized domains were observed in the core and the rim of monazite M26 (Fig. 3B) and in the core of monazite M13 (Fig. 4C). Figure 3D shows EDX mapping results for Pb in M26. The lead is not homogeneously distributed (Fig. 3D): the dark domains labeled 2 and 3 and one fluid inclusion (Fig. 3B) are enriched in Pb (Fig. 3D). The EDX point

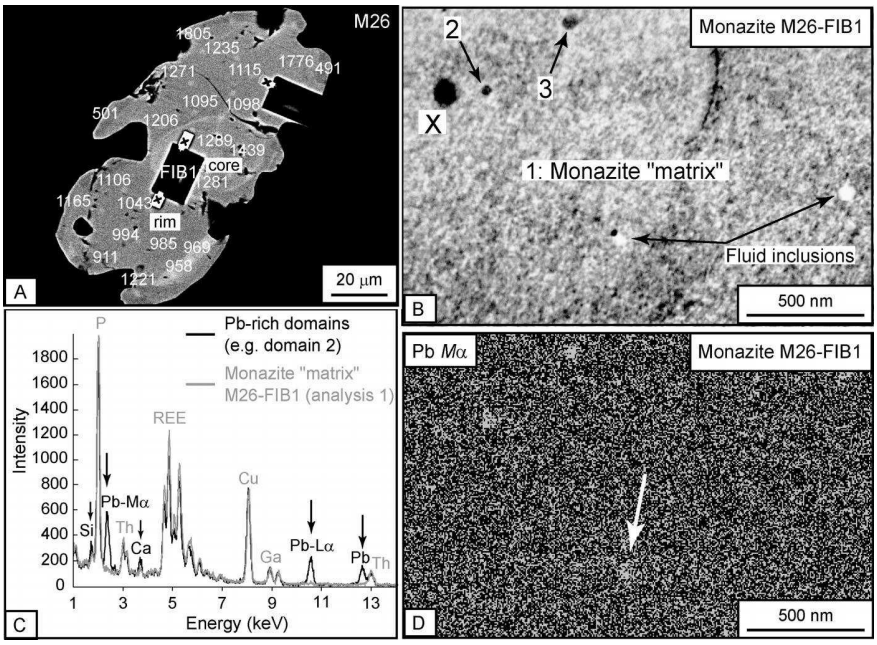

Figure 3. Energy-dispersive X-ray (EDX) analysis of monazite M26. A: Backscattered-electron (BSE) image. Foil FIB1 covers core and slightly darker rim. Numbers correspond to electron microprobe (EMP) ages. B: Bright-field (BF) transmission electron microscope (TEM) image of monazite core in FIB1 foil (see A). Note dark domains 2 and 3 and two fluid inclusions. Dark domain X corresponds to contamination of foil with Ga ions dispersed during focused ion beam (FIB) milling. Mottled diffraction contrasts are due to distorted volumes in monazite lattice (cf. Fig. 4B). C: Overlay of analysis 1 of monazite matrix and representative EDX analysis of dark domain in B is reported. As TEM foil has fairly uniform thickness, analyzed volumes are same, allowing direct comparison of two analyses. Compared to monazite matrix, dark domains are very enriched in Pb and, to lesser extent, in Ca and Si. Cu and Ga are preparation artifacts. REE—rare earth elements. D: EDX map of Pb*Mα* for area shown in B. Domains 2 and 3 and one fluid inclusion (arrow) are enriched in Pb (brighter in this image) compared to monazite matrix.

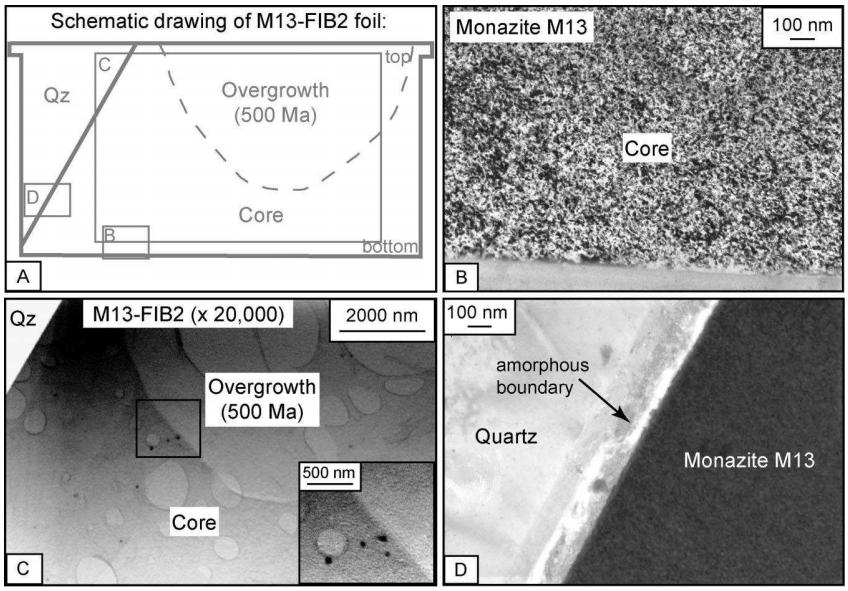

Figure 4. Transmission electron microscope (TEM) images of FIB2 foil, monazite M13. A: Schematic drawing shows different zones and locations of details given in B–D. B: Bright-field (BF) image of part of core region, showing mottled diffraction contrasts. C: BF image showing monazite, old core, with largely varying U-Th-Pb ages, and young overgrowth, together with host mineral, quartz (Qz). Bright circles correspond to holes in perforated carbon supporting TEM foil. Note small Pb-rich domains in core (dark areas in rectangle; see enlargement on lower right). D: BF image of boundary between quartz and monazite. Note presence of ~150-nm-wide amorphous phase and mottled diffraction contrasts in quartz due to lattice defects.

analysis (Fig. 3C) corroborates this observation: compared to the monazite matrix, the inclusions are considerably enriched in Pb and, to a lesser extent, in Ca and Si. Because the electron beam of the TEM covers both inclusions and monazite matrix, the precise chemical composition of the Pb-rich domains could not be determined. The core of monazite M13 yields similar results. In contrast, Pb-rich domains seem to be absent in the 500 Ma overgrowths (Fig. 4).

Phase Boundary Between Monazite and Quartz

The FIB technique permits analysis of defined, few-nanometers-small areas and inclusions, which usually are destroyed during conventional TEM preparation methods (ion milling). This fundamental advantage helped to study the phase boundary between monazite and quartz in monazite M13 (TEM foil FIB2; Figs. 2D, 4A, 4C, and 4D). At the micrometer scale (Fig. 2C), this boundary looks very narrow and sharp. At the nanometer scale, however, the interface is ~150 nm wide. It consists of an amorphous phase (Fig. 4D), which according to EDX analysis, is composed of O, Fe, and Si in approximately the same proportions, and, to a lesser extent, Al.

DISCUSSION AND IMPLICATIONS

α-Decay Damages

Goncalves (2002) explained the range in apparent ages by partial Pb loss from 2.5 Ga monazites. Clearly, in such old monazites, self-irradiation due to α-decay from U and Th must have induced more defects than that in the 500 Ma overgrowths, and Pb is probably much more mobile in such a distorted lattice than in a perfect one (Cherniak, 1993). In the present case, however, zones with different ages have a similar concentration of defects, making enhanced Pb mobility due to different structural states highly improbable.

Implication of the Presence of Pb-Rich Inclusions

The occurrence of nanometer-sized Pb-rich domains in monazites has strong implications for EMP dating. The main advantage of EMP dating is the high spatial resolution: at conventional analytical conditions, the excited volume is ~4 μm^3, which is very small compared to single-grain U-Pb ID-TIMS dating (Montel et al., 1996; Paquette and Pin, 2001), yet relatively large on the TEM scale. By using the EMP dating technique, it is not possible to exclude nanometer-sized Pb-rich domains from the analysis. In chemical dating, all Pb is considered to be of in situ radiogenic origin; hence, inclusion of Pb-rich domains in the analysis yields an older apparent age.

On the basis of these arguments, the interpretation of Goncalves (2002)—that the cores

of both M26 and M13 grain are partially reset 2.5 Ga monazites—is reconsidered. We now assume that the 2.5 Ga monazites dissolved and recrystallized at 790 Ma. All apparent ages older than 790 Ma result from mixing of the 790 Ma domains with Pb-rich domains, which contain inherited radiogenic Pb from the 2.5 Ga monazite. This surprising outcome emphasizes that special care must be taken in interpreting chemical zoning visible in BSE images in terms of different monazite generations.

The nature of the Pb-rich domains is not understood. They could (1) be a pure Pb-Ca-Si-O phase like margarosanite ($Ca_2PbSi_3O_9$), (2) represent material that crystallized in fluid inclusions (Fig. 3B), or (3) be a local domain in the monazite structure, high in lead, like the brabantite [$PbTh(PO_4)_2$] experimentally synthesized by Montel et al. (2002).

Goncalves (2002) documented some 2.5 Ga monazites that survived the 790 Ma event as inclusions in garnet. In the rock matrix, however, these old monazites were probably affected by dissolution followed by precipitation at 790 Ma, when cordierite + orthoamphibole + biotite formed at the expense of garnet + quartz. The newly formed 790 Ma monazite incorporated radiogenic Pb, previously released during the dissolution of the 2.5 Ga monazite. The EMP U-Th-Pb ages indicate a heterogeneous distribution of this old radiogenic lead. Generally, incorporation of Pb depends on its distribution coefficient between the different phases involved in the reaction. For example, Pb would be concentrated in fluids relative to monazite and in monazite relative to garnet or quartz. In hydrothermal experiments, monazite releases or incorporates Pb from a fluid depending on the relative concentrations and the external conditions (Seydoux-Guillaume et al., 2002b). Although we cannot exclude incorporation of the old radiogenic Pb in the form of brabantite into the monazite structure, we prefer the interpretation that this Pb is concentrated in nanometer-sized Pb-rich domains. Regardless of the precise location of the radiogenic Pb in the monazite, the important implication for dating is the fact that domains of unsupported Pb exist in monazite.

Role of the Fluid in Resetting Monazites

The boundary between monazite and its host quartz is not a sharp contact between pure crystalline phases, but lined with an amorphous phase (Fig. 4D), the exact nature of which is unknown. We propose this phase to be an indicator of fluid activity. It could be a low-temperature phase (a clay mineral) or an amphibolite facies mineral, that later became metamict by irradiation from adjacent monazite. In the thin section shown in Figure 2, monazite M13 is included in quartz, but this grain was not completely armored; overgrowths on the monazite record the 500 Ma event (Fig. 2B). We emphasize that all these young overgrowths are localized either at the monazite-quartz interface or close to quartz inclusions (e.g., the 524 and 484 Ma domains in Fig. 2B). We tentatively conclude that the event that yielded these monazite overgrowths took place ca. 500 Ma during late fluid circulation under low amphibolite facies conditions (Goncalves, 2002). The boundary between monazite and quartz acted as the channel for fluid circulation. Our observations confirm the major role of fluids in the resetting of monazites (Teufel and Heinrich, 1997; Seydoux-Guillaume et al., 2002a; Villa, 2002).

CONCLUSIONS

In U-Th-Pb dating of minerals from polymetamorphic terranes, the combined use of different methods is extremely useful. Possible analytical techniques include single-grain ID-TIMS and EMP U-Th-Pb dating of petrographically and chemically characterized crystals as well as TEM observations (Seydoux-Guillaume et al., 2002a; Villa, 2002). The behavior of U-Th-Pb systems in minerals during metamorphism at the single-grain scale is currently poorly understood. For example, Romer and Rötzler (2003) provided an example of a titanite that inherited the radiogenic signature of its precursor mineral rutile. In this, the TEM study of site-specific FIB foils resulted in a new understanding of EMP ages for monazites from a polymetamorphic terrane: the range in apparent ages is not the consequence of partial Pb loss, a process commonly used for interpretation, but instead is due to the incorporation of various amounts of radiogenic Pb during recrystallization of the monazites. The development of more sophisticated, more precise geochronologic techniques requires a strong effort in the understanding of what really happens to the isotopic systems in dated minerals.

ACKNOWLEDGMENTS

This work was supported by German Science Foundation (DFG) grant De 401/18-1 to Deutsch. We appreciate technical assistance by F. Bartschat and T. Grund. C. Nicollet is acknowledged for providing the unusual samples. We thank J.M. Montel and M.L. Williams for reviewing an early draft of the manuscript, and J. Connelly and D. Waters for their constructive formal reviews.

REFERENCES CITED

Black, L.P., Fitzgerald, F.D., and Harley, S.L., 1984, Pb isotopic composition, colour, and microstructure of monazites from a polymetamorphic rock in Antarctica: Contributions to Mineralogy and Petrology, v. 85, p. 141–181.

Braun, I., Montel, J.M., and Nicollet, C., 1998, Electron microprobe dating of monazite from high-grade gneisses and pegmatites of the Kerala Khondalite belt, southern India: Chemical Geology, v. 146, p. 65–85.

Catlos, E.J., Gilley, L.D., and Harrison, T.M., 2002, Interpretation of monazite ages obtained via in situ analysis: Chemical Geology, v. 188, p. 193–215.

Cherniak, D.J., 1993, Lead diffusion in titanite and preliminary results on the effect of radiation damage on Pb transport: Chemical Geology, v. 110, p. 177–194.

Cocherie, A., Legendre, O., Peucat, J.J., and Kouamelan, A.N., 1998, Geochronology of polygenetic monazites constrained by in situ electron microprobe Th–U–total lead determination: Implications for lead behaviour in monazite: Geochimica et Cosmochimica Acta, v. 62, p. 2475–2497.

Crowley, J.L., and Ghent, E.D., 1999, An electron microprobe study of the U-Th-Pb systematics of metamorphosed monazite: The role of Pb diffusion versus overgrowth and recrystallisation: Chemical Geology, v. 157, p. 285–302.

Goncalves, P., 2002, Pétrologie et géochronologie des granulites de ultra-hautes temperatures de l'unité basique d'Andriamena (Centre-Nord Madagascar): Apport de la géochronologie in situ U-Th-Pb à l'interprétation des trajets *P-T* [thèse de doctorat]: Clermont-Ferrand, France, Université Blaise-Pascal, 319 p.

Montel, J.M., Foret, S., Veschambre, M., Nicollet, C., and Provost, A., 1996, Electron microprobe dating of monazite: Chemical Geology, v. 131, p. 37–53.

Montel, J.M., Devidal, J.L., and Avignant, D., 2002, X-ray diffraction study of brabantite-monazite solid solutions: Chemical Geology, v. 191, p. 89–104.

Overwijk, M.H.F., van den Heuvel, F.C., and Bulle-Lieuwma, C.W.T., 1993, Novel scheme for the preparation of transmission electron microscopy specimens with a focused ion beam: Journal of Vacuum Science and Technology, v. 11, p. 202.

Paquette, J.L., and Pin, C., 2001, A new miniaturized extraction chromatography method for precise U-Pb zircon geochronology: Chemical Geology, v. 176, p. 311–319.

Paquette, J.L., Goncalves, P., Devouard, B., and Nicollet, C., 2003, In situ ID-TIMS U-Pb dating of single monazites: A new method to unravel complex poly-metamorphic evolutions. Application to the UHT granulites of Andriamena (north-central Madagascar): Contributions to Mineralogy and Petrology (in press).

Roberts, S., McCaffrey, J., Giannuzzi, L., Stevie, F., and Zaluzec, N., 2001, Advanced techniques in TEM specimen preparation, *in* Xiao-Feng Zhang and Ze Zhang, eds., Progress in transmission electron microscopy, Volume 1: Springer Series in Surface Sciences, v. 38, p. 336–342.

Romer, R.L., and Rötzler, J., 2003, Effect of metamorphic reaction history on the U-Pb dating of titanite: Geological Society [London] Special Publication (in press).

Seydoux-Guillaume, A.M., Wirth, R., Nasdala, L., Gottschalk, M., Montel, J.M., and Heinrich, W., 2002a, An XRD, TEM and Raman study of experimentally annealed natural monazite: Physics and Chemistry of Minerals, v. 29, p. 240–253.

Seydoux-Guillaume, A.M., Paquette, J.L., Wiedenbeck, M., Montel, J.M., and Heinrich, W., 2002b, Experimental resetting of the U-Th-Pb system in monazite: Chemical Geology, v. 191, p. 165–181.

Terry, M.P., Robinson, P., Hamilton, M.A., and Jercinovic, M.J., 2000, Monazite geochronology of UHP and HP metamorphism, deformation, and exhumation, Nordoyane, Western Gneiss region, Norway: American Mineralogist, v. 85, p. 1651–1664.

Teufel, S., and Heinrich, W., 1997, Partial resetting of the U-Pb isotope system in monazite through hydrothermal experiments: An SEM and U-Pb isotope study: Chemical Geology, v. 137, p. 273–281.

Villa, I., 2002, Where is geochronology going? Alteration and mineral mixtures: Geochimica et Cosmochimica Acta, v. 66, no. S1, p. A807.

Williams, M.L., and Jercinovic, M.J., 2002, Microprobe monazite geochronology: Putting absolute time into microstructural analysis: Journal of Structural Geology, v. 24, p. 1013–1028.

Young, R.J., 1997, Application of the focused ion beam in materials characterization and failure analysis: Microstructural Science, v. 25, p. 491–496.

Manuscript received 12 February 2003
Revised manuscript received 18 July 2003
Manuscript accepted 29 July 2003

Printed in USA

European Journal of Mineralogy (2007), **19**, 7–14.

Contrasting response of $ThSiO_4$ and monazite to natural irradiation

ANNE-MAGALI SEYDOUX-GUILLAUME[1,*], RICHARD WIRTH[2] and JANNICK INGRIN[1]

[1]LMTG, UMR 5563 CNRS – Université Paul Sabatier – IRD, 14 avenue Edouard Belin, 31400 Toulouse, France
*Corresponding author, e-mail: seydoux@lmtg.obs-mip.fr
[2]GeoForschungsZentrum (GFZ) Potsdam-Division 4, Telegrafenberg, 14473 Potsdam, Germany

Abstract: In order to compare the irradiation-induced behaviour of monazite and $ThSiO_4$, a large single crystal of monazite from Norway (Arendal monazite) containing several $ThSiO_4$ inclusions was investigated. The estimated theoretical self-irradiation dose received by monazite near those inclusions was approximately 3 x 10^{19} α-decay/g. Transmission electron microscopy (TEM) analyses were performed on both host and inclusion. The TEM samples were prepared by the focused ion beam (FIB) technique. Monazite and $ThSiO_4$ were found to have very different textures, including the presence of an amorphous zone between them. Crystalline monazite showed mottled diffraction contrast, which is characteristic of irradiation damage in this mineral. Observations suggest that there is a maximum defect density in monazite which cannot be exceeded. It is unlikely that some natural monazite can surpass this defect density. In contrast, $ThSiO_4$ is completely amorphous and exhibits an unusual spherical, bubble-like texture. The size of these spheres is in the range of 10 to 200 nm. It is proposed that $ThSiO_4$ is composed of aggregated spheres very similar to a gel. The zone between these two phases was certainly amorphized due to irradiation induced by α-decay of Th and U. It could be a preferential alteration zone and act as high-diffusive pathway for elements.

Key-words: monazite, amorphous thorium silicate, TEM, FTIR, natural irradiation, aggregate spheres.

Eur. J. Mineral.
2007, **19**, 7–14

Contrasting response of $ThSiO_4$ and monazite to natural irradiation

ANNE-MAGALI SEYDOUX-GUILLAUME[1,*], RICHARD WIRTH[2] and JANNICK INGRIN[1]

[1]LMTG, UMR 5563 CNRS – Université Paul Sabatier – IRD, 14 avenue Edouard Belin, 31400 Toulouse, France
*Corresponding author, e-mail: seydoux@lmtg.obs-mip.fr
[2]GeoForschungsZentrum (GFZ) Potsdam-Division 4, Telegrafenberg, 14473 Potsdam, Germany

Abstract: In order to compare the irradiation-induced behaviour of monazite and $ThSiO_4$, a large single crystal of monazite from Norway (Arendal monazite) containing several $ThSiO_4$ inclusions was investigated. The estimated theoretical self-irradiation dose received by monazite near those inclusions was approximately 3 x 10^{19} α-decay/g. Transmission electron microscopy (TEM) analyses were performed on both host and inclusion. The TEM samples were prepared by the focused ion beam (FIB) technique. Monazite and $ThSiO_4$ were found to have very different textures, including the presence of an amorphous zone between them. Crystalline monazite showed mottled diffraction contrast, which is characteristic of irradiation damage in this mineral. Observations suggest that there is a maximum defect density in monazite which cannot be exceeded. It is unlikely that some natural monazite can surpass this defect density. In contrast, $ThSiO_4$ is completely amorphous and exhibits an unusual spherical, bubble-like texture. The size of these spheres is in the range of 10 to 200 nm. It is proposed that $ThSiO_4$ is composed of aggregated spheres very similar to a gel. The zone between these two phases was certainly amorphized due to irradiation induced by α-decay of Th and U. It could be a preferential alteration zone and act as high-diffusive pathway for elements.

Key-words: monazite, amorphous thorium silicate, TEM, FTIR, natural irradiation, aggregate spheres.

Introduction

The study of radioactive minerals, such as monazite, zircon, thorite, uraninite is of great interest for both U-Pb age dating (see review in Speer, 1982, and Harrison *et al.*, 2002) and the problem of nuclear waste storage of high activity elements (see review in Ewing *et al.*, 2000, and Ewing & Wang, 2002). Because of their high actinide (U and Th) contents, these minerals received intense self-irradiation doses during their geological history. During an α-decay event, an α-particle (helium nucleus) is ejected, while the remaining nucleus (recoil nucleus) is recoiled in the opposite direction. The α-particle is ejected to 10–40 μm (Owen, 1988; Ewing *et al.*, 1995; Ewing *et al.*, 2000; Nasdala *et al.*, 2001b) and dissipates most of its energy by ionisation along its path, with limited elastic collisions occurring at the end of its trajectory (Nasdala *et al.,* 2001a). It produces isolated defects made of several hundred atomic displacements. The recoil nucleus travels through 10–20 nm according to the principle of momentum conservation, and causes collision cascades made of a few thousand atomic displacements (Gögen & Wagner, 2000; Nasdala *et al.*, 2001b). Collision cascade due to recoil of nucleus, the main cause of amorphization of a crystal lattice, are caused by α-recoil nuclei (*e.g.*, Ewing *et al.*, 1995; Nasdala *et al.*, 1996; Weber *et al.*, 1998; Ewing *et al.*, 2000). Long-time integration of these atomic-scale interactions produces macroscopic effects such as swelling and bubble formation due to accumulation of helium (Ewing *et al.*, 2000).

In minerals relevant for U-Pb dating, radiation damage may partially or totally destroy the crystal lattice, dramatically changing their physical and chemical properties (*e.g.*, Weber *et al.*, 1998; Ewing *et al.*, 2000; Geisler *et al.*, 2005) and modifying the kinetics of resetting. It was, for example, suggested that Pb diffusion is enhanced in a metamict crystal (Cherniak, 1993) because radiogenic Pb diffuses much faster within "channels" that correspond to the percolating interface between amorphous and crystalline domains (*e.g.*, Geisler *et al.*, 2002; Salje, 2000; Trachenko *et al.*, 2000; Geisler *et al.*, 2003; 2004). Moreover, radiogenic Pb can be leached more easily from a damaged lattice (Davis & Krogh, 2000; Romer, 2003). Consequently, a damaged lattice will retain radiogenic Pb to a lesser degree than a perfect one, resulting in discordant ages for phases that exist in such a structural state. Micro-nano-structural investigations are therefore of fundamental importance to better understand isotopic ages of minerals (Seydoux-Guillaume *et al.*, 2003; 2004). Characterising the structural state of U- and Th-rich phases is also essential when considering their potential use in nuclear waste deposit strategies. Monazite-based ceramics are currently studied as a crystalline waste form for immobilization actinides (*e.g.*, Meldrum *et al.*, 1998; Poitrasson *et al.*, 1996; 2000; 2002; Read & Williams, 2001; Montel *et al.*, 2002; Oelkers & Poitrasson, 2002). For these stud-

DOI: 10.1127/0935-1221/2007/0019-007
0935-1221/07/0019-007 $ 3.60

ies, natural monazite provides data on long-term damage accumulation at low dose rates.

The monoclinic ($P2_1/n$) light rare-earth orthophosphate monazite (APO_4: A=LREE, Th, U, Ca, Pb) contains high concentrations of U and Th (up to 6 wt. % UO_2 and 20 wt. % ThO_2; *e.g.*, Montel *et al.*, 1996; Förster, 1998; Seydoux-Guillaume *et al.*, 2002a). Up to now, amorphous monazites have never been found despite of the fact that they experienced high radiation doses (Ewing, 1975), well above the critical dose required for amorphization. In natural monazite, clear evidence of radiation damage was limited to isolated nm-sized domains within the crystal (Black *et al.*, 1984; Meldrum *et al.*, 1998; Seydoux-Guillaume *et al.*, 2002b; 2003; 2004).

The two polymorphs of $ThSiO_4$, thorite and huttonite, have the zircon ($I4_1/amd$) and monazite structure types, respectively (Pabst & Hutton, 1951; Taylor & Ewing, 1978). It seems that they have an opposite behaviour to irradiation. Thorite has been found mostly in a metamict (*i.e.* amorphous) state (Pabst, 1952; Lumpkin & Chakoumakos, 1988; Farges & Calas, 1991), whereas the rare huttonite has always been crystalline (Speer, 1982; Förster *et al.*, 2000). However, it is always difficult to be sure that amorphous $ThSiO_4$ was previously thorite, since the only criterion to distinguish thorite from the huttonite is the crystalline structure. The aim of the study was to compare the behaviour of monazite and $ThSiO_4$ inclusions to irradiation. Two kinds of irradiation were considered: monazite and $ThSiO_4$ inclusion self irradiation, and irradiation from one mineral to the other (external irradiation). Nano-structural investigations of minerals were performed by using TEM.

Sample description

A large (several centimetres) reddishbrown, dull and opaque single crystal of monazite from Arendal, Norway was used for this study. The sample comes from the collection of the "Muséum National d'Histoire Naturelle" in Paris. A piece of this crystal was prepared for microscopic studies (optical, scanning electron microscopy (SEM), and TEM). Optical observations of thin sections showed that the crystal is full of orange to red inclusions (iron oxides?). Back scattered electron microscope (BSE) images and energy dispersive X-ray (EDX) analysis (Fig. 1) of the monazite crystal showed its chemical heterogeneity. A part of the crystal (Mnz1) is enriched in Th (BSE image brighter, Fig. 1A) as compared to the rest of the crystal (Mnz2), which is also full of cracks and contains many bright (Th) and dark inclusions (Xe). Results from EDX analyses re-

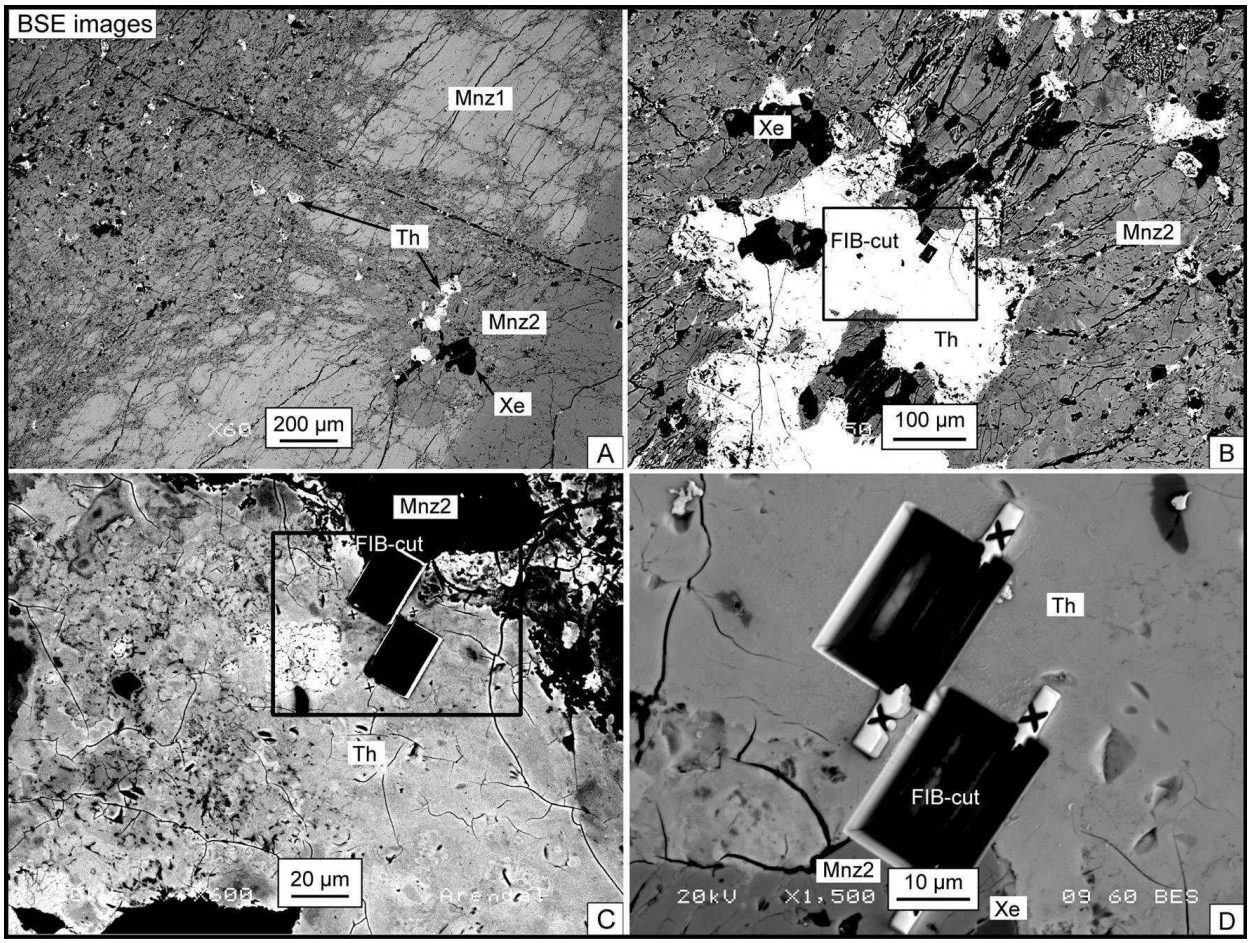

Fig. 1. Back-scattered electron (BSE) images of thorium silicate inclusions in a monazite sample. (A) Part of the monazite sample showing its chemical heterogeneity: Mnz_2 (dark grey) is depleted in Th compare to Mnz_1 (bright grey), and full of cracks, bright (Th) and dark inclusions (Xe). (B) Image of the large $ThSiO_4$ inclusion studied here. (C) Enlargement of area within the thorium silicate inclusion. (D) BSE image of two FIB-milled trenches with the TEM-foil removed. Foils were milled perpendicular to image plane along the trace marked by crosses. The size of the foil covers both monazite (Mnz_2) and $ThSiO_4$ (Th). Foil dimensions are ~18 µm × 8 µm × 130 nm. (Xe) is for xenotime.

vealed that (Xe) corresponds to the YPO_4 xenotime and (Th) to a thorium silicate, probably thorite or huttonite. Many radiating fractures are visible around $ThSiO_4$ inclusions (Fig. 1B and Fig. 4A). Electron microprobe analysis (EPMA) showed that the monazite crystal ($Mnz_1 + Mnz_2$) is heterogeneous in composition (Table 1), with a ThO_2 range of 3–13 wt.%, of 1200–6000 ppm PbO, and 400–7500 ppm UO_2. The estimated U-Th-Pb age (for method see Montel *et al.*, 1996) is ~930 +/- 17 Ma. As we do not know the exact location of our monazite sample, it was not possible to provide an independent age date for the host rock. However, the U-Th-Pb estimated age given by our monazite is in agreement with ID-TIMS ages – in the range of 920–1200 Ma – from this region (Bingen *et al.*, 2005). This results in an estimated theoretical self-irradiation dose received by monazite to be in the range of 2 to 18 x 10^{19} α-decay/g (after Nasdala *et al.*, 2001b). Close to the $ThSiO_4$ inclusions, monazite (Mnz_2) is systematically depleted in Th (Table 1, Fig. 1A). From the composition (Table 1) and the corresponding U-Th-Pb age of ~930 Ma, theoretical self-irradiation doses received by monazite near $ThSiO_4$ inclusions was estimated to be ~3.3 x 10^{19} α-decay/g. This value is quite high and similar to those calculated for previously studied monazites from "Moacir" and "Madagascar" samples (Seydoux-Guillaume *et al.*, 2002b; 2004).

Thorium silicate inclusions are very unstable under the electron beam. The BSE image on Fig. 1C shows an unusual mottled-texture mineral. The bright area left from the FIB-cut trench is damaged region generated by the electron beam after microprobe analysis under 15 kV and 20 nA. This is probably due to the presence of water inside $ThSiO_4$ (Farges & Calas, 1991; Lumpkin & Chakoumakos, 1988). From the composition (Table 1) and the same U-Th-Pb age as the cogenetic Th-depleted monazite (930 Ma), theoretical self-irradiation doses received by $ThSiO_4$ inclusion was estimated to be ~5 x 10^{20} α-decay/g. This mineral accumulates a considerable dose, about 15 times higher than the high dose accumulated in monazite.

The aim of the study is to compare the behaviour of monazite and $ThSiO_4$ inclusions with respect to natural irradiation. An article in preparation will explain in detail the mode of formation of these $ThSiO_4$ inclusions within monazite. The present paper will not deal with the chemical relationship between the monazite and $ThSiO_4$ inclusions.

Analytical methods

Focused-Ion-Beam (FIB) Technique

Because the aim of the study was to investigate the nanostructure of the monazite, the thorium silicate inclusions, and the contact-zone between these two phases, a site-specific preparation method for TEM analysis was needed. This method is called Focused Ion Beam and creates TEM foils, ~15–20 µm by 10–15 µm, and ~100 nm thick (for technical details, see, Overwijk *et al.*, 1993; Young, 1997; Roberts *et al.*, 2001; Seydoux-Guillaume *et al.*, 2003; Wirth, 2004). Milling occurs using gallium ions accelerated to 30 keV. The TEM foil is cut perpendicular to the surface of the sample (Fig. 1D), which provides information with respect to the depth of the specimen. Artefacts from FIB preparation, like redeposition of sputtered material and gallium onto the foil surface (see EDX spectra, Fig. 3) are described in Wirth (2004). The specimens were prepared with the FEI FIB200 instrument at the GeoForschungsZentrum (GFZ)-Potsdam.

Table 1. Electron microprobe analyses of monazite 1 (mean of 10 analyses), monazite 2 (8 analyses) and $ThSiO_4$ inclusion (5 analyses). See Fig. 1A for analysis location.

wt.%	Monazite 1	Monazite 2	$ThSiO_4$
SiO_2	2.05	0.43	16.45
P_2O_5	26.65	29.06	0.46
CaO	0.91	0.84	2.00
Y_2O_3	2.23	0.20	0.42
La_2O_3	11.14	12.57	0.00
Ce_2O_3	25.53	30.00	0.01
Pr_2O_3	3.09	3.61	0.11
Nd_2O_3	10.63	13.80	0.12
Sm_2O_3	2.05	2.86	0.04
Gd_2O_3	1.54	1.82	0.10
Dy_2O_3	0.69	0.25	0.28
ThO_2	11.97	4.00	62.99
UO_2	0.67	0.10	7.12
PbO	0.56	0.18	0.10
Total	99.71	99.72	90.20

Transmission Electron Microscope (TEM)

The TEM studies were carried out with the Philips CM200 TEM at the GFZ-Potsdam, operating at 200 keV, and the Philips CM30 TEM of the University of Lille (USTL), operating at 300 kV. Both microscopes were equipped with an energy-dispersive X-ray analyzer (EDX) with ultra-thin windows, and LaB_6 filaments as electron sources.

Fourier Transformed Infra-Red spectroscopy (FTIR)

We used a Fourier transform spectrometer with an attached microscope (Nicolet 5700 and Continuµm microscope from Thermo electron). Both spectrometer and microscope were purged with dry air during analyses to minimize atmospheric contamination. An MCT detector cooled by liquid nitrogen was used to collect 256 scans at a resolution of 8 cm^{-1} between 4000 and 650 cm^{-1} from an un-polarized infrared beam with a spot size of 20 x 20 μm^2. The FTIR observations were done on another piece of Arendal monazite cut to a ~30 µm thickness and doubly polished. Analyses were done on the large $ThSiO_4$ inclusion in monazite visible in Fig. 4A. The IR profile (Fig. 4B) was done at a spacing of 20 µm.

Results

The TEM sample was cut both from the monazite and from the thorium silicate inclusion as shown in the SEM images

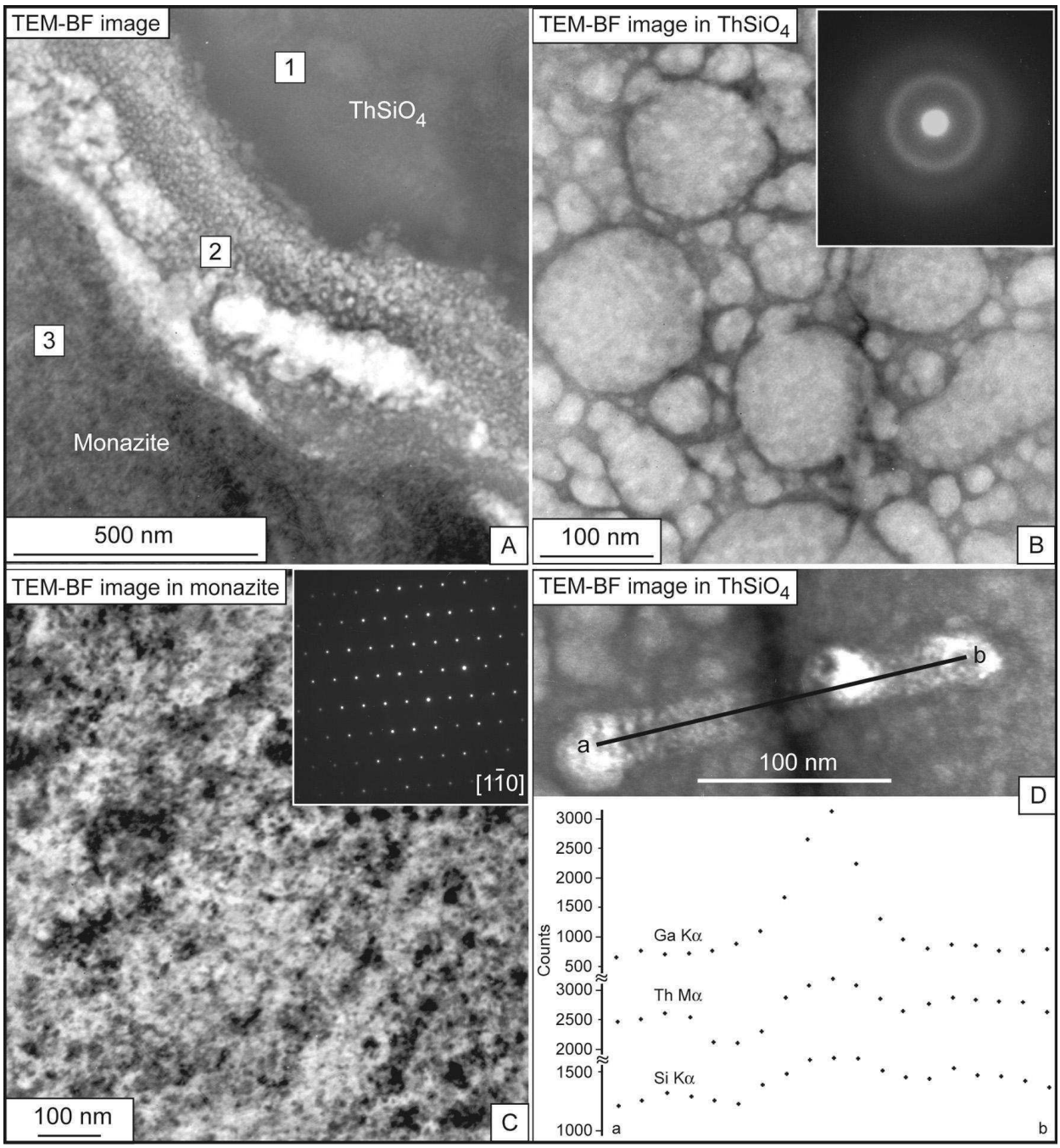

Fig. 2. TEM-bright field (TEM-BF) images of TEM- foil displayed in Fig. 1D. (A) Image of the three domains observed within the sample. (1) $ThSiO_4$ inclusion, (2) amorphous grain boundary layer and (3) monazite "matrix". (B) Image from inside $ThSiO_4$ inclusion with corresponding diffraction pattern (inset). Note the bubble-like texture of $ThSiO_4$ and its diffraction pattern displaying an amorphous structure. (C) Image from inside monazite close to $ThSiO_4$ inclusion with corresponding diffraction pattern (inset). Note the typical mottled contrast for this mineral and the diffraction pattern suggesting it is crystalline. (D) EDX profile (from a to b) across a large sphere showing clear enrichment in gallium (dark rim). Note correlation from Th and Si along profile showing thin thickness variation within the sample. BF image on the top shows localization of the profile and intense beam damage (holes + contamination) of the sample after the traverse. (conditions: 300 kV TEM, 10 s/point, 20 points)

in Fig. 1. The foil was milled perpendicular to the image plane along the trace marked by the two crosses and is ~18 μm long, 8 μm high and 130 nm thick. There is actually no direct contact between monazite (3) and thorium silicate (1) (Fig. 2A). A ~400 nm wide zone (2) is visible on the TEM bright field (BF) image. The EDX analyses (Fig. 3) performed in domains (1) and (3) are in agreement with electron microprobe analysis. The zone intermediate area (2) is enriched in Th, Fe and Si together with some P and Pb. Electron diffraction patterns from this interface demonstrate that it is amorphous. The TEM-BF images from monazite and thorium silicate (Figs. 2B and C) reveal very different microtextures. Monazite shows mottled diffraction contrast, which is characteristic for this mineral (Black *et al.*, 1984; Seydoux-Guillaume *et al.*, 2002b; 2003; 2004). They are the result of a mosaic structure of the crystal, *i.e.*, a lattice comprising many smaller domains that have slightly different orientations. The dark areas represent domains oriented close to a zone axis, and the bright ones are regions that are not diffracting. However, the lattice distortions seem to be too limited to be visible on the selected area diffraction (SAD) patterns – no arcing or defocusing of the reflections

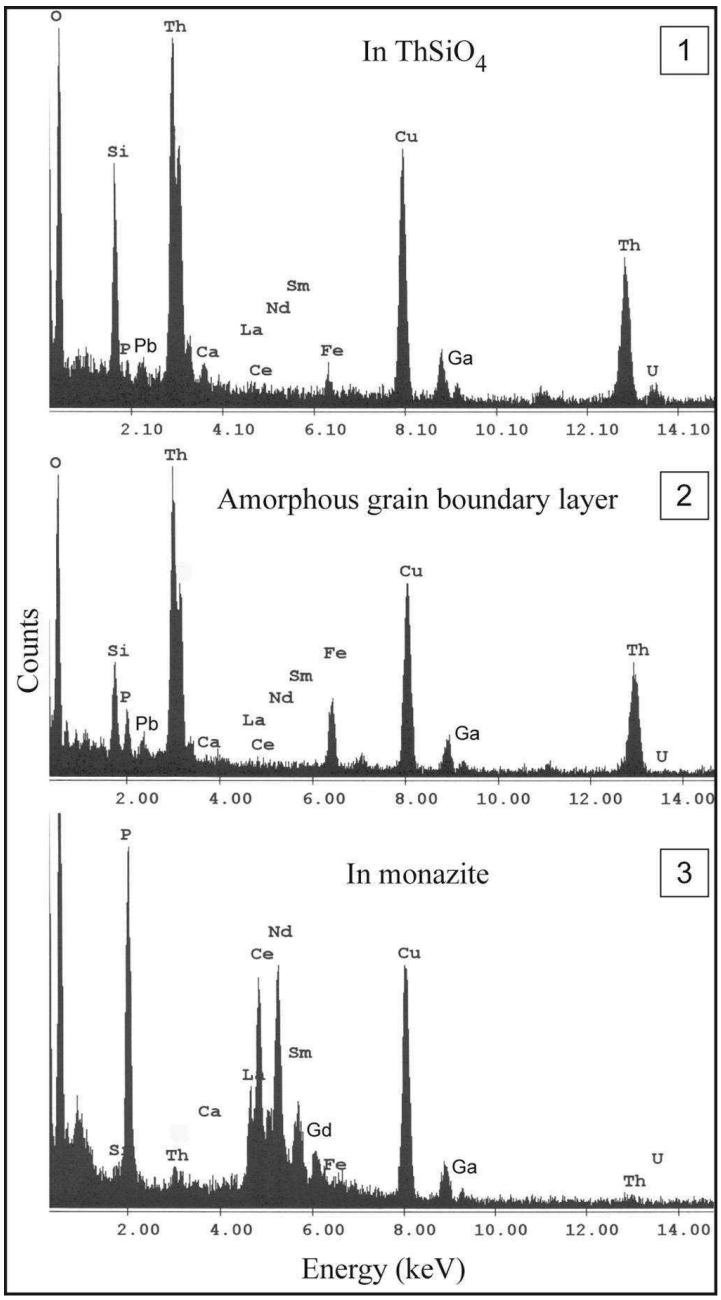

Fig. 3. TEM-Energy dispersive X-Ray (EDX) spectra acquired from the different domains (1, 2 and 3) of TEM-foil. Numbers are the same as in Fig. 2A and correspond to the location of each point analysis. Cu intensity is due to secondary fluorescence from the copper grid and Ga intensities are caused by implanted or redeposited gallium.

were observed (Fig. 2C inset). The thorium silicate shows an unusual sphere-like texture; it is basically an agglomeration of spheres 10 to 200 nm in diameter. The rim of these spheres appears darker due to redeposition of gallium ions from FIB milling thus causing stronger mass absorption contrast (Fig. 2D). Another tremendous difference between these two phases is displayed in their electron diffraction patterns (inset in Fig. 2B and C). While monazite is still crystalline, the thorium silicate is totally amorphous. A diffraction pattern of the latter shows two diffuse scattering rings, the most intense at ~ 3.1 Å, which is characteristic for a metamict structure (Lumpkin & Chakoumakos, 1988). It is not possible to confirm that amorphous $ThSiO_4$ was thorite, since the original structure is gone. Because it is impossible to discriminate between thorite and huttonite, we will simply refer to them as $ThSiO_4$ inclusions.

The FTIR data clearly demonstrates presence of molecular water within the $ThSiO_4$ inclusions. The H-O-H bending mode of molecular water is systematically present at 1645 cm^{-1} and the spectra are fully saturated in the region of O-H stretching modes (3600–2900 cm^{-1}; Fig. 4B). The spectra are very similar to those found by Lumpkin & Chakoumakos (1988) for thorite from the Harding pegmatite.

Discussion

First we want to emphasize that the structural state of this monazite (fully crystallized) is approximately the same as the Moacir monazite previously studied by Seydoux-Guillaume *et al.* (2002b; 2004). Defect concentrations in the Arendal monazite lattice, very close to what is observed in the Moacir study, remain much reduced. A comparison between many monazites studied using TEM (Black *et al.*, 1984; Meldrum *et al.*, 1998; Seydoux-Guillaume *et al.*, 2002b; 2003; 2004), in terms of defect concentrations, are similar to the current study. Irradiation damage is limited and mottled textures visible in bright field images are very similar. From this, it seems that there is a maximum defect density in natural monazite which cannot be exceeded. It is unlikely to find some natural monazite surpassing this defect density. This makes it difficult to set up a classification scheme of self-irradiation-induced defect concentrations in monazite (Seydoux-Guillaume *et al.*, 2004).

Monazite and $ThSiO_4$ react completely different to irradiation damage. As mentioned above, monazite is always found in the crystalline state (Ewing, 1975; Black *et al.*, 1984; Meldrum *et al.*, 1998; Seydoux-Guillaume *et al.*, 2002b; 2003; 2004). However, based on the irradiation dose, monazite is expected to show much more irradiation defects than observed or to be amorphous. By comparison, other minerals like zircon, pyrochlore, zirconolite were amorphous over 1 x 10^{19} α-decay/g (see review in Ewing *et al.*, 2000). Furthermore, the results of irradiation studies carried out on silicates and phosphates with monazite or thorite structures showed that at room temperature, the amorphisation dose is similar for all the investigated structures. It shows that monazite is not specifically resistant to radiation damages. The main difference is the critical temperature (temperature above which amorphization cannot be induced). For monazite this temperature is in the range of 60 to 150°C, but is above 650°C for huttonite and above 700°C for thorite (Meldrum *et al.* 1999, 2000). Therefore, monazite is able to restore its structure at low temperature, although it is not specifically resistant to radiation damage. Another reason that explains the different behaviour of monazite and $ThSiO_4$ is the difference in bonding energy between P-O and Si-O (~200 kJ/mol) (Lumpkin & Chakoumakos, 1988). The energy barrier to recrystallization in a phosphate is much lower than in a silicate ($ThSiO_4$). Nevertheless, in this study, where monazite is in contact with the very radioactive $ThSiO_4$ (the dose received by $ThSiO_4$ is ~ 15 times higher than for monazite), monazite is still crystalline. There is no observable difference in terms of defect

concentration of monazite close to $ThSiO_4$ or far away from $ThSiO_4$. Although monazite receives irradiation both internally due to its own U and Th content, and externally due to the $ThSiO_4$ irradiation, monazite is always in the crystalline state. This confirms our assumption of a maximum accumulation of irradiation damages in monazite, presumably due to its rapid healing capability of irradiation damages (Seydoux-Guillaume *et al.*, 2004).

In contrast to monazite, $ThSiO_4$ is totally amorphous with an unusual spherical nanotexture (Fig. 2B). We propose two hypotheses to explain such a texture. Because helium is a product of the Th and U disintegration, it is suggested that $ThSiO_4$ is composed of an amorphous matrix with He-bubbles inclusions. Due to the very high amount of helium produced during α-decay of U and Th in $ThSiO_4$, and due to the amorphous state of this phase, helium is not incorporated in the $ThSiO_4$ phase but is segregated into bubbles. In the case of monazite, helium seems to be accommodated in the lattice (Seydoux-Guillaume *et al.*, 2002b; 2004) as interstitial atoms. Additionally, this bubble-like texture could also explain the instability of $ThSiO_4$ under the electron beam during EPMA analysis (Fig. 1C). The observed $ThSiO_4$ spherical-nanotexture is very unusual and was never observed in minerals before. The most similar textures within minerals we found in the literature were those observed in amorphous Nb-Ta-Ti oxides minerals like euxenite (Headley *et al.*, 1981) and in $CaZrTi_2O_7$ zirconolite (Ewing & Headley, 1983). The authors described their TEM observations as spherical microvoids and proposed that these voids were generated by helium accumulation caused by the internal α-decay. Except for the experimental work on helium-irradiated minerals (Johnson *et al.*, 2000; Carrez *et al.*, 2002a; b), there is no evidence that these spherical textures or microvoids contain helium. In the same way, little is known about the behaviour of helium in such minerals in terms of helium solubility, diffusion or its effect on mineral physical properties (Weber *et al.*, 1998). Nevertheless, such data are of great importance for the study of ceramics used for the immobilization of nuclear waste. A closer look at the texture suggests the observed $ThSiO_4$-texture is more like an aggregate of spheres than an assemblage of bubbles, as shown in the TEM BF image in Fig. 2B. In the TEM images, neither holes nor voids, similar to those observed by Headley *et al.* (1981) or Carrez *et al.* (2002b) were found. The $ThSiO_4$-texture does not show any space between the supposed bubbles and the entire inclusion is composed of aggregated spheres. We do not observe a disappearance of these "bubbles" by electron irradiation during TEM analysis as observed by Carrez *et al.* (2002b). Finally, because of the presence of cracks and due to the amorphous structure of $ThSiO_4$, it is improbable that helium accumulates within the $ThSiO_4$ inclusion but diffuses out of this phase and out of the sample. In the same way, Pb is not completely accumulated in the $ThSiO_4$ phase, giving a U-Th-Pb age younger (~30 Ma) than the 930 Ma expected. Therefore, we proposed another hypothesis, which assumes this texture to be a gel, *i.e.* amorphous, highly porous, aggregated spheres, and hydrated form of $ThSiO_4$. The presence of molecular water anticipated by the low totals of $ThSiO_4$ EPMA analyses (see also Farges & Calas, 1991 and Lumpkin & Chakoumakos, 1988) is definitely confirmed by FTIR analyses (Fig. 4B). Water can also explain the instability of $ThSiO_4$ under the electron beam during EPMA analysis (Fig. 1C), and the abundance of iron oxides observed in the sample at the boundaries between monazite and $ThSiO_4$ (Fig. 3) and filling cracks. The presence of cracks around the $ThSiO_4$ inclusions (Fig. 1A, B and 4A) could be due to volume expansion of the inclusions during amorphization. Large volume changes are usually associated with amorphization and are responsible for swelling and formation of cracks (*e.g.* for zircon; Holland & Gottfried, 1955; Murakami *et al.*, 1991). It is known, for example for zircon (an orthosilicate with the same structure as thorite) that radiation damage can induce volume expansions of 16–18 % (Weber *et al.*, 1998). Cracking induces free circulation of water into the $ThSiO_4$. The $ThSiO_4$ gel probably stays amorphous because the ambient temperatures were too low to promote healing (see the discussion above about critical temperature) and/or from the constant irradiation from Th and U decay. Finally, if there is a free circulation of water, it could be possible to dissolve helium and transport it out of the structure.

The 400 nm amorphous zone between monazite and $ThSiO_4$ has approximately the same composition as the thorium silicate inclusion, except with more P and Fe and less U and Si. A similar amorphous layer, 100 nm wide, was also observed between monazite and quartz from ultrahigh temperature granulites of North-Central Madagascar (Seydoux-Guillaume *et al.*, 2003). It is suggested that this layer formed due to irradiation originating from monazite and $ThSiO_4$. Irradiation (*via* α-recoil nuclei) could initiate lattice destruction at grain boundaries (destruction on ~20 nm), and after that, alteration could be intensified by fluids to form this 400 nm amorphous zone. This zone concentrated only some elements, *e.g.* Th, Si, and Pb coming from damage of $ThSiO_4$ and P from monazite (Fig. 3). The fact that the zone is depleted in REE, Ca and U, which are other constituents of monazite and thorium silicate (Fig. 3), suggests that these elements were removed and transported by fluids; Fe could also be transported by fluids. This layer must be a preferential alteration zone and acts as high-diffusive pathway, like what is known for zircon (Geisler *et al.*, 2002; 2003; 2004). A detailed study of the process responsible for the formation of $ThSiO_4$ inclusions and this amorphous zone will be subject of another paper in preparation.

Conclusions

The TEM study of Arendal monazite revealed a different response to irradiation for monazite and $ThSiO_4$. Monazite remains crystalline exhibiting the same mottled diffraction contrast as those previously observed and described in a large variety of monazites. This confirms our presumption of a maximum accumulation of irradiation damages in monazite, due to the rapid healing capability of irradiation damages. Thorium silicate is entirely amorphous and an unusual aggregation of spheres, similar to a $ThSiO_4$-(hydrated)-gel structure is revealed. The phase boundary between these two phases was certainly altered by irradiation induced by α-decay of both minerals. Irradiation affects the lattice of minerals by knock-

on damage and consequently favors amorphization. Such an unstable structure facilitates dissolution; this phase boundary constitutes a preferential alteration zone and high-diffusive pathway for elements and fluids.

In addition, some aspects revealed by this study need further investigation. Experimental work on helium irradiation in monazite and $ThSiO_4$ is also missing if we want to understand the behaviour of helium in such minerals. Is it accumulated or accommodated in these minerals? What are the modifications on mineral properties induced by helium? Yet, such data are of great importance both for the study of ceramics used for immobilization of nuclear waste and for geochronological and petrological interpretations.

Acknowledgements: We are indebted to Michel Guiraud and Museum National d'Histoire Naturelle de Paris for the monazite sample. A part of the TEM analyses were possible thanks to the INSU/CNRS Microscope National Facility at LSPES in Lille, with the help of Ahmed Addad and Hugues Leroux. We thank Fabienne de Parseval for her meticulous preparation of FTIR sample, Jean-Marc Montel for reviewing an early draft of the manuscript, and G.R. Lumpkin, K.J. Livi and J.M. Hanchar for their constructive formal reviews.

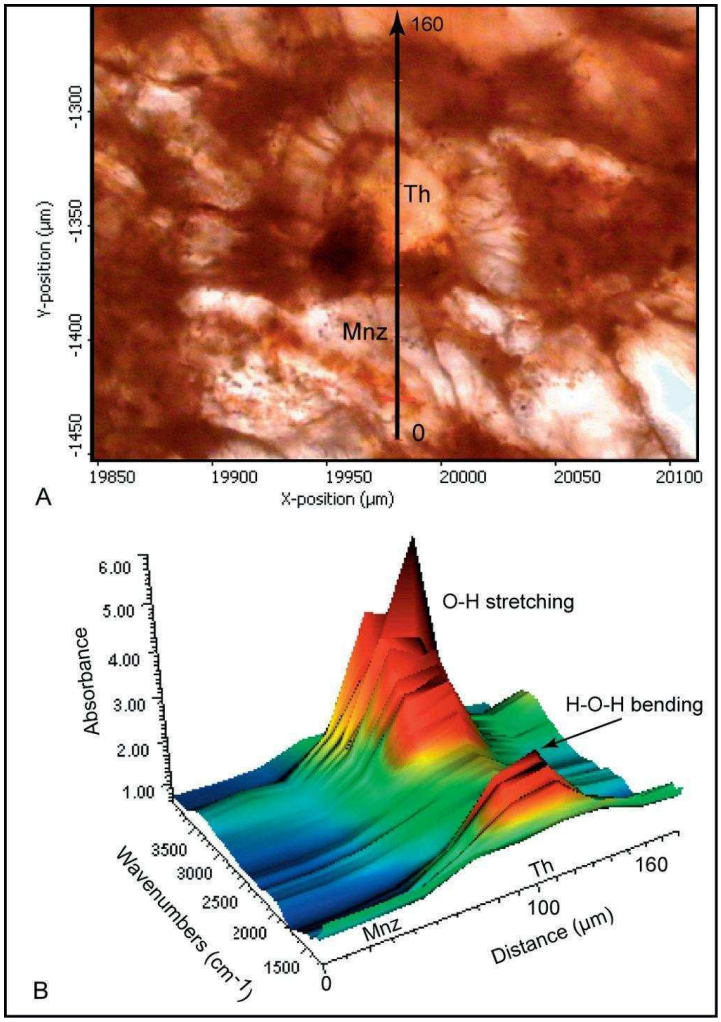

Fig. 4. (A) Transmission optical microscope image of a $ThSiO_4$ (Th) included in monazite (Mnz) and surrounded by concentric cracks and numerous red iron oxide inclusions filling the cracks. The vertical arrow locates the position of the FTIR profile composed of 9 analyses at a spacing of 20 µm. (B) FTIR profile through monazite and the $ThSiO_4$ inclusion showing the presence of molecular water within the $ThSiO_4$ inclusion: O-H stretching at 3600-2900 cm^{-1} and H-O-H bending at 1645 cm^{-1}.

References

Bingen, B., Skår, Ø., Marker, M., Sigmond, E.M.O., Nordgulen, Ø., Ragnhildstveit, J., Mansfeld, J., Tucker, R.D., Liégeois, J.-P. (2005): Timing of continental building in the Sveconorwegian orogen, SW Scandinavia. *Norweg. J. Geol.*, **85**, 87–116.

Black, L.P., Fitzgerald, J.D., Harley, S.L. (1984): Pb isotopic composition, colour, and microstructure of monazites from a polymetamorphic rock in Antarctica. *Contrib. Mineral. Petrol.*, **85**, 141–148.

Carrez, P., Demyk, K., Cordier, P., Gengembre, L., Grimblot, J., d'Hendecourt, L., Jones, A.P., Leroux, H. (2002a): Low-energy helium ion irradiation-induced amorphization and chemical changes in olivine: insights for silicate dust evolution in the interstellar medium. *Meteorit. Planet. Sci*, **37**, 1599–1614.

Carrez, P., Demyk, K., Leroux, H., Cordier, P., Jones, A.P., d'Hendecourt, L. (2002b): Low-temperature crystallization of $MgSiO_3$ glasses under electron irradiation: possible implications for silicate dust evolution in circumstellar environments. *Meteorit. Planet. Sci.*, **37**, 1615–1622.

Cherniak, D.J. (1993): Lead diffusion in titanite and preliminary results on the effect of radiation damage on Pb transport. *Chem. Geol.*, **110**, 177–194.

Davis, D.W. & Krogh, T.E. (2000): Preferential dissolution of ^{234}U and radiogenic Pb from α-recoil-damaged lattice sites in zircon: implications for thermal histories and Pb isotopic fractionation in the near surface environment. *Chem. Geol.*, **172**, 41–58.

Ewing R.C. (1975): The crystal chemistry of complex niobium and tantalum oxides IV. The metamict state: discussion. *Am. Mineral.*, **60**, 728–733.

Ewing, R.C. & Headley, T.J. (1983): Alpha-recoil damage in natural zirconolite ($CaZrTi_2O_7$). *J. Nucl. Mat.*, **119**, 102–109.

Ewing, R.C. & Wang, L.M. (2002): Phosphates as Nuclear Waste Forms. *Rev. Mineral. Geochem.,* Ribbe P.H., ed., Mineral. Soc. Amer., Washington DC., **48**, 673–699.

Ewing, R.C., Meldrum, A., Wang, L.M., Wang, S.X. (2000): Radiation-induced amorphisation. *Rev. Mineral. Geochem.,* Ribbe P.H., ed., Mineral. Soc. Amer., Washington DC., **39**, 319–361.

Ewing, R.C., Weber, W.J., Clinard, F.W. Jr. (1995): Radiation effects in nuclear waste forms. *Prog. Nucl. Energy*, **29**, 63–127.

Farges, F. & Calas, G. (1991): Structural analysis of radiation damage in zircon and thorite: an X-ray absorption spectroscopic study. *Am. Mineral.*, **76**, 60–73.

Förster, H.J. (1998): The chemical composition of REE-Y-Th-U-rich accessory minerals in peraluminous granites of the Erzgebirge-Fichtelgebirge region, Germany, Part I: The monazite-(Ce)-brabantite solid solution series. *Am. Mineral.*, **83**, 259–272.

Förster, H.J., Harlov, D.E., Milke, R. (2000): Composition and Th-U-Total ages of huttonite and thorite from Gillespie's beach, South Island, New Zealand. *Can. Mineral.*, **38**, 675–684.

Geisler, T., Pidgeon, R.T., van Bronswijk, W., Kurtz, R. (2002): Transport of uranium, thorium, and lead in metamict zircon under low-temperature hydrothermal conditions. *Chem. Geol.*, **191**, 141–154.

Geisler, T., Trachenko, K., Ríos, S., Dove, M.T., Salje, E.K.H. (2003): Impact of self-irradiation damage on the aqueous durability of zircon (ZrSiO4): Implications for its suitability as nuclear waste form. *J. Phys.: Condens. Matter*, **15**, 597–605.

Geisler, T., Seydoux-Guillaume, A.M., Wiedenbeck, M., Wirth, R., Berndt, J., Zhang, M., Mihailova, B., Putnis, A., Salje, E.K.H.,

Schlüter, J. (2004): Periodic precipitation pattern formation in hydrothermal treated metamict zircon. *Am. Mineral.*, **89**, 1341–1347.

Geisler, T., Seydoux-Guillaume, A.M., Poeml, P., Golla-Schindler, U., Berndt, J., Wirth, R., Pollok, K., Janssen, A., Putnis, A. (2005): Experimental hydrothermal alteration of crystalline and radiation-damaged pyrochlore. *J. Nucl. Mat.*, **344**, 17–23.

Gögen, K. & Wagner, G.A. (2000): Alpha-recoil track dating of quaternary volcanics. *Chem. Geol.*, **166**, 127–137.

Harrison, T.M., Catlos, E., Montel, J.M. (2002): U-Th-Pb dating of phosphate minerals. *Rev. Mineral. Geochem.,* Ribbe P.H., ed., Mineral. Soc. Amer., Washington D.C., **48**, 523–558.

Headley, T.J., Ewing, R.C., Haaker, R.F. (1981): Amorphous structure of metamict minerals observed by TEM. *Nature*, **293**, 449–450.

Holland, H. D. & Gottfried, D. (1955): The effect of nuclear radiation on the structure of zircon. *Acta Crystallogr.*, **8**, 291–300.

Johnson, P.B., Gilberd, P.W., Markwitz, A., Raudsepp, A., Brown, I.W.M. (2000): Helium ion implantation in SiAlON: characterization of cavity structures using TEM and IBA. *Nucl. Instrum. Methods Phys. Res. Sect.B.*, **166/167**, 121–127.

Lumpkin, G.R. & Chakoumakos, B.C. (1988): Chemistry and radiation effects of thorite-group minerals from the Harding pegmatite, Taos County, New Mexico. *Am. Mineral.,* **73**, 1405–1419.

Meldrum, A., Boatner, L.A., Weber, W.J., Ewing, R.C. (1998): Radiation damage in zircon and monazite. *Geochim. Cosmochim. Acta*, **62**, 2509–2520.

Meldrum, A., Boatner, L.A., Zinkle, S.J., Wang, S.X., Wang, L.M., Ewing, R.C. (1999): Effects of dose rate and temperature on the crystalline-to-metamict transformation in the ABO_4 orthosilicates. *Can. Mineral.,* **37**, 207–221.

Meldrum, A., Boatner, L.A., Ewing, R.C. (2000): A comparison of radiation effects in crystalline ABO_4-type phosphates and silicates. *Mineral. Mag.,* **64**, 183–192.

Montel, J.M., Foret, S., Veschambre, M., Nicollet, C., Provost, A. (1996): Electron microprobe dating of monazite. *Chem. Geol.*, **131**, 37–53.

Montel, J.M., Devidal, J.L., Avignant, D. (2002): X-ray diffraction study of brabantite-monazite solid solutions. *Chem. Geol.*, **191**, 89–104.

Murakami, T., Chakoumakos, B.C., Ewing, R.C., Lumpkin, G.R., Weber, W.J. (1991): Alpha-decay event damage in zircon. *Am. Mineral.*, **76**, 1510–1532.

Nasdala, L., Pidgeon, R.T., Wolf, D. (1996): Heterogeneous metamictization of zircon on a microscale. *Geochim. Cosmochim. Acta*, **60**, 1091–1097.

Nasdala, L., Wenzel, M., Andrut, M., Wirth, R., Blaum, P. (2001a): The nature of radiohaloes in biotite. *Amer. Mineral.*, **86**, 498–512.

Nasdala, L., Wenzel, M., Vavra, G., Irmer, G., Wenzel, T., Kober, B. (2001b): Metamictisation of natural zircon: Accumulation *versus* thermal annealing of radioactivity-induced damage. *Contrib. Mineral. Petrol.*, **141**, 125–144.

Oelkers, E.H. & Poitrasson, F. (2002): An experimental study of the dissolution stoichiometry and rates of a natural monazite as a function of temperature from 50 to 230°C and pH from 1.5 to 10. *Chem. Geol.*, **191**, 73–87.

Overwijk, M.H.F., van den Heuvel, F.C., Bulle-Lieuwma, C.W.T. (1993): Novel scheme for the preparation of transmission electron microscopy specimens with a focused ion beam. *J. Vac. Sci. Technol.,* **11**, 202.

Owen, M.R. (1988): Radiation-damage halos in quartz. *Geology*, **16**, 529–532.

Pabst, A. (1952): The metamict state. *Am. Mineral.*, **37**, 137–157.

Pabst, A. & Hutton, C.O. (1951): Huttonite a new monoclinic thorium silicate. *Am. Mineral.*, **36**, 60–69.

Poitrasson, F., Chenery, S., Bland, D.J. (1996): Contrasted monazite hydrothermal alteration mechanisms and their geochemical implications for the U-Th-Pb geochronology and nuclear ceramics. *Earth Planet. Sci. Lett.*, **145**, 79–96.

Poitrasson, F., Chenery, S., Shepherd, T.J. (2000): Electron microprobe and LA-ICP-MS study of monazite hydrothermal alteration: implications for the U-Th-Pb geochronology and nuclear ceramics. *Geochim. Cosmochim. Acta*, **64**, 3283–3297.

Poitrasson, F., Hanchar, J.M., Schaltegger, U. (2002): The current state and future of accessory mineral research. *Chem. Geol.*, **191**, 3–24.

Read, D. & Williams, C.T. (2001): Degradation of phosphatic waste forms incorporating long-lived radioactive isotopes. *Mineral. Mag.,* **65**, 589–601.

Roberts, S., McCaffrey, J., Giannuzzi, L., Stevie, F., Zaluzec, N. (2001): Advanced techniques in TEM specimen preparation, *in* Xiao-Feng Zhang & Ze Zhang, eds.,"Progress in transmission electron microscopy, Volume 1", *Springer Series in Surface Sciences*, **38**, 336–342.

Romer, R. (2003): Alpha-recoil in U-Pb geochronology: effective sample size matters. *Contrib. Mineral. Petrol.,* **145**, 481–491.

Salje, E.K.H. (2000): Structural transformations in minerals: The role of temperature and radiation damage. *Ber. Dtsch. Mineral. Ges., Beih. z. Eur. J. Mineral.*, **12**, 175.

Seydoux-Guillaume, A.M., Wirth, R., Heinrich, W., Montel, J.M. (2002a): Experimental determination of the Th partitioning between monazite and xenotime using Analytical Electron Microscopy and X-ray Diffraction Rietveld analysis. *Eur. J. Mineral.*, **14**, 869–878.

Seydoux-Guillaume, A.M., Wirth, R., Nasdala, L., Gottschalk, M., Montel, J.M., Heinrich, W. (2002b): An XRD, TEM and Raman study of experimentally annealed natural monazite. *Phys. Chem. Minerals*, **29**, 240–253.

Seydoux-Guillaume, A.M., Goncalves, P., Wirth, R., Deutsch, A. (2003): TEM study of polyphasic and discordant monazites: site specific specimen preparation using the Focused Ion Beam technique. *Geology*, **31**, 973–976.

Seydoux-Guillaume, A.M., Wirth, R., Deutsch, A. Schärer, U. (2004): Microstructure of 24 – 1928 Ma concordant monazites: implications for geochronology and nuclear waste deposits. *Geochim. Cosmochim. Acta*, **68**, 2517–2527.

Speer, J.A. (1982): Actinide orthosilicates. *Rev. Mineral. Geochem.,* Ribbe P.H. ,ed., Mineral. Soc. Amer., Washington DC., **5**, 113–135.

Taylor, M. & Ewing, R.C. (1978): The crystal structures of $ThSiO_4$ polymorphs: huttonite and thorite. *Acta Crystallogr. B*, **34**, 1074–1079.

Trachenko, K., Dove, M.T., Salje, E.K.H. (2000): Modelling the percolation-type transition in radiation damage. *J. Appl. Phys.*, **87**, 7702–7707.

Weber, W.J., Ewing, R.C., Catlow, C.R.A., Diaz de la Rubia, T., Hobbs, L.W., Kinishita, C., Matzke, H.J., Motta, A.T., Nastasi, M., Salje E.H.K., Vance E.R., Zinkle, S. J. (1998): Radiation effects in crystalline ceramics for the immobilization of high-level nuclear waste and plutonium. *J. Mater. Res.*, **13**, 1434–1484.

Wirth, R. (2004): Focused Ion Beam (FIB): A novel technology for advanced application of micro- and nanoanalysis in geosciences and applied mineralogy. *Eur. J. Mineral.*, **16**, 863–877.

Young, R.J. (1997): Application of the focused ion beam in materials characterization and failure analysis. *Microstr. Sci.*, **25**, 491–496.

Received 8 March 2006
Modified version received 5 September 2006
Accepted 13 November 2006

Chemical Geology (2009), **261**, 318–332.

Radiation damage in diopside and calcite crystals from uranothorianite inclusions

Anne-Magali Seydoux-Guillaume [a,*], Jean-Marc Montel [a], Richard Wirth [b], Bernard Moine [a]

[a] *LMTG, CNRS, Université de Toulouse, IRD, OMP, 14 avenue Edouard Belin, 31400 Toulouse, France*
[b] *GeoForschungsZentrum (GFZ) Potsdam-Division 4, Telegrafenberg, D-14473 Potsdam, Germany*

ARTICLE INFO

Article history:
Accepted 12 April 2008

Keywords:
Pleochroic halo
Radiation damage
Uranothorianite
Calcite
Diopside
FIB/TEM
Alteration

ABSTRACT

Combining observation and simulation, radiohalos formed around uranothorianite (UTh) from the Tranomaro granulitic skarns (SE-Madagascar) were studied. These structures consist of UTh grains surrounded by both aluminous diopside (Cpx) and calcite (Cc_1) crystals. Optical microscope and Scanning Electron Microscope (SEM) images revealed (1) the presence of radiating cracks around the UTh probably due to swelling of the metamict UTh, (2) a diffuse optical halo at the Cc_1/UTh interface, and (3) a wide "reaction zone" at the Cpx/UTh interface, composed of "secondary calcite" (Cc_2) with low temperature sheet silicate from the smectite (φ) group. Samples prepared across various interfaces using Focused Ion Beam (FIB) were investigated by Transmission Electron Microscope (TEM). In contrast to SEM observations, there is no direct contact between Cc_1 and UTh. From Cc_1 to UTh, we found: (1) a large (~200–300 nm) amorphous zone (A), enriched in U, Th and Ca, but without Si; (2) a chain (B) of very small (~20 nm) ThO_2 crystals; (3) another amorphous zone (C), which, in contrast to zone A is enriched in Si; and (4) another zone (D) made of small amorphous Si-rich "bubbles". The organization is similar for the UTh–Cc_2 interface. The presence of hydrous minerals (smectite) and carbonate (calcite) in reaction zone and in cracks, the presence of Pb-rich inclusions in secondary calcite, the abundance of fluid inclusions in the porous layer in calcite, the dissociation of U and Th in the calcite–uranothorianite layer, and the ThO_2 chains along interfaces, are strong indications that low-temperature crystallization was promoted by a fluid phase. SRIM simulation was used to calculate the effect of α and recoil particles of the three decay chains, in Cpx, Cc and UTh. The thickness of the damaged area calculated for α in Cpx and Cc are similar to the widths of the recrystallized areas observed in thin section (~30 μm). Corrected with the "wandering recoil effect", the size of the damaged area calculated for recoil nuclei in Cc (~50–60 nm) is ~multiplied by 3 and is in rather good agreement with the thickness of the totally amorphous layer at the Cc–UTh interface (~200 nm). Finally, it is emphasized that radiohalos are a point of chemical and physical weakness in a rock and probably a starting point for alteration.

Chemical Geology 261 (2009) 318–332

Contents lists available at ScienceDirect

Chemical Geology

journal homepage: www.elsevier.com/locate/chemgeo

Radiation damage in diopside and calcite crystals from uranothorianite inclusions

Anne-Magali Seydoux-Guillaume [a,*], Jean-Marc Montel [a], Richard Wirth [b], Bernard Moine [a]

[a] LMTG, CNRS, Université de Toulouse, IRD, OMP, 14 avenue Edouard Belin, 31400 Toulouse, France
[b] GeoForschungsZentrum (GFZ) Potsdam-Division 4, Telegrafenberg, D-14473 Potsdam, Germany

ARTICLE INFO

Article history:
Accepted 12 April 2008

Keywords:
Pleochroic halo
Radiation damage
Uranothorianite
Calcite
Diopside
FIB/TEM
Alteration

ABSTRACT

Combining observation and simulation, radiohalos formed around uranothorianite (UTh) from the Tranomaro granulitic skarns (SE-Madagascar) were studied. These structures consist of UTh grains surrounded by both aluminous diopside (Cpx) and calcite (Cc_1) crystals. Optical microscope and Scanning Electron Microscope (SEM) images revealed (1) the presence of radiating cracks around the UTh probably due to swelling of the metamict UTh, (2) a diffuse optical halo at the Cc_1/UTh interface, and (3) a wide "reaction zone" at the Cpx/UTh interface, composed of "secondary calcite" (Cc_2) with low temperature sheet silicate from the smectite (φ) group. Samples prepared across various interfaces using Focused Ion Beam (FIB) were investigated by Transmission Electron Microscope (TEM). In contrast to SEM observations, there is no direct contact between Cc_1 and UTh. From Cc_1 to UTh, we found: (1) a large (~200–300 nm) amorphous zone (A), enriched in U, Th and Ca, but without Si; (2) a chain (B) of very small (~20 nm) ThO_2 crystals; (3) another amorphous zone (C), which, in contrast to zone A is enriched in Si; and (4) another zone (D) made of small amorphous Si-rich "bubbles". The organization is similar for the UTh–Cc_2 interface. The presence of hydrous minerals (smectite) and carbonate (calcite) in reaction zone and in cracks, the presence of Pb-rich inclusions in secondary calcite, the abundance of fluid inclusions in the porous layer in calcite, the dissociation of U and Th in the calcite–uranothorianite layer, and the ThO_2 chains along interfaces, are strong indications that low-temperature crystallization was promoted by a fluid phase. SRIM simulation was used to calculate the effect of α and recoil particles of the three decay chains, in Cpx, Cc and UTh. The thickness of the damaged area calculated for α in Cpx and Cc are similar to the widths of the recrystallized areas observed in thin section (~30 μm). Corrected with the "wandering recoil effect", the size of the damaged area calculated for recoil nuclei in Cc (~50–60 nm) is ~multiplied by 3 and is in rather good agreement with the thickness of the totally amorphous layer at the Cc–UTh interface (~200 nm). Finally, it is emphasized that radiohalos are a point of chemical and physical weakness in a rock and probably a starting point for alteration.

1. Introduction

During geological time, U- and Th-rich minerals accumulate radiation damage, mainly from α decay. Such damage destroys to a variable extent the host crystal network, leading to an amorphous structure, called metamict state (summary in Ewing, 1994). Damage is caused by three types of particles. First, α particles, which are energetic (4–8 MeV), penetrative, (10–20 μm), but not very destructive (about 100 displacement/particle); second, recoil nuclei (daughter nuclei), which are less energetic (100–400 keV), less penetrative (20–50 nm), but more destructive (800–2000 displacement/particle); finally, fission nuclei, which are very energetic (150–200 MeV), very destructive (fission tracks are 10–20 μm long and 5–10 nm diameter, and made of several ten thousands displacements), but very rare (0.0005% of ^{238}U decays). Submitted to natural radiation damages, i.e. accumulated over a long time, minerals react differently: many minerals, like zircon (review in Ewing et al., 2003) or allanite (Headley et al., 1981; Janeczek and Eby, 1993), become amorphous (metamict), whereas some remain crystalline such as monazite (Meldrum et al., 1998; Ewing and Wang, 2002; Seydoux-Guillaume et al., 2002; 2004; reviews in Ewing et al., 2003) or apatite (Linberg and Ingram, 1964; review in Ewing and Wang, 2002).

Radiation damage in radioactive minerals has been studied in the geosciences for two main reasons. First, U–Th-rich minerals are used for U–Th–Pb dating, and it is essential to understand the effects of radiation damages on lead retentivity (Lumpkin et al., 1986a; Davis and Krogh, 2000; Romer, 2003). Second, the effect of long-term accumulation of radiation damage is a key parameter for assessing the durability of ceramics that could be used as nuclear-waste forms (Ewing, 1975; Ewing et al., 1988; Ewing et al., 1995; Weber et al., 1998).

Four strategies are used to study radioactive damage in minerals (see review in Ewing et al., 2000): (1) external irradiation by ion beams (e.g. Wang and Ewing, 1992; Meldrum et al., 1998); (2) atomistic simulations (e.g. Crocombette and Ghaleb, 2001; Trachenko et al., 2001); (3) synthesis of doped-crystal with short-lived isotopes (e.g. Begg et al.,

* Corresponding author. Tel.: +33 5 61 33 25 97.
E-mail address: seydoux@lmtg.obs-mip.fr (A.-M. Seydoux-Guillaume).

0009-2541/$ – see front matter © 2008 Elsevier B.V. All rights reserved.
doi:10.1016/j.chemgeo.2008.04.013

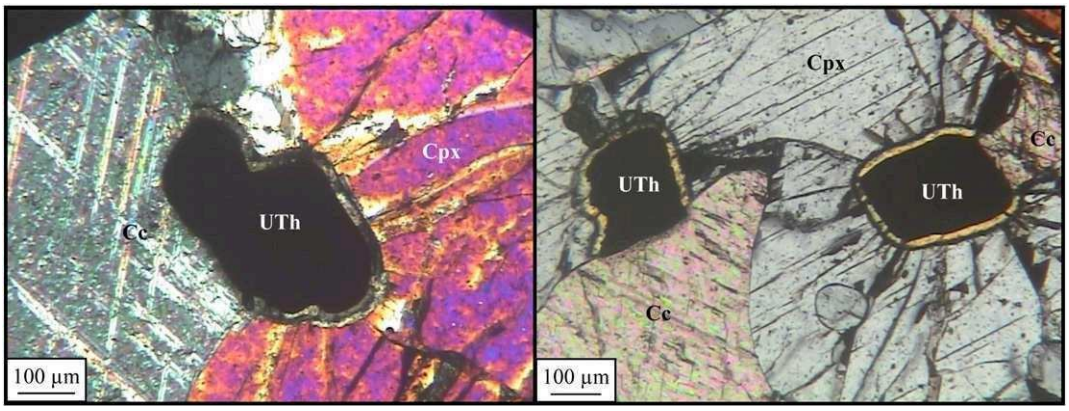

Fig. 1. Optical microscope images showing 3 uranothorianite (UTh) grains included in diopside (Cpx) + calcite (Cc) under crossed polar light. Note the associated structures due to irradiation from α decay of U and Th: (1) cracks, visible only in diopside, radiating from uranothorianite; (2) a diffuse optical halo at calcite–uranothorianite interface; and (3) a wide (~20–30 µm) "reaction zone" along diopside–uranothorianite interface.

2000; Burakov et al., 2002); (4) study of old naturally radioactive minerals in various geological contexts by using various analytical methods like IR (Zhang and Salje, 2001), EXAFS (Farges and Calas, 1991; Harfouche et al., 2005), Raman (Nasdala et al., 1995), RMN (Farnan et al., 2003), RPE (Balan et al., 2005), and TEM (Black et al., 1984; Lumpkin et al., 1986a; Murakami et al., 1991; Weber et al., 1994). The most studied minerals are those that are either used for U–Th–Pb geochronology or expected to be good candidate for nuclear-waste storage, and many papers have been published on zircon (review in Ewing et al., 2003), monazite (review in Ewing and Wang, 2002; Seydoux-Guillaume et al., 2004), titanite (Vance and Metson, 1985; Hawthorne et al., 1991; Lumpkin et al., 1991; Farges, 1997, Zhang et al., 2002), pyrochlore and zirconolite (Lumpkin et al., 1986b; Lumpkin and Ewing, 1988; Farges et al., 1993; Farges, 1997), apatite (Ouchani et al. 1997), and thorite-group (Lumpkin and Chakoumakos, 1988; Farges and Calas, 1991).

However, radioactive minerals not only irradiate themselves, but also the surrounding non-radioactive minerals. This produces concentric structures called "pleochroic halos" or "radiohalos", very familiar to petrologists, who use them to identify radioactive minerals in metamorphic or plutonic rocks. In contrast to the numerous studies dealing with radiation effects in radioactive minerals themselves, the effect of radiation damages in host minerals are rare. The first time that such halo around mineral inclusions was interpreted as being due to the radioactivity of these inclusions was 100 years ago (Mügge, 1907; Joly, 1907). After that, studies on radiohalos were published between the seventies and the nineties (e.g. Gentry, 1973, 1974; Owen, 1988; Odom and Rink, 1989; Meunier et al., 1990). Recently, only two papers deal with radiohalos: in biotite (Nasdala et al., 2001) and in chlorite and cordierite (Nasdala et al., 2006). These latter studies demonstrated that radiohalos are created by α particles and correspond only to modification of optical characteristics of the host mineral, the various energies of the α particles explaining the difference in size of the halos. Furthermore, those authors found intensive damage (i.e. amorphous domains visible via TEM) only in cordierite up to a few tens of nanometers away from radioactive inclusions. They interpreted these damaged zones to recoil nuclei. Such amorphous zones at the vicinity of a radioactive mineral has already been observed by using Focused Ion Beam–Transmission Electron Microcopy (FIB–TEM) across monazite–quartz boundaries by Seydoux-Guillaume et al. (2003); in this case, the zone was ~150 nm wide.

However, other consequences of radiation damage have not been evaluated. In rocks, poorly crystallized areas, such as the metamict grains but also the damaged zone around them, are actually zones, which can be used by geological fluids to initiate alteration. Another important effect is swelling produced by radiation damage, which can induce cracks around the enclosing minerals, forming pathways for fluids to penetrate into the rock.

The aim of this study is to investigate, by various electron microscopy techniques, the effect of irradiation in a radioactive mineral (uranothorianite) and in the surrounding minerals (calcite and diopside). The geological consequences of radioactive damage for the non-radioactive host minerals and for the whole-rock itself will be discussed.

2. Sample description

The studied sample (SB540) is a diopside-bearing marble within skarns from the Tranomaro area (Andranomitrohy open pit at 46°33.15′ E, 24°19.97′ S) in South-East Madagascar, metamorphosed under granulitic

Table 1
Compositions (in wt.%) of uranothorianite (UTh), diopside (Cpx), calcite (Cc) and sheet silicate (φ) from Fig. 2A obtained by EMP.

# (Fig. 2A)	Uranothorianite (UTh)					Sheet silicate (φ)				Diopside (Cpx)				Calcite (Cc)
	1	2	12	13	14	3	4	5	6	7	8	9	10	11
Na_2O	0.00	0.00	0.08	0.00	0.00	0.07	0.00	0.00	0.00	0.12	0.22	0.21	0.29	0.00
MgO	0.00	0.00	0.00	0.01	0.00	10.56	14.02	15.50	13.75	13.79	13.72	14.05	13.99	0.66
Al_2O_3	0.00	0.00	0.00	0.00	0.00	19.05	18.42	18.75	19.06	8.22	8.19	8.38	8.35	0.00
SiO_2	0.00	0.39	0.00	0.01	0.00	43.58	39.52	33.68	43.81	48.73	48.70	49.27	48.67	0.04
K_2O	0.10	0.03	0.05	0.04	0.11	0.21	0.10	0.03	0.20	0.00	0.02	0.00	0.00	0.00
CaO	0.19	0.25	0.16	0.11	0.16	2.26	1.87	1.94	2.34	25.03	25.38	25.00	25.07	55.95
TiO_2	0.00	0.00	0.00	0.00	0.00	0.25	0.18	0.09	0.24	0.74	0.72	0.83	0.68	0.00
Cr_2O_3	0.04	0.00	0.07	0.00	0.01	0.00	0.04	0.02	0.00	0.00	0.00	0.00	0.02	0.02
MnO	0.00	0.07	0.07	0.05	0.02	0.13	0.01	0.23	0.10	0.11	0.05	0.00	0.04	0.02
FeO	0.12	0.00	0.00	0.01	0.01	6.28	7.55	14.45	7.25	2.36	2.26	2.23	2.50	0.19
PbO	3.77	3.74	4.10	4.33	3.92	0.06	0.17	0.14	0.00	0.25	0.00	0.00	0.05	0.18
ThO_2	66.37	64.80	66.33	66.12	66.99	0.04	0.68	0.10	0.00	0.03	0.00	0.06	0.08	0.00
UO_2	29.24	28.50	30.27	29.76	28.92	0.10	0.00	0.00	0.00	0.00	0.06	0.00	0.01	0.00
Total	99.83	97.78	101.14	100.44	100.15	82.57	82.56	84.93	86.75	99.38	99.31	100.03	99.75	57.06

EMP operating at 15 kV, 20 nA. Standards are: albite (NaKα), periclase (MgKα), corundum (AlKα), wollastonite (Si and CaKα), sanidine (KKα), perovskite (Ti and MnKα), Cr_2O_3 (CrKα), hematite (FeKα), synthetic Pb-glass (PbMβ), synthetic ThO_2-ceramic (ThMα) and synthetic UO_2-ceramic (UMβ).

conditions (4–5 kbar, 800–850 °C; Rakotondrazafy, 1995; Rakotondrazafy et al., 1996) during the Pan-African orogeny (565–580 Ma, Paquette et al., 1994). In this region, at the western border of the Anosyan Belt, uranothorianite mineralization is common (Moine et al., 1985; Boulvais et al., 1998; Ramambazafy, 1998; Ramambazafy et al., 1998; Boulvais et al., 2000). They occur in skarns formed by metasomatic alteration of calcitic marbles (Moine et al., 1985). Fluid inclusions study shows that fluids are CO_2-rich ($X_{CO2} \geq 0.8$) and in equilibrium with mineral assemblages (Ramambazafy et al., 1998). The hydrothermal/metasomatic mobility of Th can be explained by transport in F-rich fluids as shown by the widespread occurrence of fluor-phlogopite and fluor-pargasite (Moine et al., 1998; Ramambazafy, 1998).

Minerals are essentially aluminous diopside (Cpx) and calcite (Cc_1) sometimes containing uranothorianite inclusions; but spinel, pargasite, plagioclase, phlogopite and zirconolite may also be present. Optical microscope pictures (Fig. 1) show examples of 3 uranothorianite grains included in diopside + calcite. The uranothorianite grains are systematically associated with structures suggesting that radioactivity significantly modified the host non-radioactive minerals. These include: (1) cracks, visible only in diopside, radiating from uranothorianite; (2) a

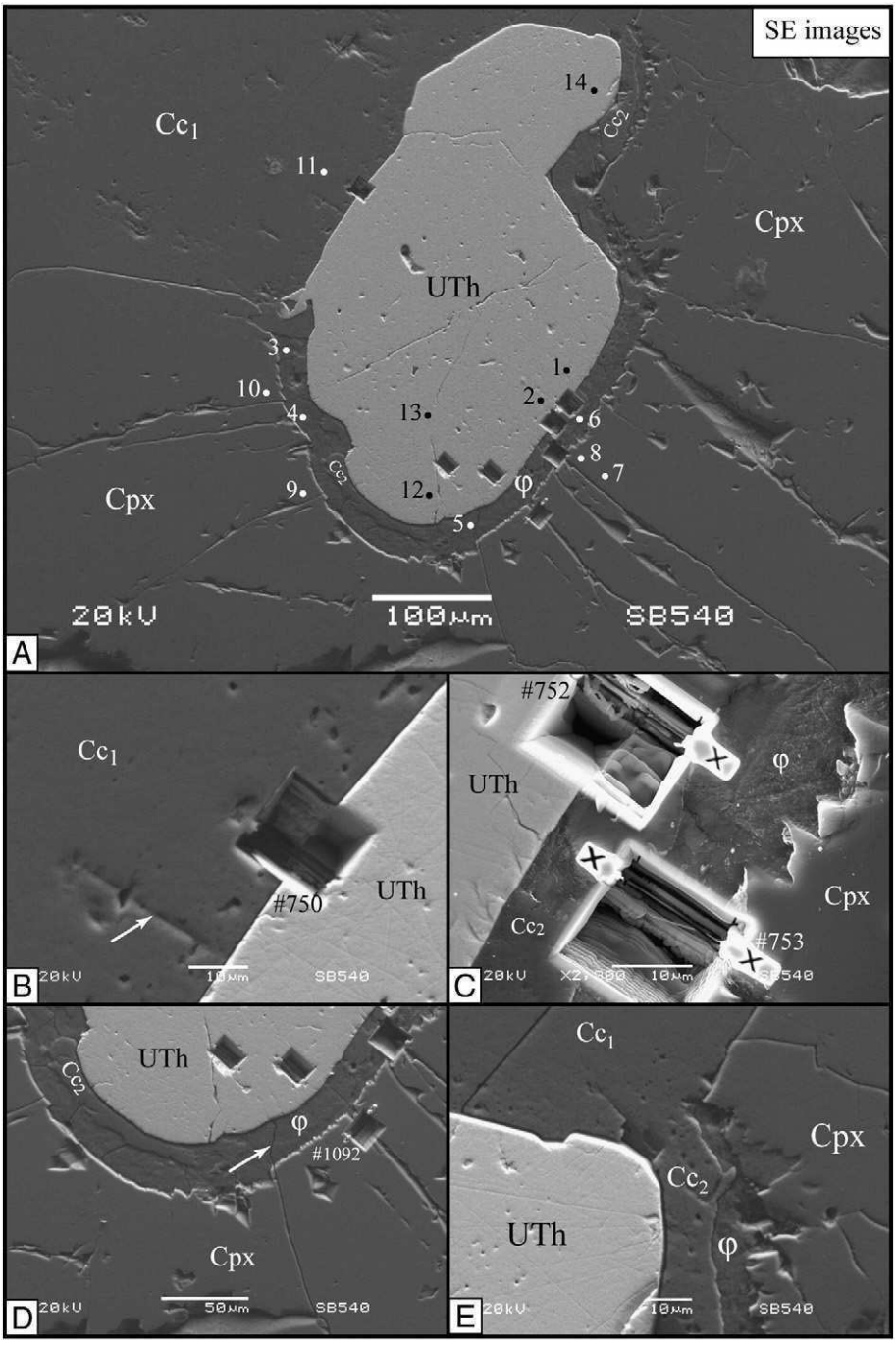

Fig. 2. Scanning Electron Microscope (SEM) images in Secondary Electron (SE) mode from UTh + Cc_1 + Cpx shown in Fig. 1 (left one). A. Note the associated structures due to irradiation from α decay of U and Th: (1) cracks, visible only in diopside, radiating from uranothorianite; (2) a diffuse optical halo at calcite–uranothorianite interface; and (3) a wide (~20–30 µm) "reaction zone" along the diopside–uranothorianite interface. Within this reaction zone, 2 other phases were observed: a secondary calcite (Cc_2) and a clay mineral (φ). 7 FIB holes and Electron Microprobe analyses (see numbers) were also done. B. FIB hole across UTh–Cc_1 boundary (# 750). Note the porosity within Cc_1 and possible remnant of cracks (see arrow). C. Enlargement within the "reaction zone" showing mixture of a secondary calcite (Cc_2) and a low-T clay mineral (φ), and FIB holes done across UTh-φ (# 752) and φ-Cpx (# 753) boundaries. D. Enlargement within the "reaction zone" showing fractures within diopside, with some extended into the reaction zone (arrow), and FIB hole cut across one crack (# 1092). E. Enlargement within the "reaction zone" showing high porosity within Cc_2.

diffuse optical halo at the calcite–uranothorianite interface; and (3), a wide (~20–30 μm) "reaction zone" along the diopside–uranothorianite interface. Only diopside in contact with uranothorianite show these corona; other diopside crystals are pristine indicating these features are due to irradiation coming from α decay of U and Th.

3. Analytical methods

3.1. Scanning Electron Microscope (SEM) and Electron Microprobe (EMP)

SEM images and EDX mapping were performed using the JEOL 6360 equipped with a Sahara detector from PGT at the LMTG-Toulouse. Quantitative EMP analyses were obtained using the Cameca SX50 at the LMTG-Toulouse operating at 15 kV and 20 nA (Table 1).

3.2. Transmission Electron Microscope (TEM) coupled with Focused Ion Beam (FIB) technique

Since the aim of this study is to investigate the interfaces between grains in thin section, a site-specific preparation method for TEM analysis is needed. This method is called Focused Ion Beam (FIB) and allows cutting site-specific TEM foils, ~15–20 μm by 10–15 μm, and ~100 nm thick (for technical details, see, Overwijk et al., 1993; Young, 1997; Roberts et al, 2001 and Wirth, 2004). TEM samples were milled

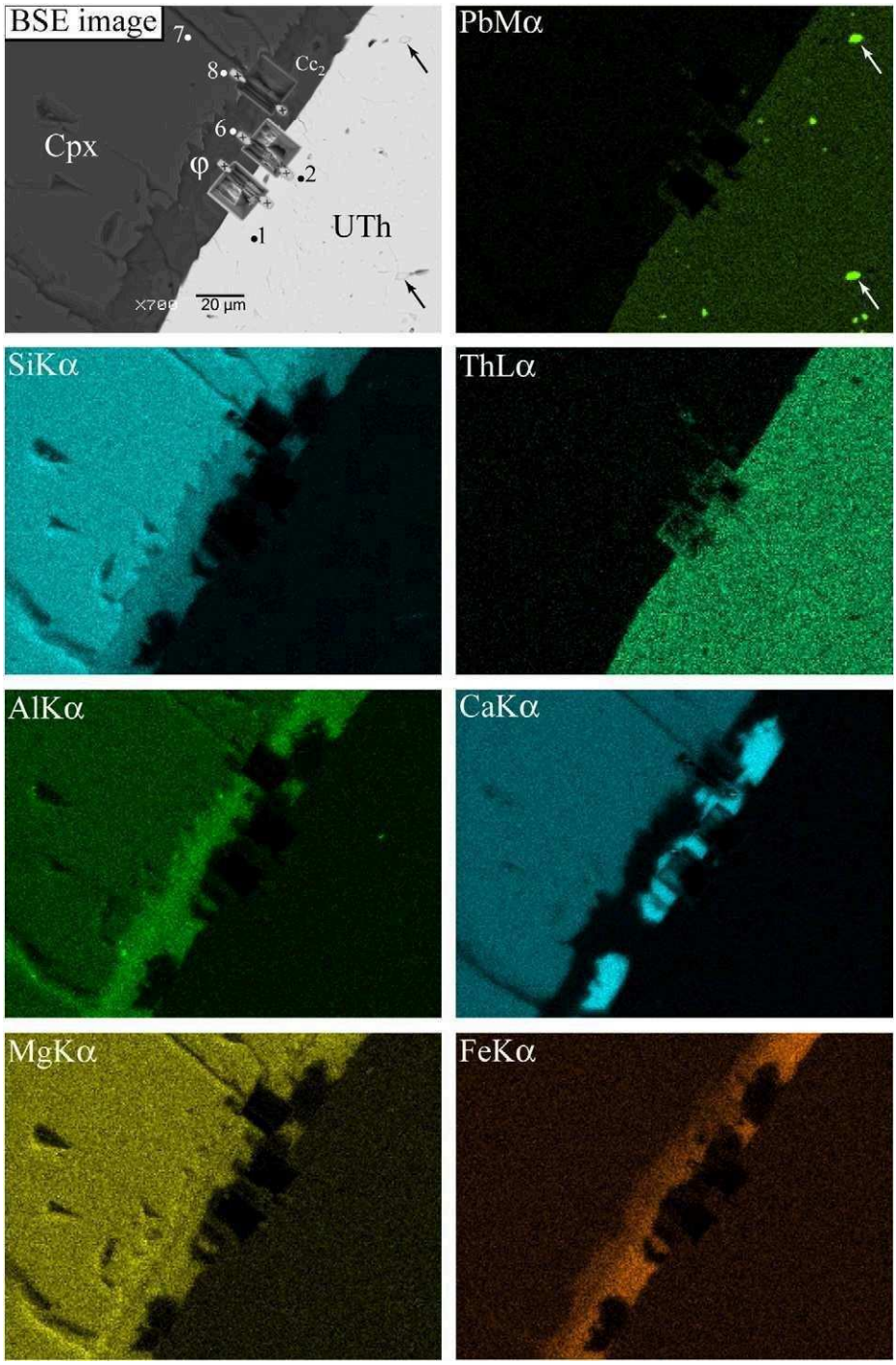

Fig. 3. SEM chemical maps of PbMα, SiKα, ThLα, AlKα, CaKα, MgKα and FeKα of the zone observed in the Back Scattered Electron (BSE) image on the left. Acquisition time was 12.4 sec/image for a total of 140 images and a size of maps of 256×192×16 bits. Note of the high quantity of PbS inclusions within UTh.

by using gallium ions accelerated to 30 keV. The TEM foil is cut perpendicular to the surface of the sample (Fig. 2), providing information with respect to the depth of the specimen. The site-specific specimens were prepared with the FEI FIB200 instrument at the GeoForschungsZentrum (GFZ)-Potsdam.

TEM studies were carried out with the Philips CM200 TEM, operating at 200 keV, equipped with an energy-dispersive X-ray analyzer (EDX) with an ultra-thin window, and a LaB_6 filament as electron source, and the FEI Tecnai™G^2 F20 X-Twin, operating at 200 kV, equipped with a FEG electron source, a high angle annular dark field (HAADF) detector, and an EDAX energy-dispersive X-ray analyzer system; both instruments are installed at the GFZ-Potsdam. Additional selected area diffraction (SAED) patterns were also performed at the TEMSCAN-Toulouse with a Jeol 2010 (200 keV, LaB_6) microscope.

4. Results

4.1. Microscopic study

In agreement with previous studies (Rakotondratsima, 1983; Ramambazafy, 1998), EMP analyses showed that uranothorianite is a solid-solution made of about two-thirds thorianite and third uraninite. The lead content is about 3–4 wt.% PbO. The SEM–EDX map (Fig. 3) shows that uranothorianite contains many Pb-rich inclusions, demonstrated by EMP and TEM to be galena PbS. The chemical ages calculated from U, Th, and Pb content range from 544 to 578 Ma, for four analyses, in agreement with the accepted ages for those rocks, but one analysis gives 931 Ma, due to high Pb content. We think that this analysis was contaminated by a galena inclusion, giving an apparently high Pb content, and then an apparently old age. Clinopyroxene is an Al-rich diopside ($X_{mg} = 0.92$, and 8.3 wt.% Al_2O_3).

The "reaction zone" at diopside–uranothorianite interface (Fig. 2C) consists of a mixture of calcite (secondary calcite, Cc_2), with an Al–Mg–Fe–silicate fibrous phase (φ) (Fig. 2C, D and E). EMP coupled with TEM results (Table 1) demonstrated that it is a low-T phyllosilicate from the smectite group. Secondary calcite is usually located at the inner part of the reaction zone, along uranothorianite, and is always porous, whereas smectite (φ) is located in the outer part along diopside. The diopside-reaction zone grain boundary is locally indented (Fig. 2A, C and D), along the main cleavage direction. The primary calcite–uranothorianite interface is sharp, but calcite in contact with uranothorianite is more or less porous on a ~20 μm layer (Fig. 2B and E), as is secondary calcite in the reaction zone (Fig. 2E).

SEM confirms the presence of cracks radiating around the uranothorianite within clinopyroxene (Fig. 2A and D). Possible remnants of cracks were observed within Cc_1 (arrow Fig. 2B). Some fractures extend into the reaction zone (Fig. 2A and D).

4.2. Nanometric study (FIB/TEM)

TEM samples were prepared using the FIB milling technique across the uranothorianite–primary calcite (#750; Fig. 2B), uranothorianite–secondary calcite (#752) and diopside-reaction zone (#753) interfaces (Fig. 2C); one foil was also cut across a fracture (#1092, Fig. 2D). From selected area diffraction (SAD) patterns (Fig. 4B and C), we can conclude that both primary calcite and uranothorianite are crystalline. The only indication of structural modification in those phases, is mottled diffraction contrast in bright field and dark field images, observed mostly in uranothorianite. In this mineral, diffraction spots are split (Fig. 4C), probably because of PbS inclusions (Fig. 3—PbMα map).

Uranothorianite–primary calcite interface (Figs. 4 and 5): in contrast to what was observed with SEM, there is no direct contact between primary calcite and uranothorianite. Four different zones (A, B, C and D) were identified (Fig. 5). From calcite to uranothorianite, we found: (1) a large (~200–300 nm) amorphous zone (A), enriched in U and Th, but without Si (see U–Th–Si maps in Fig. 5) and enriched in Ca (see EDX spectrum Fig. 5); (2) a chain (B) of very small (~20 nm) ThO_2 crystals free of U (Figs. 4 and 5); (3) another amorphous zone (C), which, in contrast to zone A is enriched in Si; and (4) another zone (D) made of small amorphous Si-rich "bubbles". Many fluid inclusions were observed in the calcite, some of them displaying a "negative crystal" shape (arrow Fig. 4A).
Diopside-reaction zone interface (Fig. 6): the FIB cut foil shows preferential dissolution of Cpx along cleavages, giving this particular triangular-shaped boundary (Fig. 6A). Within the

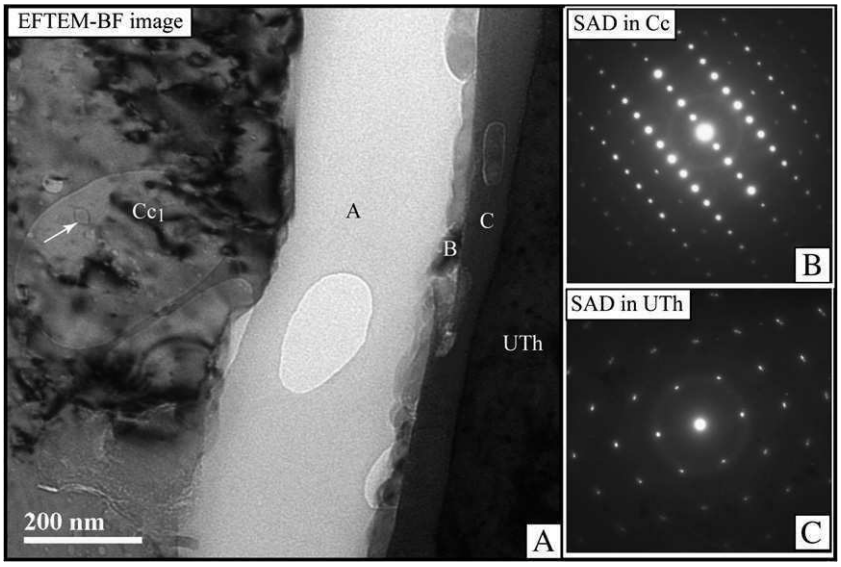

Fig. 4. TEM foil # 750. A. Energy Filtered Transmission Electron Microscope (EFTEM) — Bright Field (BF) image showing presence of an amorphous zone (A) between primary calcite (Cc_1) and UTh. Zone (B) correspond to ThO_2 grains and zone (C) to another amorphous zone (see Fig. 5). Many fluid inclusions were observed in the calcite, some of them displaying a "negative crystal" shape (see arrow). B and C. Selected area diffraction (SAD) patterns in respectively primary calcite and UTh showing that both phases are crystalline. In UTh diffraction spots are split probably because of the presence of PbS inclusions within UTh (arrows in Fig. 3).

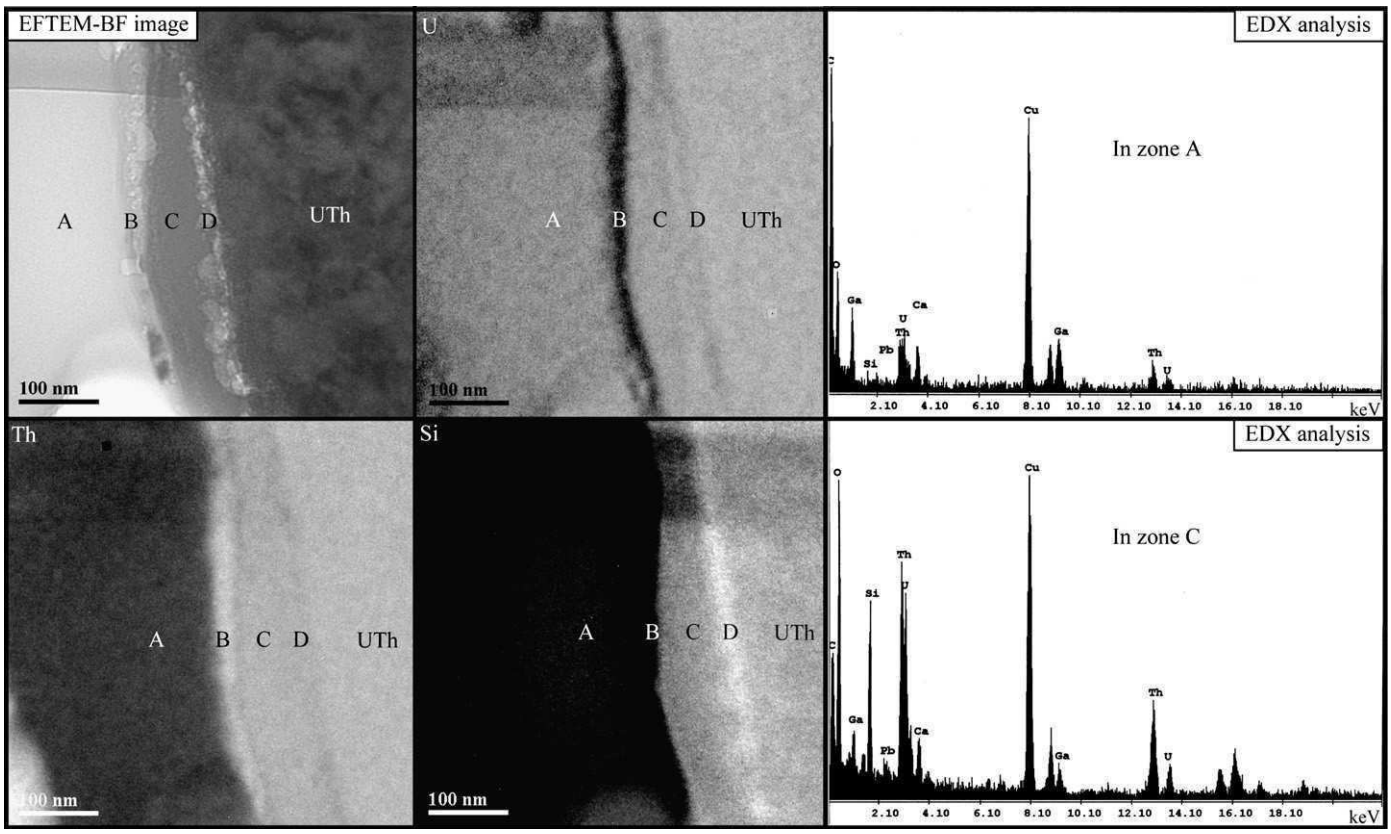

Fig. 5. TEM foil # 750. EFTEM-BF image (on the top on the left), and U, Th, Si-jump ratio maps of the same zone showing from calcite to uranothorianite: (1) a large (~200–300 nm) amorphous zone (A), enriched in U and Th, but without Si (see U, Th and Si maps) and enriched in Ca (see EDX spectrum on the right); (2) a chain (B) of very small (~20 nm) ThO_2 crystals free of U; (3) another amorphous zone (C), which, in contrast to zone A is enriched in Si (see EDX spectrum on the right and Si-map); and (4) another zone (D) made of small amorphous Si-rich "bubbles".

reaction zone an unoriented clay mineral (smectite) was observed, with its typical layer-form (Fig. 6B and C). Many inclusions are present in this zone (arrows on Fig. 6): Pb-rich inclusions as well as and U + Th-rich inclusions.

Uranothorianite–secondary calcite interface (Fig. 7): the organization is similar, but opposite to the uranothorianite–primary calcite interface. An amorphous zone (A) enriched in U, Th and Ca and a chain of ThO_2 crystals (B) parallel to the interface was observed. However the ThO_2 layer is mostly along calcite, and not along uranothorianite, and no Si-rich zone was observed. Secondary calcite contains many fluid inclusions (see arrows in Fig. 7A and C) and U + Th + Pb-rich inclusions (large inclusion Fig. 7A).

Within one crack (Fig. 8): the fracture (~2 μm wide) is filled with a mixture of clay mineral and calcite similar to the reaction zone. It contains also ZrTiCaTh-amorphous phase (Zr), presumably metamict zirconolite, already described in those rocks (Rakotondrazafy et al., 1996). Nano-channels are visible at the interface between diopside and the crack border; the channel is larger (~70 nm compared to ~40 nm) on the upper side (Fig. 8A and B). Bright field (BF) image of the upper channel (Fig. 8B) shows that it is filled with nano-bubbles, i.e. fluid inclusions.

4.3. Summary of petrographic features

The aureole along the diopside–uranothorianite interface is not a pleochroic halo such as described by Nasdala et al. (2001) in biotite or Nasdala et al. (2006) in cordierite. It is a totally transformed zone, filled with material that we could expect to form during low-temperature retrogression of diopside. The transformed zone is rather constant in thickness: 20 to 38 μm, with an average at 27 μm. The transition to pristine diopside is very sharp, but sometime indented. The transformations in primary calcite are less visible but there is actually a porous calcite layer, again 20 to 30 μm thick, although it is there more difficult to estimate. At the nano-scale, the uranothorianite–calcite interfaces are quite complex, with several layers, of various chemical compositions and structural states.

Those observations suggest that primary calcite and diopside located close to uranothorianite has been crystallized at low temperature, as a secondary porous calcite for calcite, and as a mixture of secondary calcite and clay mineral for diopside. The presence of hydrous minerals (smectite) and carbonate (calcite) in reaction zone and in cracks, the presence of Pb-rich inclusions in secondary calcite, the abundance of fluid inclusions in the porous layer in primary calcite, the dissociation of U and Th in the calcite–uranothorianite layer, and the ThO_2 chains along interfaces, are all strong indications that low-temperature crystallization was promoted by a fluid phase.

Surprisingly, truly metamict material is very rare, limited to a narrow (200–300 nm) amorphous layer, along the calcite–uranothorianite interface. However all structures described above are strictly limited to the interface between uranothorianite and other minerals, so must be more or less related to the effect of irradiation. In order to evaluate how irradiation by U and Th could affect the minerals studied above, we carried out a detailed study of irradiation damages using the SRIM/TRIM software.

5. Modeling with SRIM/TRIM

Damage was modeled by using the SRIM/TRIM software package (Ziegler, 2006) which allows simulating the effect a particle in a target, knowing what kind of particle it is, its energy, and the density and chemical compositions of the target. It is based on full-quantum calculations of individual interactions of incident particles with the atoms of the target. For our purpose the interesting outputs are the particle path (in three dimensions), and the vacancies created in the

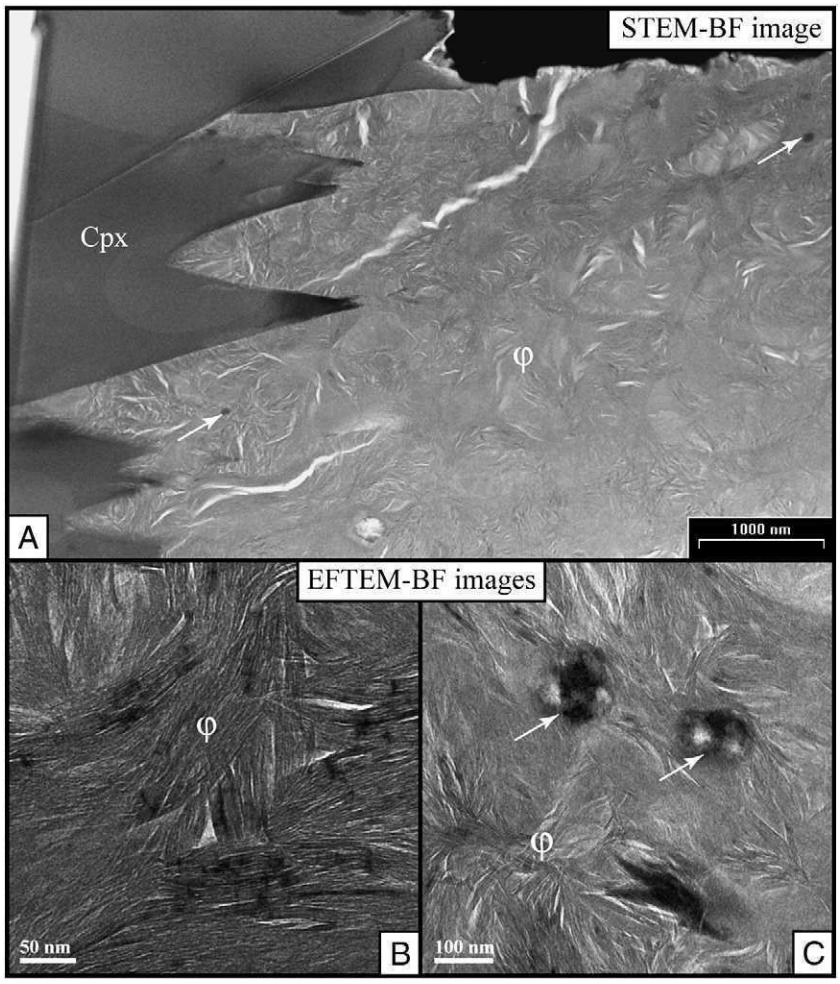

Fig. 6. TEM foil # 753. Scanning Transmission Electron Microscope Bright Field (STEM-BF) image (A) and EFTEM-BF images (B and C) showing preferential dissolution of diopside (Cpx) along cleavages, giving this particular triangular-shaped boundary, an unoriented clay mineral (φ-smectite), with its typical layer-form (B and C), and many Pb-rich as well as U + Th-rich inclusions (arrows in A and C).

target. SRIM/TRIM always assumes that the target is amorphous and isotropic.

5.1. Irradiation by U and Th chains

Irradiation by U and Th is done by all the radioelements of the ^{235}U, ^{238}U, and ^{232}Th decay chains which combine α and β decays to reach the final stable nuclei: ^{207}Pb, ^{206}Pb and ^{208}Pb respectively. We will neglect the β decay which produces no major damage, and we will neglect also α decays of minor branched radioactivity. During α decay, two particles are created: the α particle itself, which is a ^{4}He nucleus, and the recoil nucleus, which is actually the nucleus of the daughter element, belonging to elements from U to Tl. The total energy involved during an α decay is few MeV, distributed unevenly between the two particles (about 100 keV for the recoil, and the rest for the α). Then each α decay produces a slow, heavy nucleus (recoil), and a light, fast particle (α). Another source of damage in radioactive minerals is the spontaneous fission of ^{238}U. It is a rare event (0.00005% of the ^{238}U decay) but the energy involved is about 200 MeV, and it produces two fissions nuclei with atomic number around 100 and 140 respectively. The energies of the particles of the three decay chains are summarized in Table 2. For α particles, it ranges from 4 to 8.8 MeV and for recoil for from 70 to 170 keV.

Using SRIM we calculated the effect of α and recoil particles of the three decay chains, in diopside, calcite and uranothorianite, as well as the effect of two typical fission products ^{90}Y and ^{140}Ce. Usually 1000 particles are calculated to obtain good statistics. Two key outputs are presented in Table 2: the average distance reached by the particle, and the number of vacancies created. To illustrate the effect of α and recoil particles in minerals, the vacancy distributions for the ^{214}Po⇒^{210}Pb decay in diopside (α:7.69 MeV; recoil:146 keV), are presented in Fig. 9. For other decays or other minerals, the amount of vacancies and the distances are different, but the shapes are similar. The effects of α particles and recoil nuclei are fundamentally different. The α particles are penetratives (12–38 μm in diopside, 14 to 45 μm in calcite) and produce 220 to 270 vacancies in diopside and 170–200 vacancies in calcite. The recoil nuclei are 1000 times less penetrative (27–45 nm in diopside, 32–55 nm in calcite) but 10 times more destructive (1200–2500 vacancies in diopside, 940–2030 vacancies in calcite). The fast α particle produces vacancies only at the end of its displacement, when it has been slowed down enough by ionization to interact with target nuclei. The slow recoil nucleus creates vacancies all along its trajectory. In three dimensions, the trajectory of a series of α particles has the shape of a cone, while it is pear-shaped for the recoils. The maximum distance reached by an α particle is very close to the average distance, whereas it is about twice as long for recoil nuclei. Fundamentally the length of the trajectory increases with increasing energy, and decreases with increasing density of the target. In uranothorianite the length of the trajectories are about 9 to 30 μm for α particles, so only the outer part of the uranothorianite irradiates the surrounding minerals.

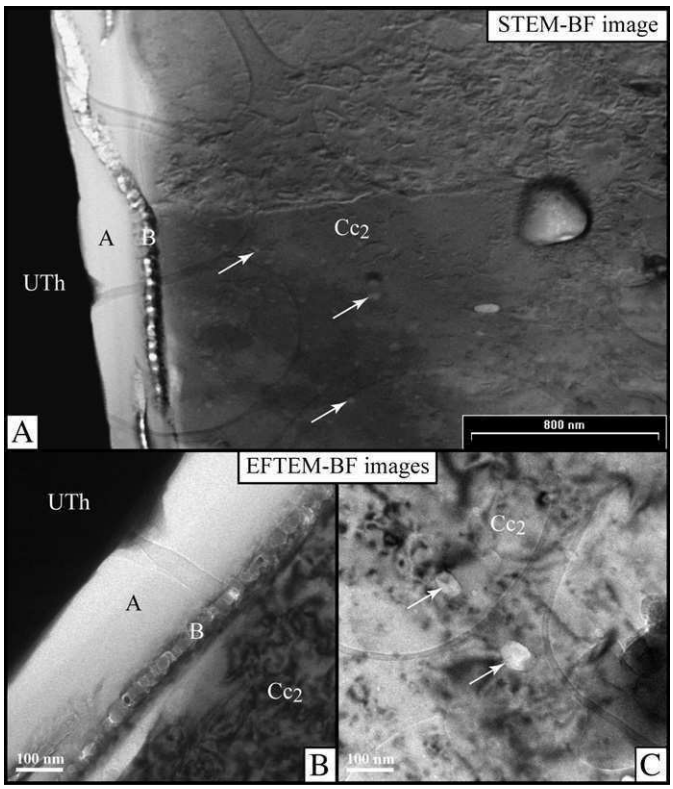

Fig. 7. TEM foil # 752. STEM-BF image (A) and EFTEM-BF images (B and C) showing a similar organization but reversed from the uranothorianite–Cc_1 interface: an amorphous zone (A) enriched in U, Th and Ca and a chain of ThO_2 crystals (B) parallel to the interface (see also image B). Secondary calcite (Cc_2) contains many fluid inclusions (see arrows in A and C) and U + Th + Pb-rich inclusions (large inclusion on the right).

5.2. Geometry

SRIM/TRIM simulates only the effect of a particle thrown into a target along a single direction. In the present study we are studying the effect of a layer of radioactive material (the outer part of the uranothorianite grain) into a non-radioactive material (diopside and calcite). The vacancy distribution calculated by SRIM/TRIM must then be corrected. First, because radioactive decay emits particles in random directions and not along a single path, and second, because the emitting volume is a layer and not a point. The main output of SRIM/TRIM is the linear density

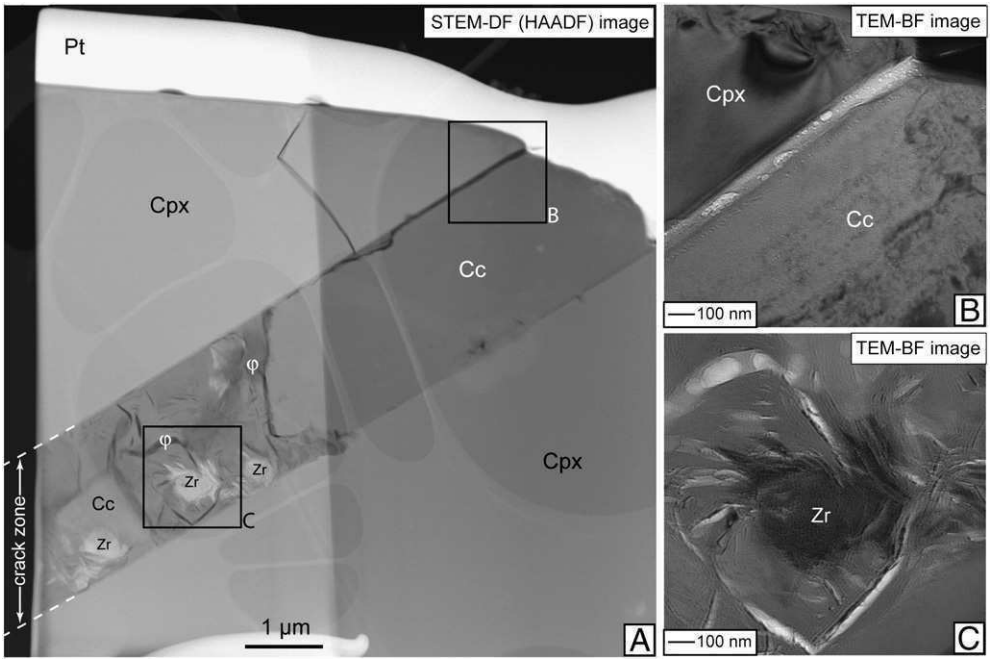

Fig. 8. TEM foil # 1092. STEM — Dark Field (DF) image (A) done with high angle annular dark field (HAADF) detector and TEM-BF images (B and C) showing TEM foil cut across one fracture within Cpx (see Fig. 2D). The fracture (~2 μm wide) is filled with a mixture of clay mineral (φ), calcite (Cc), and a ZrTiCaTh-amorphous phase (Zr), presumably metamict zirconolite (A). Nano-channels, filled with nano-bubbles (fluid inclusions) are visible at the interface between Cpx and the crack border (B); the channel is larger (~70 nm compared to ~40 nm) on the upper side (A and B).

Table 2
Summary of the results of TRIM/SRIM calculations.

	E (MeV)	Alpha particles						E (keV)	Recoil nuclei					
		Diopside		Calcite		Uranothorianite			Diopside		Calcite		Uranothorianite	
		dist	dam	dist	dam	dist	dam		dist	dam	dist	dam	dist	dam
^{238}U														
$^{238}U \Rightarrow ^{234}U$	4.20	12.3	228	14.6	172	9.7	184	71	27	1231	33	983	16	971
$^{234}U \Rightarrow ^{230}Th$	4.78	14.8	225	17.5	186	11.5	190	83	29	1414	36	1129	16	1124
$^{230}Th \Rightarrow ^{226}Ra$	4.69	14.4	221	17.1	178	11.2	198	83	29	1381	36	1117	17	1113
$^{226}Ra \Rightarrow ^{222}Rn$	4.79	14.7	224	17.5	179	11.5	190	86	29	1447	36	1145	18	1141
$^{222}Rn \Rightarrow ^{218}Po$	5.49	18.0	238	21.4	184	14.0	203	90	31	1485	41	1315	19	1312
$^{218}Po \Rightarrow ^{214}Pb$	6.00	20.5	236	24.4	193	15.9	206	112	35	1826	43	1456	22	1467
$^{214}Po \Rightarrow ^{210}Pb$	7.69	30.0	251	35.7	197	22.9	224	146	42	2300	53	1830	24	1836
$^{210}Po \Rightarrow ^{206}Pb$	5.31	17.1	236	20.4	185	17.1	209	103	34	1694	42	1357	20	1341
^{232}Th														
$^{232}Th \Rightarrow ^{228}Ra$	4.01	11.8	219	14.0	173	9.0	136	69	27	1191	32	937	15	927
$^{228}Th \Rightarrow ^{224}Ra$	5.42	18.1	232	21.4	186	13.7	194	95	31	1577	38	1247	19	1224
$^{224}Ra \Rightarrow ^{220}Rn$	5.69	19.4	231	23.0	177	14.6	210	102	32	1647	40	1329	19	1310
$^{220}Rn \Rightarrow ^{216}Po$	6.29	22.5	233	26.7	189	16.9	203	114	35	1848	43	1459	21	1443
$^{216}Po \Rightarrow ^{212}Pb$	6.78	25.2	252	29.9	193	18.8	213	126	38	2032	46	1607	23	1595
$^{212}Bi \Rightarrow ^{208}Tl$ (36%)	6.09	21.5	231	25.5	194	16.1	203	115	34	1863	43	1470	21	1450
$^{212}Po \Rightarrow ^{208}Pb$ (64%)	8.79	37.8	268	44.7	201	27.7	225	166	45	2592	55	2029	44	2038
^{235}U														
$^{235}U \Rightarrow ^{231}Th$	4.69	14.3	221	17.1	178	10.9	192	81	29	1386	35	1095	16	1057
$^{231}Pa \Rightarrow ^{227}Ac$	5.06	16.0	231	19.0	181	12.1	192	89	30	1497	36	1194	18	1179
$^{227}Th \Rightarrow ^{223}Ra$	6.04	20.8	239	24.7	190	15.6	206	108	34	1754	42	1406	21	1382
$^{223}Ra \Rightarrow ^{219}Rn$	5.87	19.9	235	23.7	180	15.0	199	107	35	1742	42	1400	21	1376
$^{219}Rn \Rightarrow ^{215}Po$	6.82	24.9	243	29.6	191	18.6	214	127	37	2035	47	1623	24	1597
$^{215}Po \Rightarrow ^{211}Pb$	7.39	28.2	245	33.5	197	21.0	204	140	41	2244	50	1785	26	1750
$^{211}Bi \Rightarrow ^{207}Tl$	6.62	23.8	241	28.3	185	17.8	207	128	38	2055	47	1634	26	1604
Fission														
^{90}Y (100 MeV)	15.8 μm 39000 vacancies/ion								9.10 μm 43500 vacancies/ion					
^{140}Ce (100 MeV)	17.5 μm 81000 vacancies/ion								8.50 μm 95700 vacancies/ion					

E: energy of the particle, in MeV (alpha) or in keV (recoil); dist: average distance done by the particle in μm (alpha) or in nm (recoil); dam: damage in vacancies/ion.

of vacancies created by a particle, expressed in vacancy/ion/Å, hereafter named $\mathrm{VAC}(r)_{\mathrm{linear}}$ with r being the distance (radius). A series of N particles, along a small distance dr situated at a distance r of the emitting volume creates a number of vacancies $N \cdot \mathrm{VAC}(r)_{\mathrm{linear}} \cdot \mathrm{dr}$. In three dimensions, because of the random direction of the emission, the same amount of vacancies is diluted in a fraction of sphere $4\pi r^2 \cdot \mathrm{dr}$. Therefore the vacancy density per ion around an emitting center is:

$$VAC(r)_{\mathrm{sphere}} = \frac{VAC(r)_{\mathrm{linear}}}{4\pi r^2} \quad (1)$$

This expression is fundamentally the same as in Nasdala et al. (2001), but calculated by differentiation.

As shown in the first part of this paper the thickness of the damaged area (20–30 μm) is small compared to the length of the uranothorianite–diopside/calcite interface (few hundreds of μm). Therefore we will consider the irradiation geometry to be a plane separating a radioactive domain from a non-radioactive domain. Each volume of the irradiated medium situated at a distance L from the interface will receive $\mathrm{VAC}(r)_{\mathrm{sphere}}$ damages from all the particles emitted from the radioactive medium and situated at a distance r. The volume of radioactive medium situated at a distance r is:

$$V\mathrm{rad} = \Omega \cdot r^2 \cdot dr \quad (2)$$

with Ω the solid angle of the cone defined by r and L, which is given by

$$\Omega = 2\pi\left(1 - \frac{L}{r}\right). \quad (3)$$

Combining Eqs. (1)–(3) and summing over the whole radioactive volume, we obtain the density of vacancies created at a distance L of the radioactive half-space:

$$VAC(r)_{\mathrm{plane}} = \int_L^{\infty} \frac{1}{2} \cdot VAC(r)_{\mathrm{linear}} \cdot \left(1 - \frac{L}{r}\right) \cdot \mathrm{dr}. \quad (4)$$

Since we do not have an analytical expression for $\mathrm{VAC}(r)_{\mathrm{linear}}$, this can only by estimated numerically from the output of SRIM/TRIM. The calculation of the exact expression would require calculating each $\mathrm{VAC}(r)_{\mathrm{linear}}$ function for all L and all particles. In order to maintain the calculation time reasonable we decided, for each particle and each target, to use only the $\mathrm{VAC}(r)_{\mathrm{linear}}$ function calculated for the target mineral. The consequences of this approximation will be discussed later.

5.3. The time scale

The petrological study showed that the altered aureole was formed by recrystallization of the target minerals, calcite or diopside. To estimate the amount of damage that the target had experienced when recrystallization occurred, we should know the time at which damage started, assumed to be the age of the rock formation (550 Ma), and the time at which alteration and recrystallization occurred, which is unknown. This initial damage at recrystallization is not zero because some lead, presumably radiogenic has been found in the altered aureole, but it can be from few millions to few hundredths of millions years. This is a major uncertainty, which affect the amount of damage and the relative proportion of damages due to the ^{235}U, ^{238}U and ^{232}Th chains. However neither the size of the damaged area, which depends only on the nature of the target and the particles energy, nor the shape of the vacancy distribution, which depends mainly on the shape of

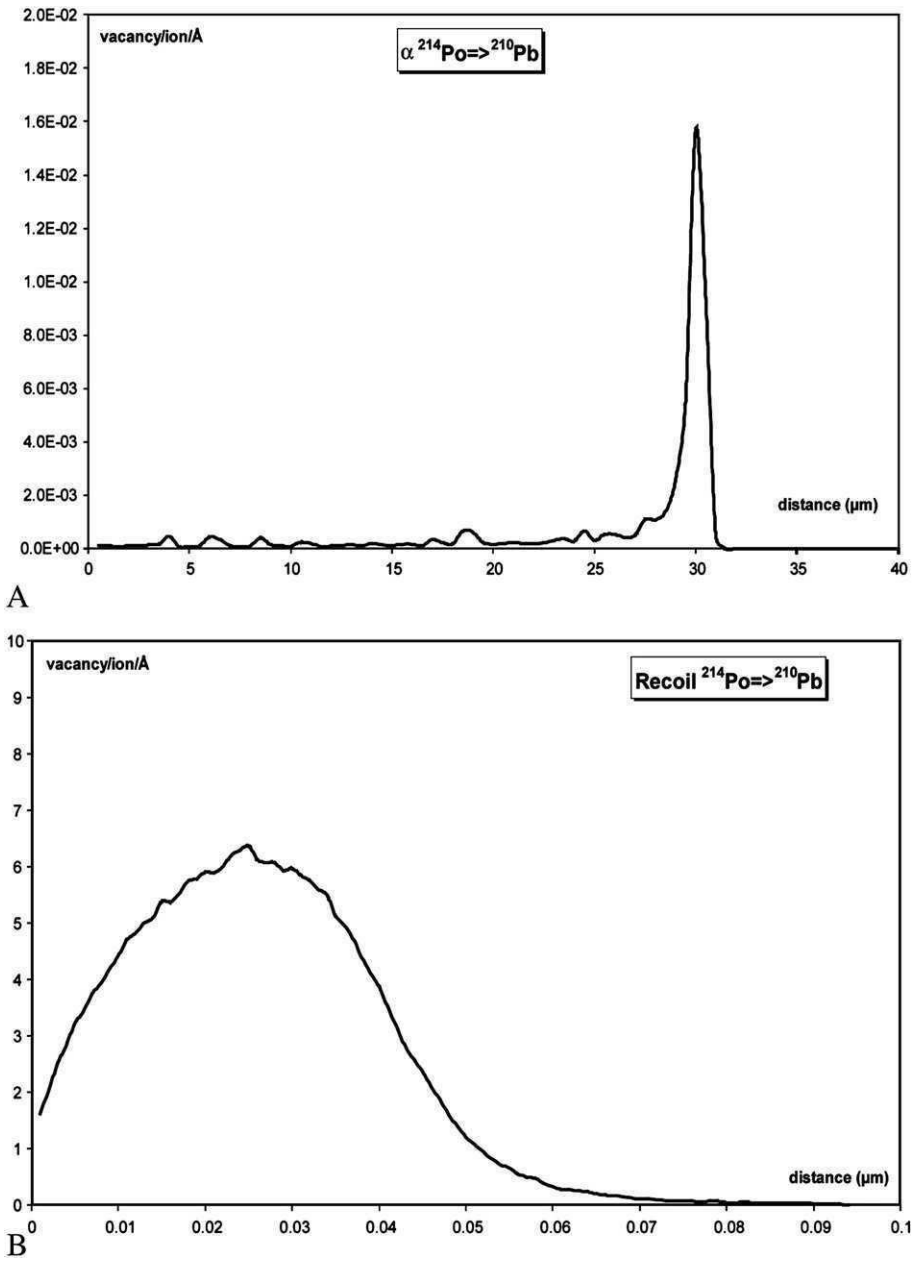

Fig. 9. Projection of the vacancy distribution created by a 7.69 MeV α particle (A) and the corresponding recoil (B) nuclei (^{210}Pb at 146 keV) in diopside. The fast α particle produces vacancies only at the end of its displacement, when it has been slowed down enough by ionization to interact with target nuclei. The slow recoil nucleus creates vacancies all along its trajectory. Note that vertical and horizontal scales are very different in the two figures.

individual particle damaging and of the geometrical corrections, are affected. All the calculations have been carried out assuming 550 Ma as the irradiation time. As a result of this major uncertainty, we made no attempt to estimate dpa (displacements per atom) from the number of vacancies in target minerals.

5.4. Results

Uranothorianite has been auto-irradiated since its formation. It is possible to calculate the number of vacancies directly from the average damage in Table 2, integrated over 550 Ma, and converted it in dpa (displacement per atom). The calculated average of 240 dpa over 550 Ma, when compared to the dose necessary to completely amorphized thorite ($ThSiO_4$), ~0.20 dpa at room temperature (Meldrum et al., 1999), suggests that the uranothorianite should be completely amorphous. However, because electron diffraction patterns (SAD—Fig. 4) demonstrate that it is crystalline, uranothorianite must self-anneal by some processes. As a comparison, amorphization of UO_2 seems impossible, because of the highly rapid recombination of the bonding; for an irradiation dose equivalent to 25 dpa at ~170 °C, UO_2 is still crystalline (Matzke and Turos, 1992; Matzke and Wang, 1996).

Results for diopside and calcite are presented in Figs. 10 and 11. Spontaneous fission of ^{238}U is such rare event that it can be neglected. The shapes of the curves, representing the damage due to α particles as a function of distance from uranothorianite are similar. Most damage is accumulated at short distances (about 15 μm in diopside and 17 μm in calcite). The more distant part corresponds to the area damaged only by the more energetic particles emitted close to the uranothorianite surface. The total damaged area is then about 35 μm wide in calcite and 30 μm in diopside. Recoils nuclei create 1000 times more damage than α particles, with a very steep decrease for a damaged zone of 60 nm in calcite and 50 nm in diopside.

The thickness of the damaged area calculated for α in diopside is similar to the width of the recrystallized area observed in thin section. The thickness of the porous calcite layer around along the primary calcite–thorianite interface is more difficult to estimate but is also similar to the size of the area damaged by α as calculated above. However the characteristic distances calculated for the damage of recoil nuclei (50 to 60 nm) are far away from the size of the totally amorphous layer seen at the calcite–uranothorianite interface (150–250 nm).

5.5. Effect of wandering recoils

Modeling the effect of recoil nuclei by a succession of individual ions projected from uranothorianite into the target is, actually, a poor representation of the real process occurring during the radioactive decay of a chain. In decay chains the recoil nucleus is the next radioactive element. During radioactive decay, the recoil moves of few tens of nm, in a random direction. Therefore, there is a possibility, for decay occurring close to the uranothorianite surface, that after decay the recoil is indeed located out of the uranothorianite. Then next decay will occur inside the diopside (or calcite), and the new recoil will move again, in a random direction. For damages created by α this effect can be neglected, because the path of α is much longer than the possible displacement of the recoil, but for the recoil itself, the damaged area can be significantly enlarged by the "wandering recoil effect": a series of recoils that would move always in the same direction, although very unlikely, can ends few hundredths of nm inside diopside (or calcite). In order to quantitatively estimate this effect we simulated this effect by the following procedure: (1) for each decay, a random direction is chosen; (2) the average damage is distributed along the path, as calculated by SRIM/TRIM; (3) the recoil (daughter) nucleus is displaced in that direction, at the average distance shown in Table 2; (4) the next decay in the chain is processed from this position, as described in (1)–(2)–(3). For each chain and for both diopside and calcite we simulated 1000 decay chains. At the end of the calculation, the radial distribution of the damages is calculated. Strictly, this procedure only simulates a decay chain initiated exactly at the interface. Again, because we do not know the time scale, but only the shape of the curves, only the characteristics distances have real meanings in this simulation. The results are presented in Fig. 12. The main result is that the thickness of the area damaged by the recoils is approximately multiplied by 3 because of the

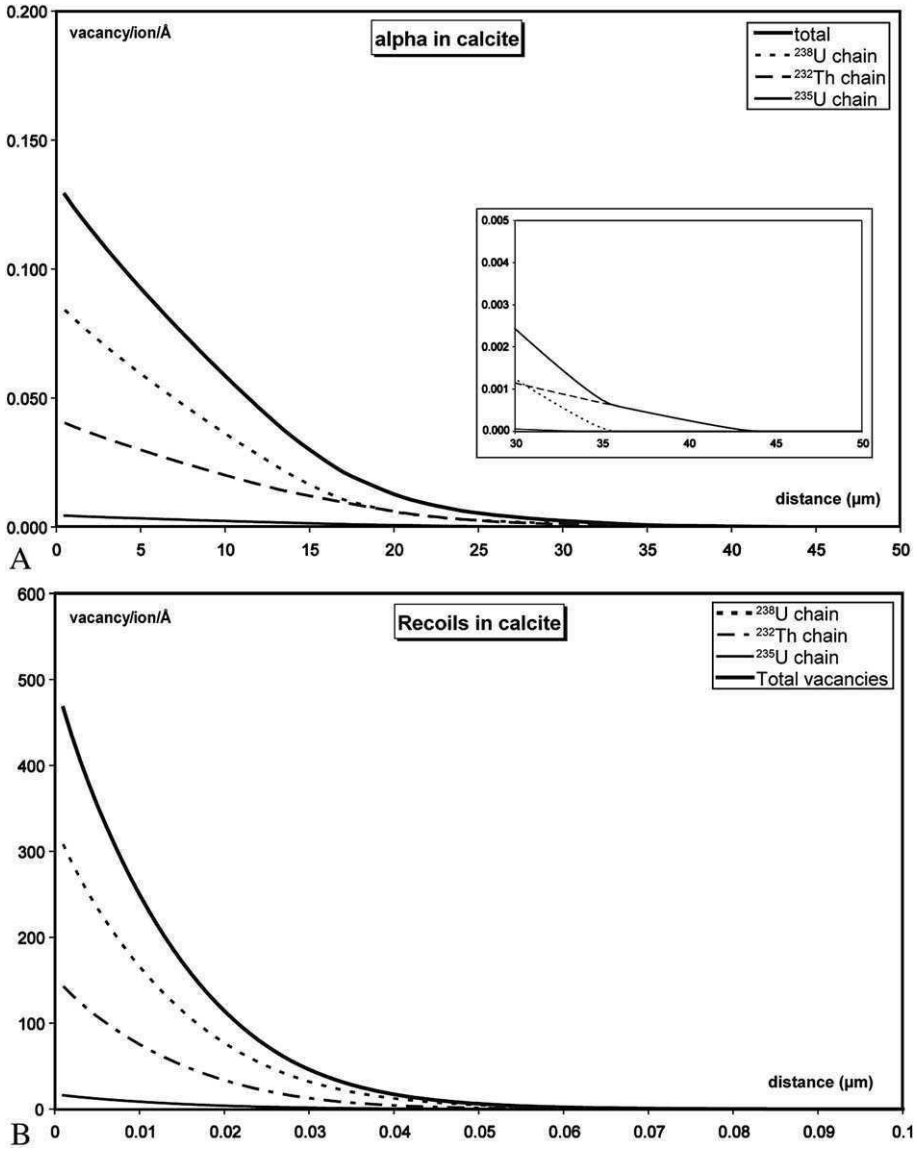

Fig. 10. Spatial distribution of the vacancies created in calcite by α particles (A) and recoil nuclei (B) emitted by uranothorianite. The calculation includes all particles from the three decay chains, integrated for 550 Ma. It assumes that uranothorianite is a semi-infinite emitting medium irradiating a semi-infinite calcite half-space, separated by a plane. Note that vertical and horizontal scales are very different in the two figures.

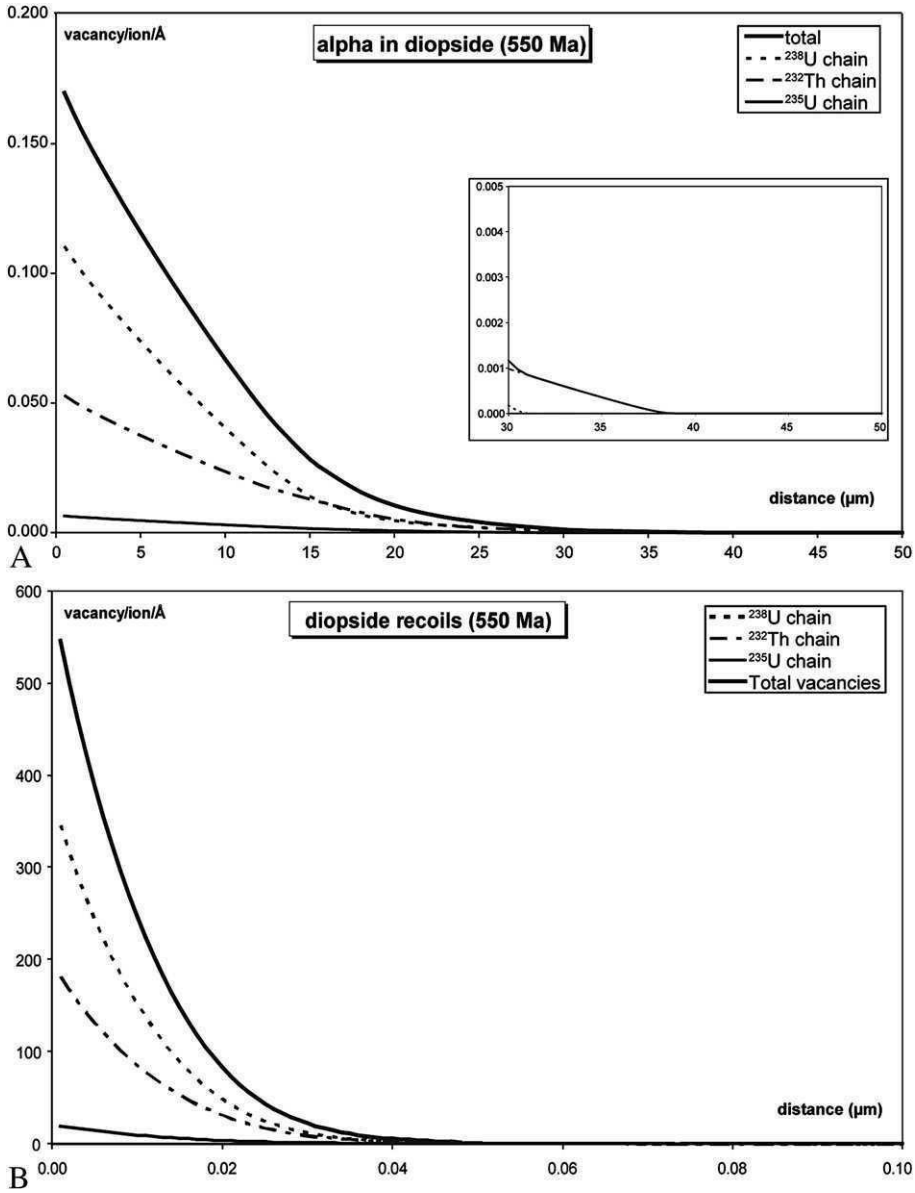

Fig. 11. Spatial distribution of the vacancies created in diopside by α particles (A) and recoil nuclei (B) emitted by uranothorianite. The calculation includes all particles from the three decay chains, integrated for 550 Ma. It assumes that uranothorianite is a semi-infinite emitting medium irradiating a semi-infinite diopside half-space, separated by a plane. Note that vertical and horizontal scales are very different in the two figures.

"wandering recoil effect". With this correction, the size of the area damaged by recoil nuclei in calcite is in rather good agreement with the thickness of the totally amorphous layer at the calcite–uranothorianite interface (Figs. 4 and 7).

6. Interpretation and discussion

6.1. A reasonable history of radiohalos in Tranomaro skarns

From petrographical study and damage modeling, the evolution of the rock can be reconstructed as follows. The initial rock is a high-temperature marble, mainly made of aluminous diopside and primary calcite, with some large uranothorianite grains. As soon as the latter is formed, radioactive decays start, with three consequences: (1) radiogenic Pb accumulates in uranothorianite; (2) radiation damage accumulates in uranothorianite and in the contiguous minerals; and (3) the uranothorianite grains swells because of radiation damage. For uranothorianite similar to the minerals studied here, Evron et al. (1994) estimated a macroscopic volume expansion of ~1.5%. With increasing time, swelling creates radial cracks in diopside and calcite, and radiation damage accumulates and weakens calcite and diopside around uranothorianite. A heavily damaged (amorphous) thin layer is created along the interface by the recoils, and a partially or totally damaged layer, 20–40 μm is created by α. Since no Helium bubbles was observed within uranothorianite by TEM, it is supposed that radiogenic Helium diffused out of the crystal through the cracks. After some time, a low-temperature fluid infiltrates through the rock, using the cracks and the weak interfaces as preferential pathways. The damaged part of diopside is retrogressed as a mixture of clay and secondary calcite. The damaged part of primary calcite recrystallized as a secondary porous calcite layer. At this stage, cracks in calcite are healed, whereas, cracks in diopside are partially filled by various secondary material (Fig. 8; calcite, zirconolite, clay mineral). Uranothorianite is also affected by fluids, as shown by the presence of Pb, U, and Th in the reaction zones (Fig. 6) and in the amorphous layers A and C (Figs. 4 and 5), and the presence of ThO_2 chains (Figs. 4, 5 and 7). However the fact that the chemical ages are in good agreement with the age of the rock indicates that this mineral is not deeply penetrated

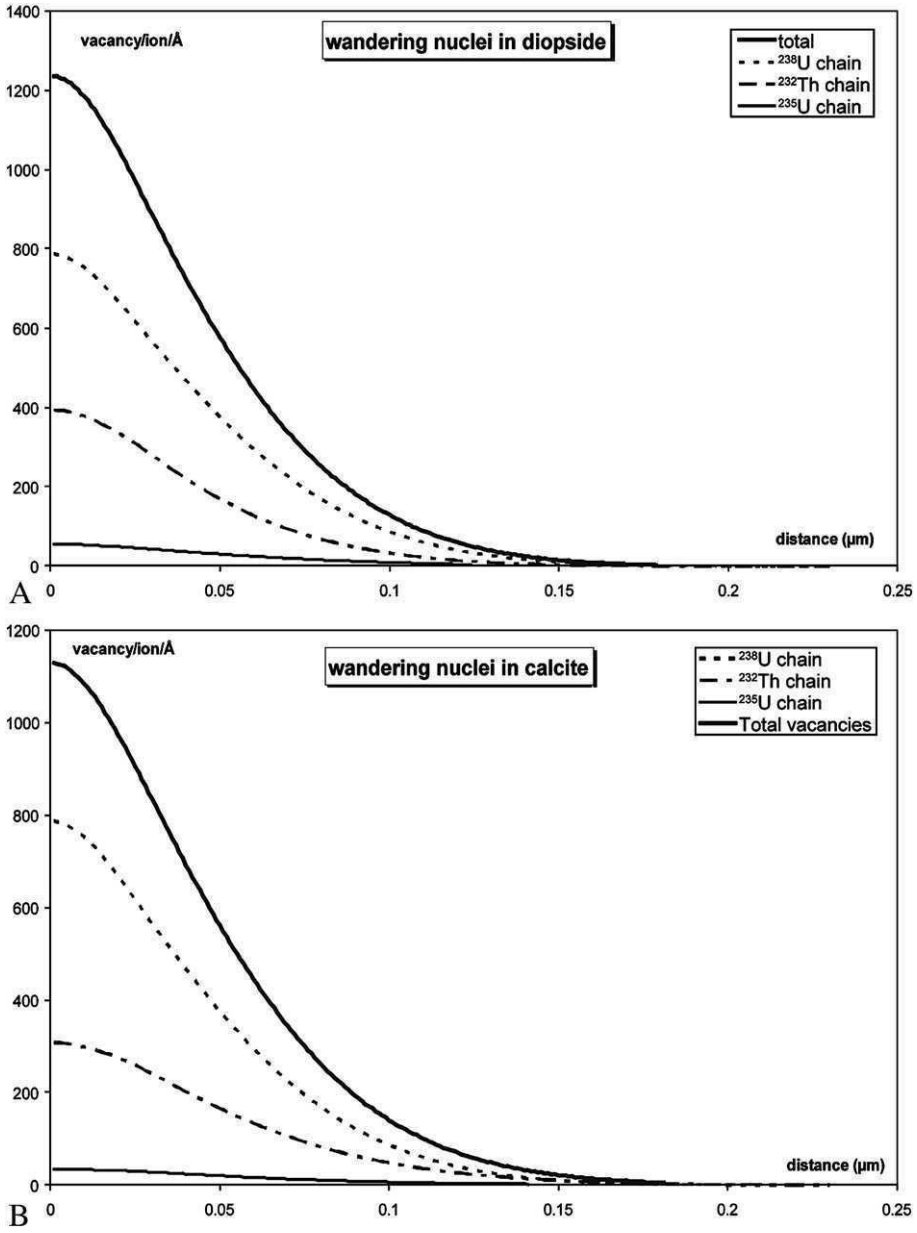

Fig. 12. Spatial distribution of the vacancies created in diopside (A) and calcite (B) by wandering nuclei. The model simulates the random trajectories of recoil nuclei during the successive decays in the three decay chains, and estimates, via TRIM/SRIM simulation the vacancies created along the path. The integration time is 550 Ma. Those diagrams should be compared to Figs. 10 and 11(B).

by fluids. During fluid infiltration, some elements are partially redistributed, including elements which are not obviously present in the thin section such as Zr. After this hydrothermal episode, the newly formed phases are again affected by radioactive damage.

The exact significance of the features observed along the uranothorianite and calcite is at this stage not totally explained. However the B zone, a chain of ThO_2 grains, suggest an *in-situ* reprecipitation of ThO_2 during partial dissolution of uranothorianite, as it is commonly observed in experiments with ThO_2 (Seydoux-Guillaume et al., 2002; Heisbourg et al., 2003; Heisbourg et al., 2004).

6.2. Some properties of uraninite, calcite, and diopside relative to radiation damages

The observations made on this sample support several hypotheses on the behavior of calcite, diopside and uranothorianite under irradiation. Uranothorianite is remarkably resistant to irradiation damage. This is not unexpected, since uraninite, which is isostructural with uranothorianite remains crystalline (Evron et al. 1994; Janeczek et al. 1996). By contrast, a thorium silicate ($ThSiO_4$) that accumulated approximately the same dose as the uranothorianite studied here ($\sim 5\times10^{20}$ α/g) is completely amorphous (Seydoux-Guillaume et al., 2007). This observation is consistent with higher resistance to amorphization by radiation damage (or greater ability to self-anneal) in minerals for which the long-range ionic forces dominates over the short-range covalent forces (Trachenko, 2004), as in the case for uranothorianite when compared to thorite.

Contrary to uranothorianite, diopside seems to be highly sensible to radiation damage. The average size of the retrogressed zone is 27 µm. At this distance the damage is only 2% of the maximum damage created by the α at the contact with uranothorianite. For 550 Ma of irradiation, this would correspond to 0.0014 dpa, so it means that the resistance of diopside relative to low-temperature fluids is modified even if about 1/1000 atoms are displaced. We should recall that

550 Ma is the maximum for the irradiation time since it assumes that retrogression occurred at the present time.

The limit between pristine diopside and the retrogressed area is very sharp; there is no intermediate zone in which diopside would be partly retrogressed. This suggests that there is a threshold in the sensitivity of damaged diopside to low temperature fluid. Below a certain value of damage the diopside behaves as an undamaged diopside, and is not affected by alteration. We should recall that diopside is a common mineral in heavy minerals concentrates in river, so it is not normally destroyed by low-T fluids.

In calcite the porous layer, which can be assumed to be the equivalent of the retrogressed zone in diopside, is ~10 to 15 μm wide, as estimated from Fig. 2. At this distance damage is 45 to 25% of the maximum (550 Ma) α damage, for 0.013 to 0.0055 dpa. Calcite seems then more resistant to irradiation damage than diopside, probably due to the type of interatomic forces in that structure (Trachenko, 2004). It is important to remember, that diopside crystals that are not in contact with uranothorianite in the rest of the rock are pristine. This demonstrates that irradiation is responsible for the destabilization of diopside by fluids. However, calcite directly in contact with uranothorianite (see presence of Ca within amorphous zone A (Figs. 4A and 5) is amorphous, showing the strong effect of "continuous irradiation by wandering recoil". It should be also noted that calcite is always crystalline, even at the contact with uranothorianite where the damage rate can be up to 0.055 dpa.

Outside the modified area around uranothorianite, the rock is very fresh; the only indication of the low-T fluid infiltration is secondary material along the diopside–uranothorianite interfaces and, at nano-scale, in swelling structures, i.e. cracks (Fig. 8). This definitely shows that uranothorianite grains create weak zones in the rock, by destroying the surrounding minerals, and by creating swelling cracks.

The thickness of the retrogressed area at the diopside–uranothorianite interface is approximately constant all around the thin section. It means that the effect of irradiation damage in diopside does not depend on the orientation of the diopside crystals although it is an anisotropic chain-silicate. The only visible indication of the anisotropy of diopside is the local presence of indentation at the pristine-retrogressed limit, due to limited fluid infiltration along cleavage surfaces.

6.3. Reliability of the conclusions

The above conclusions are based on a detailed study of structures surrounding a single uranothorianite grain. The representativity of the studied zone can then be legitimately questioned. Many features observed around this particular grain are visible in the whole thin section, such as the radiating cracks, the presence of retrogressed zone along the diopside–uranothorianite interface, and the presence of a porous layer along the calcite–uranothorianite. Those features are also present in all studied samples of the same rock. Observations at the nano-scale by coupling FIB/TEM analyses, like the presence of a wide amorphous zone along the calcite–uranothorianite boundary, or the presence of chains of ThO_2 crystals, which are time-consuming, cannot easily be multiplied all around a thin section, but are regular in shape and size, and are in agreement with damage model. Therefore we are quite confident that these are general features in this sample. Moreover, similar observations have been reported in other studies (Seydoux-Guillaume et al., 2003, 2007; Nasdala et al., 2006; Seydoux-Guillaume, unpublished), suggesting that it is common in rocks containing radioactive minerals. Some observations are clearly accidental, and may not be representative, such as the presence of zirconolite grains in the fractures.

6.4. Reliability of the model

In this study the SRIM/TRIM model provided several important constraints. This software has the advantage of being the most sophisticated program available for non-specialist; on the other hand it has some limitations; for example it considers all materials as isotropic, and neglects the effect of crystalline structures. However, the fact that the size of damaged area in diopside is constant whatever its orientation provides an *a posteriori* justification of this assumption. Diopside is a chain-based, highly anisotropic structure, and if radiation damage is sensitive to crystal anisotropy, it should be visible in this mineral.

7. Conclusions

Radiohalos are complex structures, which deserve detailed study. Since radiation damage has a visible effect at the thin section scale, but also affects the structure of crystals at the atomic scale, studies must be conducted with a variety of techniques, including FIB/TEM for the nano-scale. Radiohalos are unique sources of information for understanding the behavior of minerals submitted to irradiation damages, even for non-radioactive minerals. This approach allows to study the effects of long-term irradiation and is thus very complementary to other methods that involve doping experiments with short-lived isotopes, which are far more expensive.

In the present study we have demonstrated the high resistance of uranothorianite to self-irradiation damage, in agreement with previous results (Evron et al., 1994), and, by contrast, the high sensitivity of diopside to radiation damage from neighbouring uranothorianite. TRIM/SRIM simulations have been shown to be able to correctly simulate radiation damage, even in complex minerals such as diopside.

Finally, we would like to emphasize that radiohalos are actually a point of chemical and mechanical weakness in a rock and probably a starting point for alteration.

Acknowledgements

FIB/TEM analyses have been done thanks to the financial support for travels to Potsdam from PROCOPE (2005–2006) No. 09638ZB. The authors want to thank Ph. De Parseval and T. Aigouy for their technical assistance with the Electron Microprobe and with the SEM, and L. Datas and L. Weingarten for their technical assistance with the TEM at the TEMSCAN service from UPS. Constructive comments from R.C. Ewing and an anonymous reviewer were appreciated; we also want to thank J. Hanchar for his excellent editorial work. Thanks to M. Jessel for correcting the English language.

References

Balan, E., Allard, T., Fritsch, E., Sélo, M., Falguères, C., Chabaux, F., Pierret, M.P., Calas, G., 2005. Formation and evolution of lateritic profiles in the middle Amazon basin: insights from radiation-induced defects in kaolinite. Geochimica et Cosmochimica Acta 69, 2193–2204.

Begg, B., Hess, N.J., Weber, W.J., Conradson, S.D., Scheiger, M.J., Ewing, R.C., 2000. XAS and XRD study of annealed ^{238}Pu and ^{239}Pu substituted zircons ($Zr_{0.92}Pu_{0.08}SiO_4$). Journal of Nuclear Materials 278, 121–224.

Black, L.P., Fitzgerald, J.D., Harley, S.L., 1984. Pb isotopic composition, colour, and microstructure of monazites from a polymetamorphic rock in Antarctica. Contrib. Mineral. Petrol. 85, 141–148.

Boulvais, P., Fourcade, S., Gruau, G., Moine, B., Cuney, M., 1998. Persistence of pre-metamorphic C and O isotopic signatures in marbles subject to Pan-African granulite facies metamorphism and U–Th mineralization (Tranomaro, South East Madagascar). Chemical Geology 150, 247–262.

Boulvais, P., Fourcade, S., Moine, B., Gruau, G., Cuney, M., 2000. Rare-earth elements distribution in granulite-facies marbles: a witness of fluid–rock interaction. Lithos 53, 117–126.

Burakov, B.E., Hanchar, J.M., Garbusov, V.M., Zirlin, V.A., 2002. Synthesis and investigation of Pu doped single crystal zircon $ZrPuSiO_4$. Radiochimica acta 90, 95–97.

Crocombette, J.P., Ghaleb, D., 2001. Molecular dynamics modeling of irradiation damage in pure and uranium doped zircon. Journal of Nuclear Materials 295, 167–178.

Davis, D.W., Krogh, T.E., 2000. Preferential dissolution of ^{234}U and radiogenic Pb from α-recoil-damaged lattice sites in zircon: implications for thermal histories and Pb isotopic fractionation in the near surface environment. Chemical Geology 172, 41–58.

Evron, R., Kimmel, G., Eyal, Y., 1994. Thermal recovery of self-radiation damage in uraninite and thorianite. Journal of Nuclear Materials 217, 54–66.

Ewing, R.C., 1975. The crystal chemistry of complex niobium and tantalum oxides IV. The metamict state: discussion. American Mineralogist 60, 728–733.
Ewing, R.C., 1994. The metamict state: 1993—the centennial. Nuclear Instruments and Methods in Physics Research B91, 22–29.
Ewing, R.C., Wang, L.M., 2002. Phosphates as nuclear waste forms. In: Kohn, M.J., Rakovan, J., Hughes, J.M., Ribbe, P.H. (Eds.), Phosphates: Geochemical, Geobiological and Materials Importance. . Reviews in Mineralogy and Geochemistry, vol. 48. Mineralogical Society of America, pp. 673–699.
Ewing, R.C., Weber, W.J., Clinard Jr., F.W., 1995. Radiation effects in nuclear waste forms. Progress in Nuclear Energy 29, 63–127.
Ewing, R.C., Chakoumakos, B.C., Lumpkin, G.R., Murakami, T., Greegor, R.B., Lytle, F.W., 1988. Metamict minerals: natural analogues for radiation damage effects in ceramic nuclear waste forms. Nuclear Instruments and Methods in Physics Research B32, 487–497.
Ewing, R.C., Meldrum, A., Wang, L.M., Wang, S.X., 2000. Radiation-induced amorphisatio. In: Redfern, S.A.T., Carpenter, M.A., Ribbe, P.H. (Eds.), Transformation Processes in Minerals. . Reviews in Mineralogy and Geochemistry, vol. 39. Mineralogical Society of America, pp. 319–361.
Ewing, R.C., Meldrum, A., Wang, L.M., Weber, W.J., Corrales, L.R., 2003. Radiation damage in zircon. In: Hanchar, J.M., Hoskin, P.W.O. (Eds.), Zircon. . Reviews in Mineralogy and Geochemistry, vol. 53. Mineralogical Society of America, pp. 387–425.
Farges, F., 1997. Coordination of Ti4+ in silicate glasses: A high-resolution XANES spectroscopic study at the Ti K edge. Am. Mineral. 82, 36–43.
Farges, F., Calas, G., 1991. Structural analysis of irradiation damage in zircon and thorite. An X-ray absorption spectroscopic study. American Mineralogist 76, 60–73.
Farges, F., Ewing, R.C., Brown, G.E., 1993. The structure of aperiodic, metamict (Ca,Th) ZrTi2O7 (zirconolite): an EXAFS study of the Zr, Th and U sites. Journal of Material Research 8, 1983–1995.
Farnan, I., Balan, E., Pickard, C.J., Mauri, F., 2003. The effect of radiation damage on local structure in the crystalline fraction of $ZrSiO_4$: investigating the Si-29 NMR response to pressure in zircon and reidite. American Mineralogist 88, 1663–1667.
Gentry, R.V., 1973. Radioactive halos. Annual review in Nuclear Science 23, 347–362.
Gentry, R.V., 1974. Radiohalos in a radiochronological and cosmological perspective. Science 184, 62–66.
Harfouche, M., Farges, F., Crocombette, J.-P., Flank, A.-M., 2005. XAFS and molecular dynamics study of the structural environment around actinides and network formers in natural minerals analogues of ceramics for nuclear waste storage. Physica Scripta T115, 928–930.
Hawthorne, F.C., Groat, L.A., Raudsepp, M., Ball, N.A., Kimata, M., Spike, F.D., Gaba, R., Halden, N.M., Lumpkin, G.R., Ewing, R.C., Greegor, R.B., Lytle, F.W., Ercit, T.S., Rossman, G.R., Wicks, F.J., Ramik, R.A., Sherriff, B.L., Fleet, M.E., McCammon, C., 1991. Alpha-decay damage in titanite. American Mineralogist 76, 370–396.
Headley, T.J., Ewing, R.C., Haaker, R.F., 1981. Amorphous structure of metamict minerals observed by TEM. Nature 293, 449–450.
Heisbourg, G., Hubert, S., Dacheux, N., Ritt, J., 2003. The kinetics of dissolution of $Th_{1-x}U_xO_2$ solid solutions in nitric media. Journal of Nuclear Materials 321, 141–151.
Heisbourg, G., Hubert, S., Dacheux, N., Purans, J., 2004. Kinetic and thermodynamic studies of the dissolution of thoria-urania solid solutions. Journal of Nuclear Materials 335, 5–13.
Janeczek, J., Eby, R.K., 1993. Annealing of radiation damage in allanite and gadolinite. Physics and Chemistry of Minerals 19, 343–356.
Janeczek, J., Ewing, R.C., Oversby, V.M., Werme, L.O., 1996. Uraninite and UO_2 in spent nuclear fuel: a comparison. Journal of Nuclear Materials 238, 121–130.
Joly, J., 1907. Pleochroic halos. Philosophical Magazine 13, 381–383.
Lumpkin, G.R., Chakoumakos, B.C., 1988. Chemistry and radiation effects of thorite-group minerals from the Harding pegmatite, Taos County, New Mexico. American Mineralogist 73, 1405–1419.
Lumpkin, G.R., Ewing, R.C., 1988. Alpha decay damage in minerals of the pyrochlore group. Physics and Chemistry of Minerals 16, 2–20.
Lumpkin, G.R., Chakoumakos, B.C., Ewing, R.C., 1986a. Mineralogy and radiation effects of microlite from the Harding Pegmatite, Taos County, New Mexico. American Mineralogist 71, 569–588.
Lumpkin, G.R., Ewing, R.C., Chakoumakos, B.C., Greegor, R.B., Lytle, F.W., Forltyn, E.M., Clinard Jr., F.W., Boatner, L.A., Abraham, M.M., 1986b. Alpha-recoil damage in zirconolite ($CaZrTi_2O_7$). Journal of Material Research 1, 564–576.
Lumpkin, G.R., Eby, R.K., Ewing, R.C., 1991. Alpha-recoil damage in titanite ($CaTiSiO_5$): direct observation and annealing study using high resolution transmission electron microscopy. Journal of Material Research 6, 560–564.
Linberg, M.L., Ingram, B., 1964. Rare-earth silicatian apatite from the Adirondack Mountains, New-York. US Geological Survey Professional Paper 501-B, B64–B65.
Matzke, H.j., Turos, A., 1992. Ion implantation studies of UO_2 and UN. Journal of Nuclear Materials 188, 285–292.
Matzke, H.j., Wang, L.M., 1996. High-resolution transmission electron microscopy of ion irradiated uranium oxide. Journal of Nuclear Materials 231, 155–158.
Meldrum, A., Boatner, L.A., Weber, W.J., Ewing, R.C., 1998. Radiation damage in zircon and monazite. Geochimica et Cosmochimica Acta 62, 2509–2520.
Meldrum, A., Zinckle, S.J., Boatner, L.A., Ewing, R.C., 1999. Heavy-ion irradiation effects in the ABO4 orthosilicates: decomposition, amorphization, and recrystallization. Physical Review B59, 3981–3992.
Meunier, J.D., Sellier, E., Pagel, M., 1990. Radiation damage rims in quartz from uranium bearing sandstones. Journal of Sedimentary Petrology 60, 53–58.
Moine, B., Rakotondratsima, C., Cuney, M., 1985. Les pyroxénites à urano-thorianite du sud-est de Madagascar, conditions physico-chimiques de la métasomatose. Bulletin de Minéralogie 108, 325–340.
Moine, B., Ramambazafy, A., Rakotondrazafy, M., Ravololomiandrinarivo, B., Cuney, M., de Parseval, P., 1998. The role of fluorine-rich fluids in the formation of the thorianite and sapphire deposits of S.E. Madagascar. 8th Goldschmidt Conference. Mineralogical Magazine, vol. 62A, pp. 999–1000.
Mügge, O., 1907. Radioaktivität als Ursache der pleochroitischen Höfe. Zentralblatt Mineralogie Geologie 71, 529–532.
Murakami, T., Chakoumakos, B.C., Ewing, R.C., Lumpkin, G.R., Weber, W.J., 1991. Alpha-decay event damage in zircon. Am. Mineral. 76, 1510–1532.
Nasdala, L., Irmer, G., Wolf, D., 1995. The degree of metamictization in zircons a Raman spectroscopic study. European Journal of Mineralogy 7, 471–478.
Nasdala, L., Wenzel, M., Andrut, M., Wirth, R., Blaum, P., 2001. The nature of radiohaloes in biotite: experimental studies and modeling. American Mineralogist 86, 498–512.
Nasdala, L., Wildner, M., Wirth, R., Groshopf, N., Pal, D.C., Möller, A., 2006. Alpha particle haloes in chlorite and cordierite. Mineralogy and Petrology 86, 1–27.
Odom, A.L., Rink, W.L., 1989. Giant radiation-induced colored halos in quartz solution to a riddle. Science 246, 107–109.
Ouchani, S., Dran, J.C., Chaumont, J., 1997. Evidence of ionization annealing upon helium-ion irradiation of pre-damaged fluorapatite. Nuclear Instruments and Methods. Physical Research, vol. B132, pp. 447–451.
Overwijk, M.H.F., van den Heuvel, F.C., Bulle-Lieuwma, C.W.T., 1993. Novel scheme for the preparation of transmission electron microscopy specimens with a focused ion beam. Journal of Vacuum Science and Technology 11, 202.
Owen, M.R., 1988. Radiation damage halos in quartz. Geology 16, 529–532.
Paquette, J.L., Nédélec, A., Moine, B., Rakotondrazafy, M., 1994. U–Pb, single zircon evaporation and Sm–Nd isotopic study of a granulite domain in SE Madagascar. Journal of Geology 102, 523–538.
Rakotondratsima, C., 1983. Les pyroxénites à Uranothorianite du Sud-Est de Madagascar: étude pétrographique, minéralogique et géochimique. Thesis, Claude Bernard University-Lyon, 226 pp.
Rakotondrazafy, M., 1995. La hibonite ($CaAl_{12}O_{19}$) du Sud-Est de Madagascar. Caractères et modalités de formation dans les skarns à thorianite du faciès granulite (Unpublished). Thesis, Antananarivo University, Madagascar.
Rakotondrazafy, M., Moine, B., Cuney, M., 1996. Mode of formation of hibonite ($CaAl_{12}O_{19}$) within the U–Th skarns from the granulites of S–E Madagascar. Contribution to Mineralogy and Petrology 123, 190–201.
Ramambazafy, A., 1998. Granites et fluides en relation avec les skarns à thorianite dans les granulites du S.E. de Madagascar. Thesis, Paul Sabatier Toulouse III University, 302 pp.
Ramambazafy, A., Moine, B., Rakotondrazafy, M., Cuney, M., 1998. Signification des fluides carboniques dans les granulites et les skarns du Sud-Est de Madagascar. Compte Rendu de l'académie des Sciences 327, 743–748.
Roberts, S., McCaffrey, J., Giannuzzi, L., Stevie, F., Zaluzec, N., 2001. Advanced techniques in TEM specimen preparation. In: Xiao-Feng, Zhang., Ze, Zhang (Eds.), Progress in transmission electron microscopy, vol. 1. Springer Series in Surface Sciences, 38, pp. 336–342.
Romer, R., 2003. Alpha-recoil in U–Pb geochronology: effective sample size matters. Contribution to Mineralogy and Petrology 145, 481–491.
Seydoux-Guillaume, A.M., Paquette, J.L., Wiedenbeck, M., Montel, J.M., Heinrich, W., 2002. Experimental resetting of the U–Th–Pb systems in monazite. Chemical Geology 191, 165–181.
Seydoux-Guillaume, A.M., Goncalves, P., Wirth, R., Deutsch, A., 2003. TEM study of polyphasic and discordant monazites: site specific specimen preparation using the Focused Ion Beam technique. Geology 31, 973–976.
Seydoux-Guillaume, A.M., Wirth, R., Deutsch, A., Schärer, U., 2004. Microstructure of 24 – 1928 Ma concordant monazites: implications for geochronology and nuclear waste deposits. Geochimica et Cosmochimica Acta 68, 2517–2527.
Seydoux-Guillaume, A.M., Wirth, R., Ingrin, J., 2007. Contrasting response of $ThSiO_4$ and monazite to natural irradiation. European Journal of Mineralogy 19, 7–14.
Trachenko, K.O., 2004. Understanding resistance to amorphization by radiation damage. Journal of Physics: Condensed Matter 16, 1491–1515.
Trachenko, K.O., Dove, M.T., Salje, E.K.H., 2001. Atomistics modeling of radiation dammage in zircon. Journal of Physics: Condensed Matter 13, 947–952.
Vance, E.R., Metson, J.B., 1985. Radiation damage in natural titanites. Physics and Chemistry of Minerals 12, 255–260.
Wang, L.M., Ewing, R.C., 1992. Ion beam induced amorphization of complex ceramic materials — minerals. Materials Research Society Bulletin 13, 38–44.
Weber, W.J., Ewing, R.C., Catlow, C.R.A., Diaz de la Rubia, T., Hobbs, L.W., Kinishita, C., Matzke, H.J., Motta, A.T., Nastasi, M., Salje, E.H.K., Vance, E.R., Zinkle, S.J., 1998. Radiation effects in crystalline ceramics for the immobilization of high-level nuclear waste and plutonium. Journal of Material Research 13, 1434–1484.
Weber, W.J., Ewing, R.C., Wang, L.M., 1994. The radiation-induced crystalline-to-amorphous transition in zircon. Journal of Materials Research 9, 688–698.
Wirth, R., 2004. Focused Ion Beam (FIB): a novel technology for advanced application of micro- and nanoanalysis in geosciences and applied mineralogy. European Journal of Mineralogy 16, 863–876.
Young, R.J., 1997. Application of the focused ion beam in materials characterization and failure analysis. Microstructural Science 25, 491–496.
Zhang, M., Salje, E.K.H., 2001. Infrared spectroscopic analysis of zircon: radiation damage and the metamict state. Journal of Physics: Condensed Matter 13, 3057–3071.
Zhang, M., Salje, E.K.H., Bismayer, U., Groat, L.A., Malcherek, T., 2002. Metamictization and recrystallization of titanite: an infrared spectroscopic study. American Mineralogist 87, 882–890.
Ziegler, J.F., 2006. SRIM: the stopping and range of ions in matter. Instruction Manual.

European Journal of Mineralogy (2010), **22**, 235–244.

Dominance of mechanical over thermally induced damage during femtosecond laser ablation of monazite

ANNE- MAGALI SEYDOUX-GUILLAUME[1,*], RÉMI FREYDIER[1,4], FRANCK POITRASSON[1], FRANÇOIS-XAVIER D'ABZAC[1], RICHARD WIRTH[2] and LUCIEN DATAS[3]

[1] LMTG, CNRS, Université de Toulouse, UPS (OMP), 14 Av. Edouard Belin, 31400 Toulouse, France
*Corresponding author, e-mail: seydoux@lmtg.obs-mip.fr
[2] GeoForschungsZentrum Potsdam, Telegrafenberg, Department 3.3-Experimental Geochemistry, 14473 Potsdam, Germany
[3] TEMSCAN – CIRIMAT, CNRS, Université de Toulouse, UPS, 118 route de Narbonne, 31400 Toulouse, France
[4] Present address: Laboratoire HydroSciences Montpellier, Université Montpellier 2, Case MSE, Place Eugène Bataillon, 34095 Montpellier Cedex 5, France

Abstract: Effects of infrared femtosecond laser ablation (800 nm, 60 fs, 5 Hz, 85 μJ/pulse, objective × 15) of a well-characterized monazite on its micro- and nano-structure were investigated. Craters were produced by single and multiple pulses (N = 10, 20, 50, 150 and 300) to follow the evolution of laser-induced damage in monazite using Scanning Electron Microscope (SEM), and Transmission Electron Microscope (TEM) coupled with Focused Ion Beam (FIB) sample preparation, in order to characterize this damage. Voids are observed within craters from the first pulse and cracks appear already after 10 pulses, at the sample surface; radial cracks are well-defined for 50 pulses, and become conchoidal after 150 pulses, indicating high-strain fields in the vicinity of craters. After the first pulse, the monazite lattice is highly strained to depths greater than ~1 μm with a spotty ring diffraction pattern demonstrating that the damaged monazite is a mosaic crystal. Under this area monazite is moderately strained over 6 μm in depth. Crack formation within the crystal is observed from the first pulse. Cracks formed at the surface and propagated over 2 μm into the crystal. Their number increased notably after 10 pulses, with some cracks propagating 8 μm into the crystal. Increasing lattice defects (mosaic crystal, twins) and fracture intensities demonstrate that a cumulative effect exists. Part of the energy carried by the laser is stored within the crystal and used in the formation of defects. This study highlights the intense damages that are created during a femtosecond laser ablation in monazite. Mechanical effects dominate thermal ones, limited to a thin layer (200 nm–1 pulse) of resolidified monazite, and are induced by high-pressure shock wave from plasma expansion.

Key-words: fs-laser ablation, laser induced damage, SEM-TEM-FIB, monazite, high pressure-shocked minerals.

Eur. J. Mineral.
2010, **22**, 235–244
Published online January 2010

Dominance of mechanical over thermally induced damage during femtosecond laser ablation of monazite

ANNE- MAGALI SEYDOUX-GUILLAUME[1,*], RÉMI FREYDIER[1,4], FRANCK POITRASSON[1], FRANÇOIS-XAVIER D'ABZAC[1], RICHARD WIRTH[2] and LUCIEN DATAS[3]

[1] LMTG, CNRS, Université de Toulouse, UPS (OMP), 14 Av. Edouard Belin, 31400 Toulouse, France
*Corresponding author, e-mail: seydoux@lmtg.obs-mip.fr
[2] GeoForschungsZentrum Potsdam, Telegrafenberg, Department 3.3-Experimental Geochemistry, 14473 Potsdam, Germany
[3] TEMSCAN – CIRIMAT, CNRS, Université de Toulouse, UPS, 118 route de Narbonne, 31400 Toulouse, France
[4] Present address: Laboratoire HydroSciences Montpellier, Université Montpellier 2, Case MSE, Place Eugène Bataillon, 34095 Montpellier Cedex 5, France

Abstract: Effects of infrared femtosecond laser ablation (800 nm, 60 fs, 5 Hz, 85 μJ/pulse, objective × 15) of a well-characterized monazite on its micro- and nano-structure were investigated. Craters were produced by single and multiple pulses (N = 10, 20, 50, 150 and 300) to follow the evolution of laser-induced damage in monazite using Scanning Electron Microscope (SEM), and Transmission Electron Microscope (TEM) coupled with Focused Ion Beam (FIB) sample preparation, in order to characterize this damage. Voids are observed within craters from the first pulse and cracks appear already after 10 pulses, at the sample surface; radial cracks are well-defined for 50 pulses, and become conchoidal after 150 pulses, indicating high-strain fields in the vicinity of craters. After the first pulse, the monazite lattice is highly strained to depths greater than ∼1 μm with a spotty ring diffraction pattern demonstrating that the damaged monazite is a mosaic crystal. Under this area monazite is moderately strained over 6 μm in depth. Crack formation within the crystal is observed from the first pulse. Cracks formed at the surface and propagated over 2 μm into the crystal. Their number increased notably after 10 pulses, with some cracks propagating 8 μm into the crystal. Increasing lattice defects (mosaic crystal, twins) and fracture intensities demonstrate that a cumulative effect exists. Part of the energy carried by the laser is stored within the crystal and used in the formation of defects. This study highlights the intense damages that are created during a femtosecond laser ablation in monazite. Mechanical effects dominate thermal ones, limited to a thin layer (200 nm–1 pulse) of resolidified monazite, and are induced by high-pressure shock wave from plasma expansion.

Key-words: fs-laser ablation, laser induced damage, SEM-TEM-FIB, monazite, high pressure-shocked minerals.

1. Introduction

Femtosecond laser ablation (Fs-LA) has been widely used for 20 years for various scientific purposes. In medicine Fs-LA can be used to ablate hard body parts such as calcified tissues (Neev *et al*., 1996; Liu & Niemz, 2007) and, in dentistry, caries may be treated by using Fs-LA (Niemz, 1998; Niemz *et al*., 2004). In materials science the potential of Fs-LA is used and is studied for applications in the semi-conductor industry related to the precise micro-machining of silicon (Bonse *et al*., 2002; Coyne *et al*., 2005), indium phosphide (Bonse *et al*., 2001; Borowiec *et al*., 2003a, 2004; Couillard *et al*., 2007) and lithium niobiate (Stach *et al*., 2003). In the geosciences, laser ablation coupled with ICP-MS (Inductively Coupled Plasma-Mass Spectrometry) is widely used for the *in situ* determination of element concentrations and isotopic ratios in minerals. In phases such as zircon or monazite, this technique allows high spatial resolution, *i.e*. down to 4–5 μm craters, for U-Th-Pb dating (Poitrasson *et al*., 2000; Paquette & Tiepolo, 2007). In this application, a critical aspect is elemental and isotopic fractionation that must be maintained as low as possible. Recent studies showed that fs lasers (Poitrasson *et al*., 2003; Horn & von Blanckenburg, 2007; Freydier *et al*., 2008) reduce elemental fractionation compared to nanosecond (ns) laser ablation. This is mostly due to the fact that, in principle, ultra short pulse laser ablation results in a significantly reduced heat-affected zone (Le Harzic *et al*., 2002). This is because the energy is imparted to the sample over a very short period of time (∼60 fs) and the ablated material is completely removed before a significant amount of the energy can be spread to the surrounding region of the sample. The energy is imparted within an average time of 10^{-15} s, which is very short compared to the mean heat diffusion time constant, which is in the order of 10^{-12} to 10^{-11} s (von

DOI: 10.1127/0935-1221/2010/0022-2001
0935-1221/10/0022-2001 $ 4.50

der Linde *et al.*, 1997; von der Linde & Sokolowski-Tinten, 2000; Laville *et al.*, 2002; Lorazo *et al.*, 2003).

In a review on Fs-laser ablation coupled with ICP-MS, Fernandez *et al.* (2007) presented a comparison between laser–matter interaction with nanosecond and femtosecond pulses (their Fig. 1). They suggested that, in addition to there being no heat-affected zone, there is no damage, no occurrence of cracks or shock-wave effects in material analyzed in the femtosecond laser ablation regime. However, numerous studies have demonstrated the presence of damage effects created by Fs-laser ablation within different materials. Borowiec *et al.* (2004) observed a high density of defects (microtwins and dense network of dislocations) extending over a few micrometres in depth in InP (800 nm, 130 fs, 2 J/cm^2) and Couillard *et al.* (2007) described a similar result for this phase (2050 nm, 100 fs, 0.8 J/cm^2); Borowiec *et al.* (2003a) imaged the residual strain field resulting from laser ablation in femtosecond (800 nm, 130 fs, 2 J/cm^2) and nanosecond regimes and show that areas under tension in femtosecond ablated samples are in compression in the nanosecond ablated samples and vice versa. Stach *et al.* (2003) observed defect-rich regions at the focal point of the laser pulse (800 nm, 300 fs, 123 J/cm^2) in $LiNbO_3$, interpreted to be associated with shock-wave propagation, and Coyne *et al.* (2005) observed the presence of mechanical damage at the base of the hole in silicon (775 nm, 150 fs, 11 J/cm^2). Furthermore, two other studies have clearly demonstrated elevated pressure induced by Fs-laser ablation: Ma *et al.* (2007) transformed rutile into anatase by Fs-laser ablation (800 nm, 120 fs, 191 J/cm^2) and Sano *et al.* (2005) used Fs-laser ablation (800 nm, 120 fs, 12 J/cm^2) to synthesize a high-pressure phase of iron (ε) and suggested this as method for synthesis of high-pressure phases. All these studies performed in different materials showed that the mechanical damage effects by Fs-laser ablation should not be ignored. Finally, it is important to recognise that with such a pronounced mechanical effect, large particles (micrometre sized) are likely to be created. This presents a problem for elemental and isotopic microanalysis as incomplete LA-ICP-MS ionization of such large-diameter aerosols (Kuhn *et al.*, 2004) will generate chemical and isotopic fractionation (Horn *et al.*, 2007). It is therefore essential to carefully study these effects on structures of materials for analytical or high-pressure mineral physics applications.

This initial study investigates the micro- to nano-structural changes induced by Fs-laser ablation (800 nm, 60 fs) in monazite by using electron microscopic methods [Scanning Electron Microscope (SEM) and Transmission Electron Microscope (TEM) coupled with Focused Ion Beam (FIB)]. Comparable studies dealing with Fs-laser ablation induced damages in materials, and in particular in geoscience, are not so widespread. As mentioned above, most of the studies concern semi conductors (Si, InP, $LiNbO_3$, AlGaN/GaN) and, to our knowledge, there are very few such studies on minerals. Only Gorelik *et al.* (2003) present a brief report of a TEM study where the laser was focused inside the quartz below the surface. Ma *et al.* (2007) followed the phase transformation from rutile into anatase induced by Fs-laser ablation by using micro-Raman spectrometry. Finally, Kosler *et al.* (2005) observed thermal decomposition of zircon with TEM in sample prepared with FIB perpendicularly to the surface and adjacent to the laser pit ablated with a nanosecond laser.

The aim of the present work has been to characterize the effects induced by Fs-laser ablation on micro-nano-structures of monazite. Single and multiple pulses Fs-laser ablation were conducted on monazite crystals and resulting craters were observed using SEM and TEM coupled with FIB sample preparation. Results demonstrate that mechanical effects cannot be neglected during fs-laser and dominate thermal ones.

2. Experimental procedure

2.1. Laser ablation

Pulses were obtained with a commercial femtosecond Ti:sapphire laser system (Pulsar 10, Amplitude Technologies, Evry, France) based on the chirped-pulse amplification (CPA) technique (for details see Freydier *et al.*, 2008). The laser operates at a centre wavelength of 800 nm, 5 Hz repetition rate and pulse duration of 60 fs. The laser beam was focused on the sample surface by a 15 × Cassegrin-type reflective objective, which induced a loss of energy; the energy arriving at the sample surface is therefore reduced to 17 % from the initial energy of laser (500 μJ/pulse, injected in the 15 × objective), *i.e.* 85 μJ/pulse. The diameter of the ablation crater is ∼30 μm (measured by SEM); this measurement allows a calculation of average laser fluence of ∼12 J/cm^2. This value is significantly above the threshold fluence, measured experimentally at ∼1 J/cm^2 in monazite (d'Abzac *et al.*, in press) with the method seen in Bonse *et al.* (2001); for this value possible LA-ICP-MS analyses would be optimized (Freydier *et al.*, 2008). Craters were produced by single and multiple pulses (10, 20, 50, 150 and 300) irradiations in order to follow the evolution of the crater geometry and the micro-nanostructure modifications induced (*e.g.*, bubbles, cracks, crystallinity). Randomly oriented monazite crystals (2–4 mm large), mounted in epoxy and polished, were placed in an ablation cell. Ablated particles were transferred from the cell via He carrier gas flowing through the cell at a fixed flow rate (He, 0.4–0.5 L/min). In order to observe the deposited ejectas on the sample surface single-pulse experiment was carried out without the use of a carrier gas (Fig. 1A-SEM and 2A-TEM).

2.2. Sample

The Moacyr monazite sample (Seydoux-Guillaume *et al.*, 2002a, 2002b, 2004) was used for this study. This standard monazite is very well characterized by a large variety of techniques such as SEM, electron microprobe analysis

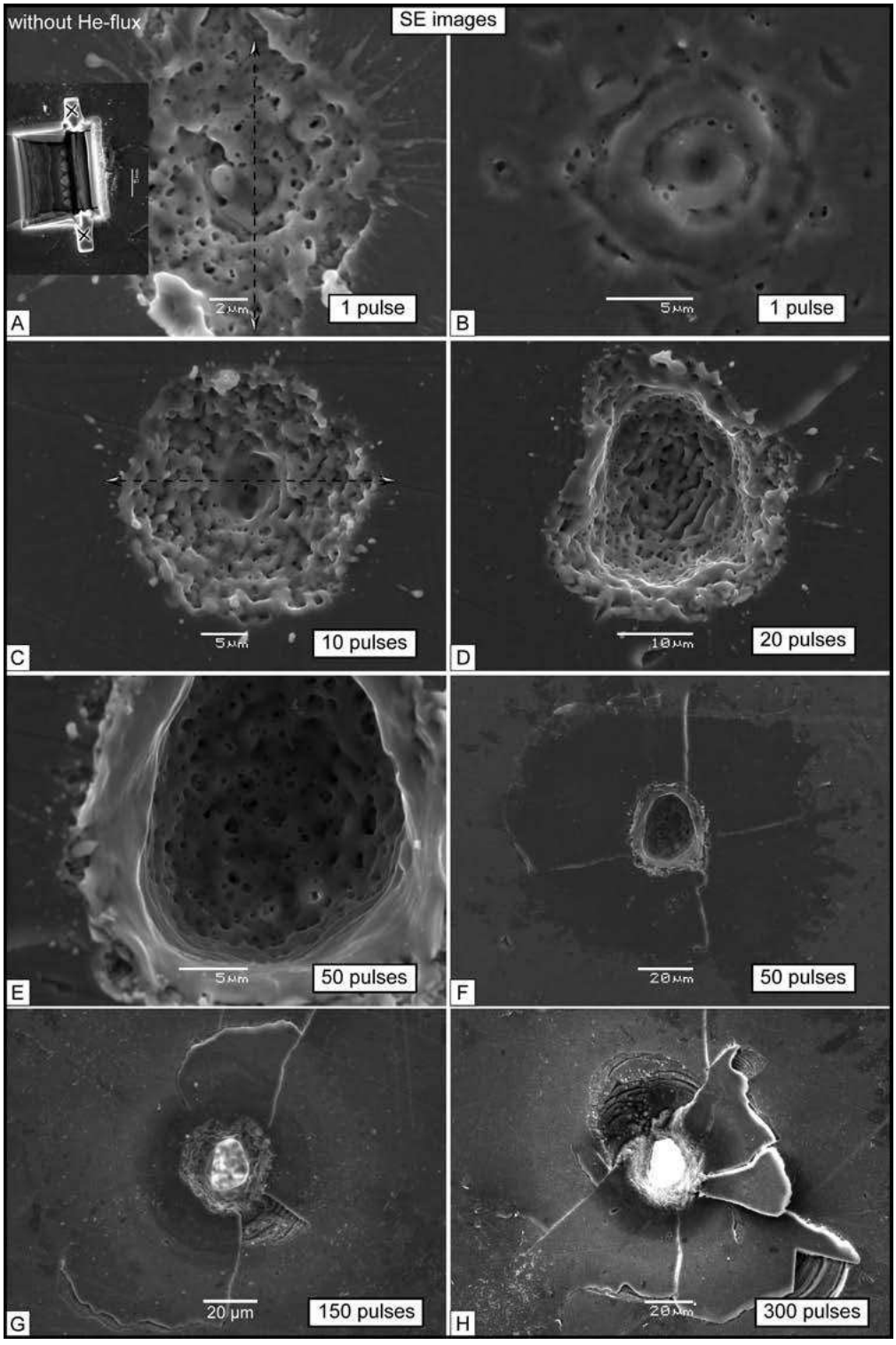

Fig. 1. Scanning electron microscope (SEM) images in secondary-electron mode (SE) showing morphologies of craters ablated with fs-laser for various numbers of pulses (1–300 pulses). In particular the diameter evolution (from 14 to 34 µm), presence of radial cracks (D–F) intense fracturation (G–H) and voids (A–E) can be noticed. The difference between A and B comes from the absence (A) or the presence (B) of a helium-flux during ablation; from that follows the presence in high quantity (A) or limited amount (B) of ejectas on the surface of the sample. Two transmission electron microscope (TEM) foils were prepared by focused-ion-beam (FIB) milling across crater shown in A (Fig. 2A) and in C (Fig. 2I). Inset in A corresponds to the trace within crater after FIB milling. See text for details.

(EPMA), TEM, Raman, cathodoluminescence (CL), X-ray diffraction (RXD), and Isotope Dilution Thermo Ionization Mass Spectrometry (ID-TIMS) (Nasdala *et al.*, 2002; Seydoux-Guillaume *et al.*, 2002a, 2002b, 2004; Freydier *et al.*, 2008). All these techniques have demonstrated the chemical homogeneity of this monocrystal, and its low amount of irradiation damage, for which the sole evidence is lattice distortion. This background

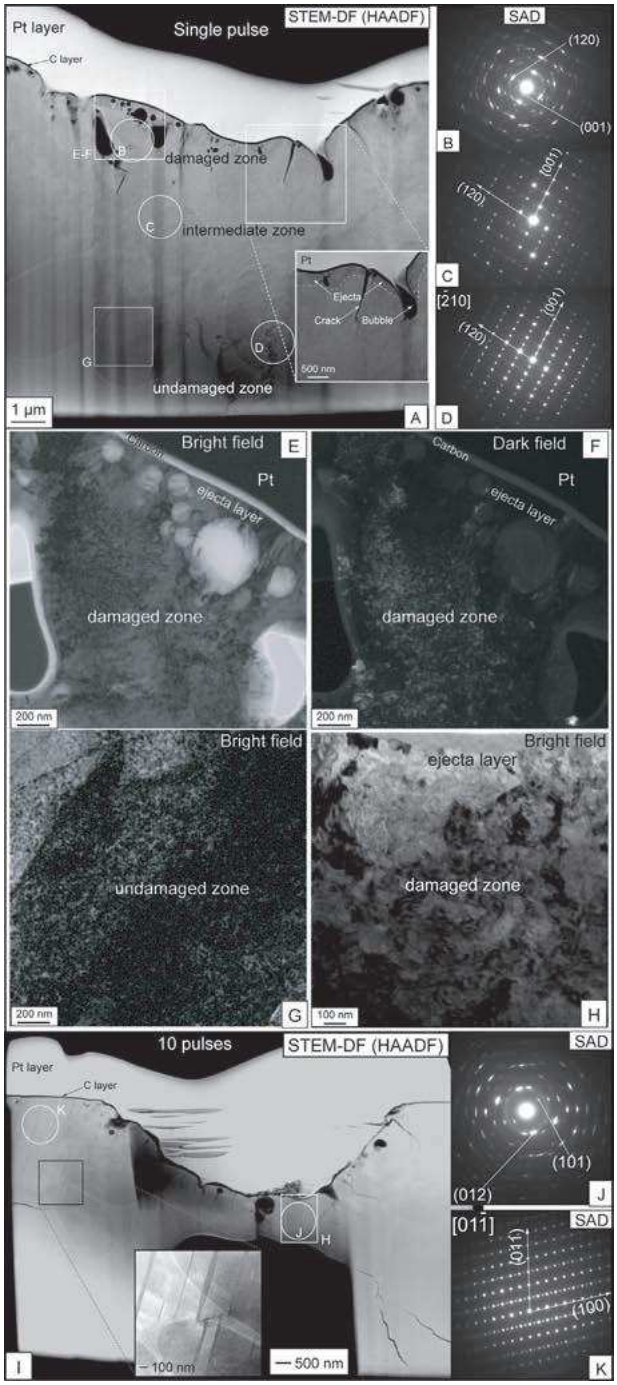

Fig. 2. TEM observations realized on two FIB foils cut across a one-pulse crater (shown in Fig. 1A) and a 10-pulse crater (shown in Fig. 1C). The long straight darker traces starting at holes and proceeding downward are an artefact from FIB preparation called ''curtaining effect'' (Fig. 2A and I). (A–G) TEM observations from foil cut across one-pulse crater. (A) Scanning TEM (STEM) image of a part of the FIB-foil cut across a single-pulse crater acquired with a high-angle annular dark-field (HAADF) detector showing four different zones: (i) resolidified layer (ejecta) composed of nanocrystalline material and bubbles, (ii) damaged zone with a corresponding selected-area diffraction (SAD) pattern (B) of a mosaic crystal, (iii) intermediate zone with diffuse contrasts (corresponding SAD pattern in C), and (iv) undamaged zone (corresponding SAD pattern in D). All dark contrast corresponds to holes (or light elements, *e.g.*, C-layer on the surface sample), and bright contrast represents heavy elements (*e.g.*, protective Pt layer deposited on the sample during the FIB-milling process). (E–F) TEM bright-field (BF) image (E) and associated dark-field (DF) image (F) from an intensively strained zone located in A. (G) TEM-BF image from undamaged zone; mottled diffraction contrasts correspond to residual strains within the lattice induced by natural irradiation damage typical for natural monazite. (H–K) TEM observation from foil cut across 10-pulse crater. (I) STEM image of a part of the FIB-foil, acquired with a HAADF; the foil was broken in the middle during FIB milling and thus a part of the foil in the axis of the laser beam and below 2 µm depth is missing, and the centre of the foil is thinner. Note that modifications induced by the accumulation of 10 pulses are the same as for one single pulse: presence of bubbles, cracks and nanocrystalline monazite in the upper part (I), damaged monazite with a mosaic crystal structure below (BF image and associated SAD pattern J); however, the mechanical effects are several orders of magnitude higher, as demonstrated by cracks propagated up to 8 µm deep, and the presence of twins (I). Note that, in contrast, the number or size of the bubbles (thermal effect) remains constant (even reduced).

characterisation was done before investigating laser-ablation effects on the sample structure. Two main reasons were at the origin of the choice of monazite for this study. Firstly, monazite is, after zircon, the most often analyzed mineral by using LA-ICP-MS for U-Pb dating. Secondly, a more indirect reason is linked to the ability of monazite to heal its irradiation damage at low temperature (Meldrum *et al*., 1997). This last point makes it an efficient tracer of thermal occurrences within the crystal.

2.3. Electron microscopy (SEM-FIB/TEM)

The SEM images were acquired using the JEOL 6360 equipped with a Sahara detector from PGT at LMTG-Toulouse.

The TEM samples were prepared using the FIB technique that allows cutting site-specific TEM foils, ~15–20 μm by 10–15 μm, and ~100 nm thick (for technical details, see Wirth, 2004) perpendicular to the surface of the sample and across the laser ablation craters (Fig. 1 and 2). The samples, coated with a protective Pt layer, were milled using gallium ions accelerated to 30 keV. After milling, foils were cut free, lifted out and placed on a holey carbon coated grid for TEM observations. The site-specific specimens were prepared with the FEI FIB200 instrument at the GeoForschungsZentrum (GFZ)-Potsdam. One TEM-foil was cut across a crater formed after single pulse irradiation (Fig. 1A and 2A) in order to observe structures modifications under the laser beam and to determine characteristic depths. A second foil was cut across a crater formed after 10 pulses (Fig. 1C and 2I) in order to observe the effect of cumulative pulses on the sample structure.

The TEM studies were carried out both with a JEOL JEM 2010 operating at 200 kV, equipped with a LaB_6 filament as electron source, and installed at the TEMSCAN lab in Toulouse, and a FEI Tecnai$^{TM}G^2$ F20 X-Twin, operating at 200 kV, equipped with a FEG electron source, a high-angle annular dark-field (HAADF) detector, and an EDX (Energy dispersive X-ray) analyzer system from EDAX, and installed at GFZ-Potsdam.

3. Results

3.1. Scanning electron microscopy

The craters are lightly elliptical, due to a little tilting of the sample against the orthogonal path of the laser beam. Surface diameters increase from 14–15 μm for the single pulse crater (Fig. 1A and B) up to 30–34 μm for 150 and 300 pulses (Fig. 1G and H).

The single-pulse crater shows two rings (the ''Airy ring'': Fig. 1B), corresponding to diffraction interferences from the laser beam associated with a heterogeneous energy distribution (80 % in the centre) in the laser beam. Furthermore, voids were observed within the crater: only a few, when ejectas were transported by He-flux (Fig. 1B), and more when He-flux was absent (Fig. 1A). This indicates that voids are more concentrated in ablated (ejectas) material and limited within the sample.

For more than one pulse, the morphology of the craters is ''ripple''-like (see the 20 pulses crater, Fig. 1D), but the ripples are not as regular as those in craters described in the literature (Bonse *et al*., 2002; Couillard *et al*., 2007; Guillermin *et al*., 2007; Varlamova *et al*., 2007). At greater than 50 pulses, crater bottoms show a ''bubbled'' morphology (Fig. 1E). Amongst the most intense modifications of the samples relate to increased density of fracturing with the pulse number. Monazite shows radial cracks on the surface after 20 pulses (Fig. 1D), and intense fracturing at greater than 50 pulses (Fig. 1F), up to conchoidal breaking from 150 pulses (Fig. 1G and H). This suggests high strain fields in the vicinity of craters. Ablated particles are ejected and re-deposited on the sample surface when no He flux is used (Fig. 1A). Even when He flux is efficient, a broad ring-shaped layer (100–180 μm in radius) of ejectas forms around the crater after 50 pulses (Fig. 1F–H).

3.2. Focused ion beam/transmission electron microscope

The FIB foils were prepared perpendicular to the sample surface on single pulse (Fig. 1A) and 10 pulses (Fig. 1C) craters.

3.2.1. Single-pulse crater

Figure 2A shows part of the FIB-foil cut across a 2.1 μm deep, single-pulse crater (Fig. 1A). Images in this STEM mode acquired with a high-angle annular dark-field (HAADF) detector contain predominantly information on chemical composition of the sample (atomic number Z). Moreover, HAADF signals strongly depend on the thickness of the sample: thinner areas of the foil with the same composition appear darker (*e.g*., Fig. 2I; middle of the foil). This is why uniform foil thickness is essential to facilitate interpretation, and is made possible by cutting the sample with FIB (Wirth, 2004). Given a uniform thickness foil it is valid to conclude that all black zones in the image corresponds to holes (or light elements, *e.g*., C-layer on the surface sample), and bright zones represent heavy elements (*e.g*., protective Pt layer deposited on the sample during the FIB-milling process). Moreover, ''diffuse or milky contrasts'' in the intermediate zone (Fig. 2A) are most likely due to different crystallographic orientations of the area (confirmed by selected area diffraction pattern, Fig. 2C).

Four different zones, more or less clearly delimited, can be distinguished from the surface of the sample (top of Fig. 2A) under the Pt-layer, downwards the deeper portions of the crystal. The first one is an ejecta layer, ~200–300 nm thick, composed of nanocrystalline (50–100 nm) material (observe diffraction contrasts in the Bright Field image, Fig. 2E) and bubbles (Fig. 2A and E); the latter were already observable using SEM (Fig. 1A). The particularity of this zone is that the

nanocrystalline monazite (Fig. 2E and F) does not show the mottled diffraction contrasts that are characteristic of natural monazites (Seydoux-Guillaume *et al.*, 2002a, 2003, 2004, 2007). This implies that the material initially composing this layer was completely transformed during ablation. Cracks are dispersed within this layer and propagate into the second zone, which corresponds to the damaged zone (Fig. 2A, B, E and F). This 1 μm-thick zone shows the structure of a mosaic crystal (Fig. 2E and F) as demonstrated by the corresponding electron diffraction pattern (SAD), whose spots show streaking into arcs (Fig. 2B), consistent with a spread in the grain orientation. TEM-Bright Field (BF, Fig. 2E) and Dark Field (DF, Fig. 2F) images confirmed that the zone is intensely strained, in particular, contrasts revealed by DF image (Fig. 2F) indicate that large number of small domains are slightly tilted with respect to each other, *i.e.* the lattice is distorted. These observations are consistent with a response of monazite to high shock pressure. Furthermore, this zone does not contain any amorphous material; the monazite is still crystalline. Below this damaged zone and up to 7 μm deep there is an intermediate (or less damaged) zone (''diffuse or milky contrasts''), where the monazite crystal is less distorted (no spotty rings on the SAD pattern, Fig. 2C), but still strained enough so that the diffraction pattern lacks spots associated with specific crystallographic directions [*e.g.*, (001), (003) directions] and shows the appearance of diffraction spots other than those seen in undistorted monazite (Fig. 2D). Finally, beyond depths of 7–8 μm the monazite is undamaged and corresponds to the original crystal not affected by laser beam. The SAD pattern corresponds to a well-crystallized undistorted monazite single crystal. The unique evidence of a defective lattice in this zone is revealed by mottled diffraction contrasts visible in the BF mode (Fig. 2G) that correspond to residual strains within the lattice induced by natural irradiation damage (Seydoux-Guillaume *et al.*, 2002a, 2004).

Finally, no significant chemical variation, *i.e.* higher than 1–2 wt% variation, was observed in any of these zones; all analyses correspond approximately (within the TEM-EDX precision, *i.e.* 5–10 wt% depending on the concentration) to the initial Moacyr monazite composition (Seydoux-Guillaume *et al.*, 2002b).

3.2.2. The 10-pulse crater

This crater is 3.2 μm deep. The foil was broken in the middle (Fig. 2I) during FIB milling and thus a part of the foil in the axis of the laser beam and below 2 μm depth is missing. Furthermore, the centre (appears darker in Fig. 2I) of the foil is thinner so that direct comparison of TEM contrasts (Fig. 2I) between the rim and the centre of the foil cannot be made. Modifications induced by the accumulation of 10 pulses are the same as for one single pulse: presence of bubbles, cracks and nanocrystalline monazite in the upper part (Fig. 2I), and damaged monazite with a mosaic crystal structure at deeper levels (Fig. 2J and H). However, the mechanical effects that induced cracks are several orders of magnitude greater: (i) more cracks are created by ablation and some have propagated down to the lower edge (~8 μm deep) of the TEM foil (Fig. 2I) monazite twins are induced by laser ablation (Fig. 2I and K) – the (100) twin visible on Fig. 2I, with lenticular form, corresponds to the most frequent twins found in monazite (Hay & Marshall, 2003). These twins are only present on the left side of the crater (Fig. 2I), whereas cracks are more penetrative on the other side of the crater. In contrast to the number of cracks that increase with increasing pulse number (mechanical effect), the number or size of the bubbles (thermal effect?) or cavitation remains constant. Because the foil was broken during FIB-milling, it is not possible to evaluate the full depth to which the laser beam affected the monazite crystal. However, on the rim of the crater, monazite is still monocrystalline as shown by SAD pattern (Fig. 2K).

4. Discussion

4.1. Evolution of the craters morphology: the cumulative effect

Crater diameters change significantly during the first 20 laser pulses (from 14 to 26 μm). For pulse numbers between 20 and 50, diameters increase from 26 to 30 μm and remain constant up to 50 pulses at a value of 35 μm. Moreover, depth measurements of single and 10-pulse craters with FIB foils demonstrate that monazite ablation rate is not linear; it is very high from the first pulse (2 μm) but after 10 pulses, the crater is only 3.2 μm deep, hence with a 0.32 μm/pulse ablation rate. Because we were only able to measure these two craters, it is difficult to extrapolate these measurements to subsequent pulses. However, it is interesting to consider two phenomena that could influence the ablation rate. The first one concerns the beam focus on the sample. When the second pulse is hitting the sample, the beam is still focused on the primary sample surface (2 μm above the material). The resulting defocused laser beam will be less efficient to ablate the material, because of a lower effective fluence. However, up to this point the efficiency of this effect has not been proven. A second and more important phenomenon concerns the modifications of physical properties of the ablated monazite induced after the first pulse. As shown above, the structure of ablated monazite is modified after the first pulse. Monazite is slightly distorted (up to 7 μm in depth), and it has the features of a mosaic crystal down to 1 μm deep (Fig. 2A–D), and fractured, with cracks propagating down to 2 μm depths in the crystal. This means that only a part of the energy contained in the first pulse was used for ablation; the rest of the energy was deposited and accumulated within the monazite crystal and is responsible for the defect creation within it, *i.e.* deformation of the monazite into a so called mosaic crystal. Subsequent pulses will therefore interact with a modified monazite. One can suggest that this

modified monazite should be ablated in the same way as an unaffected one or perhaps more easily ablated, unless the energy deposited through subsequent pulses within the sample is released, *e.g.* through cracks, or used to create other defects. This is precisely what happens after 10 pulses (Fig. 2I): intense fracturing (cracks propagated over 8 μm) and twin formation are observed within the monazite crystal. We therefore infer that a large fraction of the laser energy that was received by the monazite was used to create these features rather than for efficient ablation. This cumulative effect was explained by Yong *et al.* (1988) via an incubation mechanism, and was, in their work, related to energy accumulation via plastic stress-strain of the crystalline metals. For other authors and other materials, the possibility of energy consumption by phase transformation, such as amorphization/re-cystallization or chemical changes also has been proposed (Bonse *et al.*, 2001; Borowiec *et al.*, 2004; Couillard *et al.*, 2007).

4.2. Dominance of mechanical over thermally induced damage

Femtosecond laser ablation is of high interest essentially because of its limited heat-affected zone (Le Harzic *et al.*, 2002). This is a critical factor for elemental fractionations, which should be limited in comparison to nanosecond laser ablation when coupling femtosecond laser ablation with ICP-MS (Poitrasson *et al.*, 2003). In this section we will discuss these effects and also evaluate other effects, such as the mechanical processes observed.

4.2.1. Thermal effects: presence of resolidified material, i.e. *ejecta*

On the basis of SEM images (Fig. 1), one would expect the ejecta (resolidified material on the sample surface) to be composed of molten material, *i.e.* to be amorphous material. However, our TEM observations reveal that ejecta consist of nanocrystals embedded together with bubbles (Fig. 2A, E and F). Nanocrystalline (∼50 nm) ejecta were already described in Borowiec *et al.* (2003b) in InP and GaAs materials, for energies between 18 and 52 nJ, from the first pulse. As described above, these monazite nanocrystals do not show mottled diffraction contrasts characteristic for irradiation damage in natural monazite (Seydoux-Guillaume *et al.*, 2002a, 2003, 2004, 2007). This implies a complete transformation of this layer during ablation. From literature it is known that monazite completely heals its irradiation damage for temperature higher than 900 °C (Seydoux-Guillaume *et al.*, 2002b), nevertheless for longer duration than those occurring during a femtosecond laser ablation (Ben-Yakar *et al.*, 2007). As example, Ladieu *et al.* (2002) report direct local thermal measurements carried out on a quartz sample at the millisecond scale and measured a temperature ∼3000°C in the vicinity (50 μm) of the crater. Annealing of irradiation damage and the presence of bubbles in the layer suggest a thermal effect occurring during fs ablation. Lorazo *et al.* (2003) used Monte Carlo and molecular-dynamic modelling of 500 fs-laser ablation of silicon substrate, to demonstrate that 1 ps after the first pulse, a hot (∼8000 K) and highly pressurized (∼10 GPa) liquid layer has formed at the surface by isochoric heating; the incoming laser energy being transferred to the ions in 1 ps. The pressure is then released via mechanical and adiabatic expansion and therefore without heating the substrate under the ''liquid layer''. This rapid expansion causes material ejection, *i.e.* ablation occurs, eventually with void nucleation (=gas bubbles). Ben Yakar *et al.* (2007), in an experimental study on borosilicate glass ablated using single IR femtosecond laser pulses, demonstrate that a small portion of the incoming energy (from the high-pressure, high-temperature plasma) is deposited on the sample surface and used to form a thin melted zone below the surface. Ladieu *et al.* (2002) measured that ∼8 % of the incoming energy was thermalized and transmitted to the undamaged part of a quartz crystal irradiated with a 100 fs laser pulse for fluence very close to the threshold fluence (1.2 times higher). These results are consistent with our study; some of the ablated material (ejecta) resolidified on the monazite surface was also heated at very high temperature [monazite melts at ∼2000 °C (Boatner, 2002) and vaporizes most probably above 3000 °C; temperature in agreement with those measured by Ladieu *et al.* (2002) in quartz] but not the monazite substrate below, because irradiation damage within monazite was not healed except for within this ejecta layer. This is evidence for non-thermal diffusion within the crystal, because it is known that irradiation damage is healed at low temperature in monazite (Meldrum *et al.*, 1997, 1998; Seydoux-Guillaume *et al.*, 2002a). After expulsion, monazite re-crystallizes rapidly but is not quenched enough to stay amorphous; monazite re-crystallizes as nano-crystals. In contrast Jia *et al.* (2004) observed a rapid solidification of molten silicon after femtosecond laser ablation (150 fs) of a silicon single crystal, resulting in the formation of an amorphous Si layer. Finally, in contrast to other studies on fs-laser ablation of InP (Borowiec *et al.*, 2004; Couillard *et al.*, 2007) or $LiNbO_3$ (Stach *et al.*, 2003), many bubbles were observed in our samples that are comparable to silicon fs-ablation (Bonse *et al.*, 2002) and demonstrate vaporization of material and void nucleation.

4.2.2. Mechanical effects: shock wave propagation

Some studies from the literature investigated the plasma pressure induced by a femtosecond laser ablation. Ben-Yakar *et al.* (2007) completed the studies from Perry *et al.* (1999), Choi & Grigoropoulos (2002) and Vidal *et al.* (2001) and precised that femtosecond laser generated plasmas exhibit very high pressures (millions of atmosphere) in the first tens of picoseconds. As the plasma expands (mainly vertically), the pressure decreases rapidly to several tens of atmosphere within a few tens of nanosecond. Sokolowski-Tinten *et al.* (1998) and Lorazo *et al.* (2003) have also estimated the pressure during a femtosecond laser ablation to be in the range of tens of GPa.

In contrast to thermal effects limited to the resolidified layer, mechanical traces seem to dominate within the crystal substrate: SEM and TEM results demonstrate the presence of intense fracturing, with cracks propagating far into the crystal, a highly strained lattice resulting in a mosaic crystal, and even the presence of twins within the monazite ablated with 10 pulses. All of these observations clearly demonstrate the extent of mechanical effects due to shock-wave propagation during femtosecond laser ablation. Observation of these defects is not restricted to this study – similar defects have been observed in numerous studies on metals or alloys (Borowiec *et al.*, 2003a, 2004; Coyne *et al.*, 2005; Couillard *et al.*, 2007). However, the presence of cracks within the monazite crystal can be explained by the low hardness (Moh hardness of 5.5) of monazite; the intense fracturing is not widespread in other materials like metals, alloys and even quartz, whereas the presence of twins, dislocation networks or strained lattice has been widely reported in numerous studies (Borowiec *et al.*, 2003a, 2004; Gorelik *et al.*, 2003; Coyne *et al.*, 2005; Couillard *et al.*, 2007).

In our study, the monazite lattice responds to shock-wave propagation within the first pulse (Fig. 2A, B, E and F) by accumulating strain within the lattice, which appears as a mosaic crystal. In contrast, Couillard *et al.* (2007) detected extended defects only for multiple-pulse craters; a difference that could be explained by a lower fluence (0.8 J/cm^2). Stach *et al.* (2003) already observed high dislocation densities for the first pulse at higher fluence (123 J/cm^2). However, such comparisons of different femtosecond laser ablation studies of various materials are difficult to evaluate. This is because the majority of investigations were conducted on metals, which have properties very different from those of monazite, and also because femtosecond laser ablation parameters, notably fluence, are also very different and often poorly defined, *e.g.* estimates based on the use of crater size instead of focal spot diameter for Gaussian beams, (Freydier et al., 2008; d'Abzac et al. (in press)).

Finally, taking into account pressure values from literature (see above), we found interesting to make a parallel (only qualitative) between the plasma-pressure-induced damage in the monazite crystal under the craters produced after femtosecond laser ablation, and the pressure-induced damage in minerals submitted to high-pressure shock (experimentally or naturally shocked minerals, *e.g.*, impact rocks). Bell (2007) exposed siderite to 49 GPa experimental shock and revealed, by TEM, the development of extensively strained submicrometre domains of siderite. The crystal lattice was so distorted that mottled contrasts were observed in the bright-field TEM image. Dougherty *et al.* (2007) performed a 14 GPa gas gun shock loading experiment on 1018-steel. They also observed spotty ring patterns under the TEM, correlating with a highly strained lattice. Leroux *et al.* (2008) investigated micro-craters produced by hypervelocity impacts of comet dust particles on the aluminium foil of the Stardust collector and show that particles (olivine) were subjected to strong shock deformation (60–70 GPa). All these similarities with our observations on monazite, even though only qualitative, demonstrate that pressure effects of femtosecond laser ablation are very important and can not be neglected, and that mechanisms operating in fs-laser ablation are very close to those operating in very high-pressure studies. This was already viewed by Langenhorst *et al.* (1999), who used nanosecond laser pulse to generate shock defects in minerals. In this study, we show that a femtosecond laser pulse would be even more appropriate for this application given its stronger mechanical effect.

5. Conclusions

Using microscopic (SEM) and nanometric (FIB/TEM) studies of the monazite structure, we have demonstrated that intense damage is created during femtosecond laser ablation of monazite. Mechanical effects, such as an intensively strained lattice leading to a mosaic crystal, twin formation, and crack formation and propagation within the crystal, are induced by a high-pressure (tens of GPa) shock wave associated with the femtosecond laser pulse, and largely dominate thermal effects, which are limited to a thin layer (200 nm) of resolidified nanocrystalline monazite. The mechanical defects are created because of the storage (cumulative effect) within the crystal of a part of the energy used for ablation.

Our results are in agreement with the previous suggestions that ultra-short laser pulses like fs ablate the matter so rapidly (energy deposited within a time scale of 10^{-15} s) that the process takes place without significant thermal diffusion (mean heat diffusion time on the order of 10^{-12} until 10^{-11} s) (von der Linde *et al.*, 1997; von der Linde & Sokolowski-Tinten, 2000; Laville *et al.*, 2002; Le Harzic *et al.*, 2002). Most of the incoming energy is used by the expanding plasma to move into the ambient gas whereas a small portion remains in the ablated sample as thermal energy (Ben-Yakar *et al.*, 2007).

To conclude and as perspective for this study it is now essential to evaluate implications of such high density defect formation for laser ablation-ICP-MS measurements. In particular, the fundamental question for ICP-MS measurement concerns chemical fractionation. Since most of the energy goes into producing mechanical defects in the fs laser ablation regime, the next question is to understand the cause of the remaining small chemical fractionation still observed in fs LA-ICP-MS (Poitrasson *et al.*, 2003; Freydier *et al.*, 2008). A similar issue lies with isotopic fractionation (Ikehata *et al.*, 2008) that is still observed in IR fs LA-MC-ICP-MS. For example, a potential direct effect due to a high mechanical damage of the sample may be the production of large (micrometre sized) particles that the ICP torch may not be able to completely ionize. As a consequence, chemical and isotopic fractionation may be generated (Guillong & Günther, 2002; Jackson & Günther, 2003). Analytical TEM was not adapted to detect possible elemental fractionation (*e.g.*, U and Pb were not detectable) within the resolidified and damage areas; therefore, other analytical methods must be used. The more adapted one will be the NanoSIMS (Nano

Secondary Ion Mass Spectrometry), because we will need to obtain analyses directly from FIB foils cut within craters produced by the fs laser. Doing NanoSIMS in such FIB foils will allow us to evaluate if the very localized heating and melting (observed within the first micrometre in the present study), or if the analytical artefacts observed (Poitrasson *et al.*, 2003; Freydier *et al.*, 2008) are just related to particle size effects. This is a fundamental question to address in order to perform precise and accurate dating with a fs-laser ablation ICP-MS in monazite and other minerals.

Other parameters, like the influence of energy and pulse width on ICP-MS signal of monazite correlated with characterization of ablated particles and structure modifications within the ablated craters (d'Abzac *et al.*, in press) are in progress. Two comparisons will also be tested, that could have an influence on both structure and ICP-MS signal: the wavelength (UV *vs.* IR) and the pulse width (nanosecond *vs.* femtosecond). Once these mechanisms will be understood, we will be able to link them to the elemental and/or isotopic fractionation observed, one of the most critical parameters for successful analytical geochemistry, and develop a predictive model to improve such microanalysis.

Acknowledgements: The FIB and some of the TEM analyses have been done thanks to the financial support for travels to Potsdam from PROCOPE (2005–2006) N°09638ZB. The authors want to thank Simon Harley for checking both the scientific and the English content of this paper. R. Ewing, an anonymous reviewer and Associate Editor K.J. Livi are acknowledged for their work.

References

Bell, M.S. (2007): Experimental shock decomposition of siderite and the origin of magnetite in Martian meteorite ALH 84001. *Meteorit. Planet. Sci.*, **42**, 935–949.

Ben-Yakar, A., Harkin, A., Ashmore, J., Byer, R.L., Stone, H.A. (2007): Thermal and fluid processes of a thin melt zone during femtosecond laser ablation of glass: the formation of rims by single laser pulses. *J. Phys. D Appl. Phys.*, **40**, 1447–1459.

Boatner, L.A. (2002): Synthesis, structure, and properties of monazite, pretulite, and xenotime. *in* ''Reviews in Mineralogy and Geochemistry'', P.H. Ribbe, ed. Mineralogical Society of America, Washington, DC, 87–121.

Bonse, J., Wrobel, J.M., Kruger, J., Kautek, W. (2001): Ultrashort-pulse laser ablation of indium phosphide in air. *Appl. Phys. A Mater. Sci. Process.*, **72**, 89–94.

Bonse, J., Baudach, S., Kruger, J., Kautek, W., Lenzner, M. (2002): Femtosecond laser ablation of silicon-modification thresholds and morphology. *Appl. Phys. A Mater. Sci. Process.*, **74**, 19–25.

Borowiec, A., Bruce, D.M., Cassidy, D.T., Haugen, H.K. (2003a): Imaging the strain fields resulting from laser micromachining of semiconductors. *Appl. Phys. Lett.*, **83**, 225–227.

Borowiec, A., MacKenzie, M., Weatherly, G.C., Haugen, H.K. (2003b): Femtosecond laser pulse ablation of GaAs and InP: studies utilizing scanning and transmission electron microscopy. *Appl. Phys. A Mater. Sci. Process.*, **77**, 411–417.

Borowiec, A., Couillard, M., Botton, G.A., Haugen, H.K. (2004): Sub-surface damage in indium phosphide caused by micromachining of grooves with femtosecond and nanosecond laser pulses. *Appl. Phys. A Mater. Sci. Process.*, **79**, 1887–1890.

Choi, T.Y. & Grigoropoulos, C.P. (2002): Plasma and ablation dynamics in ultrafast laser processing of crystalline silicon. *J. Appl. Phys.*, **92**, 4918–4925.

Couillard, M., Borowiec, A., Haugen, H.K., Preston, J.S., Griswold, E.M., Botton, G.A. (2007): Subsurface modifications in indium phosphide induced by single and multiple femtosecond laser pulses: a study on the formation of periodic ripples. *J. Appl. Phys.*, **101**, doi:10.1063/1.2407259.

Coyne, E., Magee, J.P., Mannion, P., O'Connor, G.M., Glynn, T.J. (2005): STEM (scanning transmission electron microscopy) analysis of femtosecond laser pulse induced damage to bulk silicon. *Appl. Phys. A Mater. Sci. Process.*, **81**, 371–378.

d'Abzac, F.X., Seydoux-Guillaume, A.M., Poitrasson, F., Freydier, R., Wirth, R., Datas, L. (in press): Near infra red femtosecond laser ablation: the influence of energy and pulse width on ICP-MS signal of natural monazite. *J. Anal. At. Spectrom.*

Dougherty, L.M., Cerreta, E.K., Pfeif, E.A., Trujillo, C.P., Gray, G.T. (2007): The impact of peak shock stress on the microstructure and shear behavior of 1018 steel. *Acta Mater.*, **55**, 6356–6364.

Fernandez, B., Claverie, F., Pecheyran, C., Donard, O.F.X. (2007): Direct analysis of solid samples by fs-LA-ICP-MS. *Trends Anal. Chem.*, **26**, 951–966.

Freydier, R., Candaudap, F., Poitrasson, F., Arbouet, A., Chatel, B., Dupré, B. (2008): Evaluation of infrared femtosecond laser ablation for the analysis of geomaterials by ICP-MS. *J. Anal. At. Spectrom.*, **23**, 702–710.

Gorelik, T., Will, M., Nolte, S., Tuennermann, A., Glatzel, U. (2003): Transmission electron microscopy studies of femtosecond laser induced modifications in quartz. *Appl. Phys. A Mater. Sci. Process.*, **76**, 309–311.

Guillermin, M., Garrelie, F., Sanner, N., Audouard, E., Soder, H. (2007): Single- and multi-pulse formation of surface structures under static femtosecond irradiation. *Appl. Surf. Sci.*, **253**, 8075–8079.

Guillong, M. & Günther, D. (2002): Effect of particle size distribution on ICP-induced elemental fractionation in laser ablation-inductively coupled plasma-mass spectrometry. *J. Anal. At. Spectrom.*, **17**, 831–837.

Hay, R.S. & Marshall, D.B. (2003): Deformation twinning in monazite. *Acta Mater.*, **51**, 5235–5254.

Horn, I. & von Blanckenburg, F. (2007): Investigation on elemental and isotopic fractionation during 196 nm femtosecond laser ablation multiple collector inductively coupled plasma mass spectrometry. *Spectrochim. Acta Part B*, **62**, 410–422.

Ikehata, K., Notsu, K., Hirata, T. (2008): In situ determination of Cu isotope ratios in copper-rich materials by NIR femtosecond LA-MC-ICP-MS. *J. Anal. At. Spectrom.*, **23**, 1003–1008.

Jackson, S.E. & Günther, D. (2003): The nature and sources of laser induced isotopic fractionation in laser ablation-multicollector-inductively coupled plasma-mass spectrometry. *J. Anal. At. Spectrom.*, **18**, 205–212.

Jia, J., Li, M., Thompson, C.V. (2004): Amorphization of silicon by femtosecond laser pulses. *Appl. Phys. Lett.*, **84**, 3205–3207.

Kösler, J., Wiedenbeck, M., Wirth, R., Hovorka, J., Sylvester, P., Mikova, J. (2005): Chemical and phase composition of particles produced by laser ablation of silicate glass and zircon – implications for elemental fractionation during ICP-MS analysis. *J. Anal. At. Spectrom.*, **20**, 402–409.

Kuhn, H.-R., Guillong, M., Günther, D. (2004): Size-related vaporisation and ionisation of laser-induced glass particles in the inductively coupled plasma. *Analytical and Bioanalytical Chemistry*, **378**, 1069–1074.

Ladieu, F., Martin, P., Guizard, S. (2002): Measuring thermal effects in femtosecond laser-induced breakdown of dielectrics. *Appl. Phys. Lett.*, **81**, 957–959.

Langenhorst, F., Boustie, M., Migault, A., Romain, J.P. (1999): Laser shock experiments with nanoseconds pulses: a new tool for the reproduction of shock defects in olivine. *Earth Planet. Sci. Lett.*, **173**, 333–342.

Laville, S., Vidal, F., Johnston, T.W., Barthelemy, O., Chaker, M., Drogoff, B.L., Margot, J., Sabsabi, M. (2002): Fluid modeling of the laser ablation depth as a function of the pulse duration for conductors. *Phys. Rev. E*, **66**, 664151–664157.

Le Harzic, R., Huot, N., Audouard, E., Jonin, C., Laporte, P., Valette, S., Fraczkiewicz, A., Fortunier, R. (2002): Comparison of heat-affected zones due to nanosecond and femtosecond laser pulses using transmission electronic microscopy. *Appl. Phys. Lett.*, **80**, 3886–3888.

Leroux, H., Stroud, R.M., Dai, Z.R., Graham, G.A., Troadec, D., Bradley, J.P., Teslich, N., Borg, J., Kearsley, A.T., Hoerz, F. (2008): Transmission electron microscopy of cometary residues from micron-sized craters in the Stardust Al foils. *Meteorit. Planet. Sci.*, **43**, 143–160.

Liu, Y.F. & Niemz, M. (2007): Ablation of femural bone with femtosecond laser pulses – a feasibility study. *Lasers Med. Sci.*, **22**, 171–174.

Lorazo, P., Lewis, L.J., Meunier, M. (2003): Short-pulse laser ablation of solids: from phase explosion to fragmentation. *Phys. Rev. Lett.*, **91**, 225502-1–225502-4.

Ma, H.L., Guo, G.L., Yang, J.Y., Guo, Y., Ma, N.H. (2007): Femtosecond laser irradiation-induced phase transformation on titanium dioxide crystal surface. *Nucl. Instrum. Methods Phys. Res. B*, **264**, 61–65.

Meldrum, A., Boatner, L.A., Ewing, R.C. (1997): Displacive radiation effects in the monazite- and zircon-structure orthophosphates. *Phys. Rev. B*, **56**, 13805–13814.

Meldrum, A., Boatner, L.A., Weber, W.J., Ewing, R.C. (1998): Radiation damage in zircon and monazite. *Geochim. Cosmochim. Acta*, **62**, 2509–2520.

Nasdala, L., Lengauer, C.L., Hanchar, J.M., Kronz, A., Wirth, R., Blanc, P., Kennedy, A.K., Seydoux-Guillaume, A.M. (2002): Annealing radiation damage and the recovery of cathodoluminescence. *Chem. Geol.*, **191**, 121–140.

Neev, J., Da Silva, L.B., Feit, M.D., Perry, M.D., Rubenchik, A.M., Stuart, B.C. (1996): Ultrashort pulse laser system for hard dental tissue procedures. Lasers in dentistry II: San Jose CA, 28–29 January 1996. *Proc. SPIE-Int. Soc. Opt. Eng.*, 210–221.

Niemz, M.H. (1998): Ultrashort laser pulses in dentistry: advantages and limitations. Applications of ultrashort-pulse lasers in medicine and biology: San Jose CA, 29–30 January 1998. *Proc. SPIE-Int. Soc. Opt. Eng.*, 84–91.

Niemz, M.H., Kasenbacher, A., Strassl, M., Backer, A., Beyertt, A., Nickel, D., Giesen, A. (2004): Tooth ablation using a CPA-free thin disk femtosecond laser system. *Appl. Phys. B Lasers Opt. Print.*, **79**, 269–271.

Paquette, J.L. & Tiepolo, M. (2007): High resolution (5 µm) U-Th-Pb isotope dating of monazite with excimer laser ablation (ELA)-ICPMS. *Chem. Geol.*, **240**, 222–237.

Perry, M.D., Stuart, B.C., Banks, P.S., Feit, M.D., Yanovsky, V., Rubenchik, A.M. (1999): Ultrashort-pulse laser machining of dielectric materials. *J. Appl. Phys.*, **85**, 6803–6810.

Poitrasson, F., Chenery, S., Shepherd, T.J. (2000): Electron microprobe and LA-ICP-MS study of monazite hydrothermal alteration: Implications for U-Th-Pb geochronology and nuclear ceramics. *Geochim. Cosmochim. Acta*, **64**, 3283–3297.

Poitrasson, F., Mao, X.L., Mao, S.S., Freydier, R., Russo, R.E. (2003): Comparison of ultraviolet femtosecond and nanosecond laser ablation inductively coupled plasma mass spectrometry analysis in glass, monazite, and zircon. *Anal. Chem.*, **75**, 6184–6190.

Sano, T., Mori, H., Sakata, O., Ohmura, E., Miyamoto, I., Hirose, A., Kobayashi, K.F. (2005): Femtosecond laser driven shock synthesis of the high-pressure phase of iron. *Appl. Surf. Sci.*, **247**, 571–576.

Seydoux-Guillaume, A.M., Paquette, J.L., Wiedenbeck, M., Montel, J.M., Heinrich, W. (2002a): Experimental resetting of the U-Th-Pb systems in monazite. *Chem. Geol.*, **191**, 165–181.

Seydoux-Guillaume, A.M., Wirth, R., Nasdala, L., Gottschalk, M., Montel, J.M., Heinrich, W. (2002b): An XRD, TEM and Raman study of experimentally annealed natural monazite. *Phys. Chem. Minerals*, **29**, 240–253.

Seydoux-Guillaume, A.M., Goncalves, P., Wirth, R., Deutsch, A. (2003): Transmission electron microscope study of polyphase and discordant monazites: site-specific specimen preparation using the focused ion beam technique. *Geology*, **31**, 973–976.

Seydoux-Guillaume, A.M., Wirth, R., Deutsch, A., Schärer, U. (2004): Microstructure of 24-1928 Ma concordant monazites; implications for geochronology and nuclear waste deposits. *Geochim. Cosmochim. Acta*, **68**, 2517–2527.

Seydoux-Guillaume, A.M., Wirth, R., Ingrin, J. (2007): Contrasting response of $ThSiO_4$ and monazite to natural irradiation. *Eur. J. Mineral.*, **19**, 7–14.

Sokolowski-Tinten, K., Bialkowski, J., Cavalleri, A., von der Linde, D., Oparin, A., Meyer-ter-Vehn, J., Anisimov, S.I. (1998): Transient states of matter during short pulse laser ablation. *Phys. Rev. Lett.*, **81**, 224–227.

Stach, E.A., Radmilovic, V., Deshpande, D., Malshe, A., Alexander, D., Doerr, D. (2003): Nanoscale surface and subsurface defects induced in lithium niobate by a femtosecond laser. *Appl. Phys. Lett.*, **83**, 4420–4422.

Varlamova, O., Costache, F., Ratzke, M., Reif, J. (2007): Control parameters in pattern formation upon femtosecond laser ablation. *Appl. Surf. Sci.*, **253**, 7932–7936.

Vidal, F., Laville, S., Johnston, T.W., Barthélemy, O., Chaker, M., Le Drogoff, B., Margot, J., Sabsabi, M. (2001): Numerical simulations of ultrashort laser pulse ablation and plasma expansion in ambient air. *Spectrochim. Acta Part B*, **56**, 973–986.

von der Linde, D. & Sokolowski-Tinten, K. (2000): The physical mechanisms of short-pulse laser ablation. *Appl. Surf. Sci.*, **154**, 1–10.

von der Linde, D., Sokolowski Tinten, K., Bialkowski, J. (1997): Laser-solid interaction in the femtosecond time regime. Laser processing of surfaces and thin films. *Appl. Surf. Sci.*, 1–10.

Wirth, R. (2004): Focused Ion Beam (FIB): a novel technology for advanced application of micro- and nanoanalysis in geosciences and applied mineralogy. *Eur. J. Mineral.*, **16**, 863–876.

Yong, J.E.E., Becker, M.F., Walser, R.M. (1988): Laser-induced damage on single-crystal metal surfaces; Dommage induit par laser sur les surfaces monocristalines metalliques. *J. Opt. Soc. Am. B Opt. Phys.*, **5**, 648–659.

Received 24 July 2009
Modified version received 13 October 2009
Accepted 4 November 2009